Biochar

Check for updates

# Harnessing the power of functionalized biochar: progress, challenges, and future perspectives in energy, water treatment, and environmental sustainability

Muhammad Zubair Yameen[1,2], Salman Raza Naqvi[1,3]* , Dagmar Juchelková[2] and Muhammad Nouman Aslam Khan[1]

## Abstract

The swift advancement of sustainable energy technologies, coupled with the urgent need to address environmental challenges, has generated considerable interest in the multifaceted applications of biochar materials to promote energy, water, and environmental sustainability. This comprehensive review examines recent advancements in the production and applications of functionalized biochar materials, emphasizing their pivotal roles in energy conversion and storage, wastewater treatment, $CO_2$ reduction, soil amelioration, and the promotion of carbon neutrality within a circular economy framework. The functionalization of biochar materials involves surface chemistry and porosity modifications, achieved through techniques like templating, chemical activation, metal impregnation, or heteroatom doping. These modifications substantially enhance the catalytic activity, energy storage capacity, and cycling stability of biochar materials, making them particularly effective in diverse energy applications such as water splitting, fuel cells, and supercapacitors. Additionally, functionalized biochar materials demonstrate remarkable efficacy as catalysts and adsorbents in wastewater treatment, proficiently removing pollutants like heavy metals, organic contaminants, and nutrients, thereby facilitating resource recovery from wastewater. The review also underscores the potential of functionalized biochar materials in $CO_2$ capture and conversion, exploring innovative strategies to augment their $CO_2$ adsorption capacity and state-of-the-art catalytic processes for transforming captured $CO_2$ into valuable fuels and chemicals. In summary, this review offers valuable insights into the recent advancements in biochar research, underscoring its substantial commercial potential as a versatile material contributing to a cleaner and more sustainable future.

## Article Highlights

- The current status of biochar research is comprehensively reviewed.
- The potential of biochar in energy, water, and environmental fields is critically examined.
- Technology readiness levels (TRLs) of various biochar-based technologies are evaluated.

---

*Correspondence:
Salman Raza Naqvi
salman.raza.naqvi@kau.se
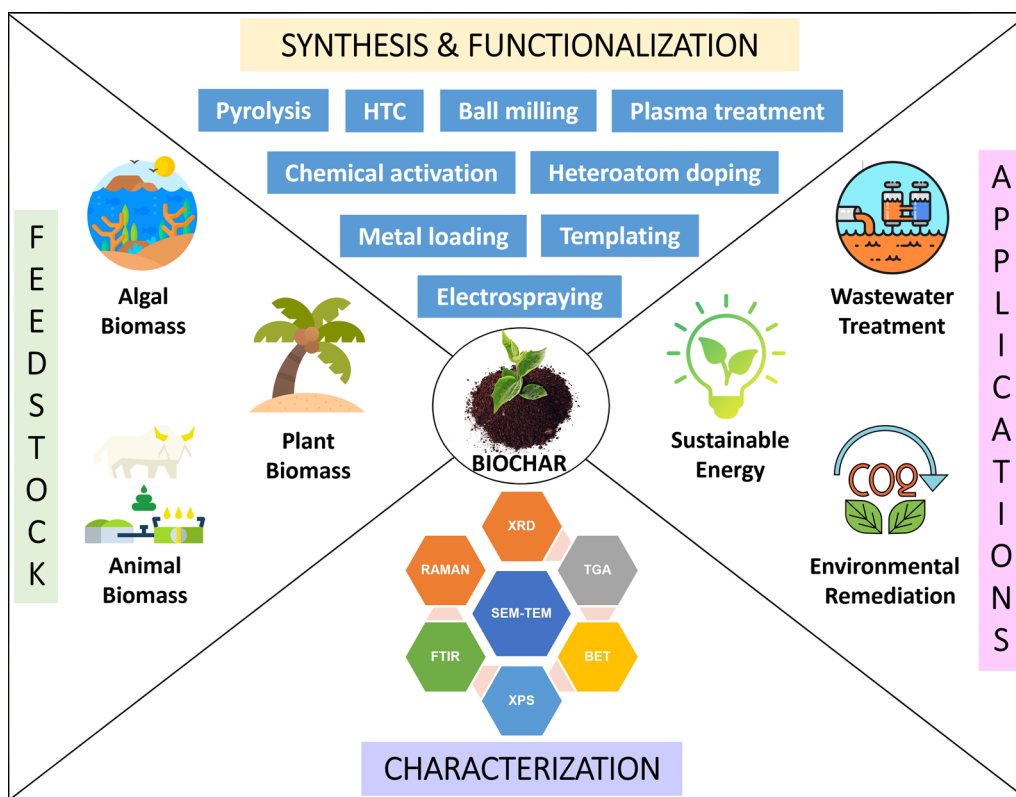Full list of author information is available at the end of the article

Springer

**Graphical Abstract**



## 1 Introduction

The twenty-first century poses two major global challenges for sustainable development: the increasing energy deficits and the worsening environmental pollution (Yuan et al. 2023b). The rapid growth of global energy consumption, along with the depletion of fossil fuel reserves, threatens the energy security of the world. Simultaneously, environmental pollution is impacting the quality of air, water, and soil, endangering both biodiversity and human health. Consequently, there is an urgent need to develop sustainable and eco-friendly technologies that can address these critical issues. One of the promising innovations in this regard is the utilization of sustainable biochar materials derived from biomass waste resources, which find versatile applications in energy generation, water purification, and environmental remediation (Tiwari et al. 2022).

Biochar is a carbon-rich material obtained through the thermochemical conversion of biomass, involving processes like pyrolysis and hydrothermal carbonization. Traditionally, it has been used as a soil amendment to enhance soil fertility and sequester carbon (He et al. 2023). However, recent advancements in biochar functionalization have opened up new avenues for its use in various fields, including energy conversion and storage, wastewater treatment, and environmental remediation (Feng et al. 2023; Yang et al. 2023b). Functionalized biochar materials exhibit abundant active sites, such as Bronsted acid sites, Lewis acid sites, base sites, metal sites, and redox sites, as well as favorable physicochemical features, such as a porous structure, high surface area, chemical functional groups, and thermal stability (Yameen et al. 2023b). These attributes make biochar an ideal candidate for catalytic and remediation

applications. Biorefineries represent a sustainable approach aimed at harnessing $CO_2$ through photosynthesis and converting renewable biomass resources into a diverse range of bio-products, including biofuels, biochemicals, and biomaterials, through various thermochemical and biochemical processes (Naqvi et al. 2018a). They seek to replace the traditional fossil-based refineries that rely on non-renewable fossil fuels like coal, crude oil,

and natural gas, which result in significant greenhouse gas (GHG) emissions, primarily in the form of $CO_2$, leading to various environmental problems (AlMohamadi et al. 2023). Biorefineries play a vital role in promoting a more sustainable society, emphasizing the principles of an eco-friendly circular economy (Khan et al. 2023e). Figure 1a and b provide a visual comparison between traditional fossil-based refineries and biorefineries.
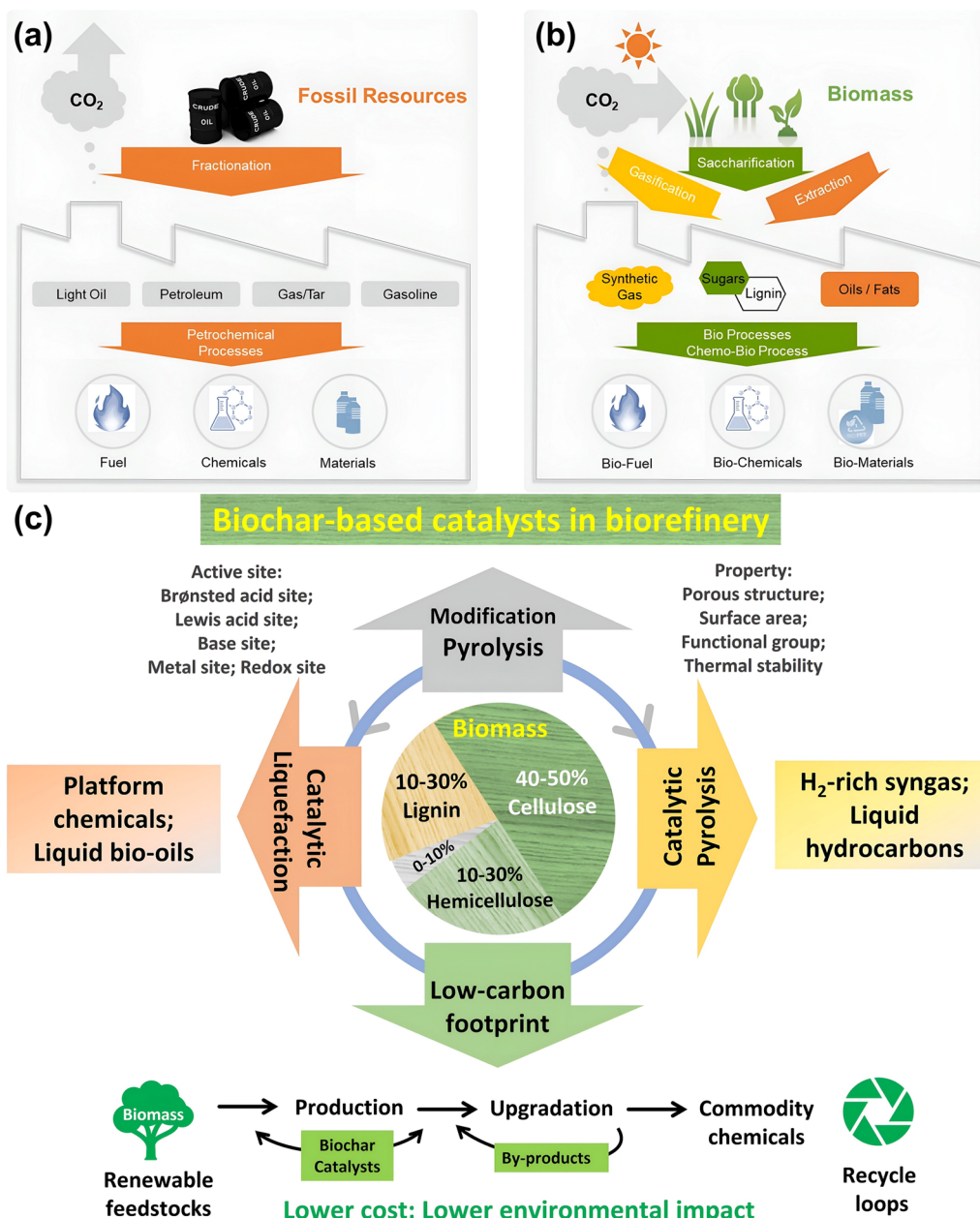


**Fig. 1** Fundamental concepts of (**a**) fossil-based refinery and (**b**) biorefinery processes (Park et al. 2023b), Copyright © 2023, The Author(s), Elsevier. **c** General overview of biochar-based catalytic processes within a biorefinery (Yuan et al. 2023a), Copyright© 2023, The Author(s), Elsevier

Biochar-based catalysts play a pivotal role in enhancing the efficiency and selectivity of biomass conversion processes within biorefineries, including catalytic pyrolysis, catalytic liquefaction, and catalytic gasification (Yuan et al. 2023a). These catalytic processes transform biomass into biofuels, $H_2$-rich syngas, and valuable chemicals, all contributing to the pursuit of carbon neutrality (Yameen et al. 2023a), as depicted in Fig. 1c. In recent years, functionalized biochar materials have gained significant attention for their diverse applications across water splitting (Xia et al. 2022a), fuel cells (Lu et al. 2021), supercapacitors (Yan et al. 2022), wastewater treatment (Khan et al. 2023c), $CO_2$ capture (Zhang et al. 2022), and electrochemical $CO_2$ reduction (Tan et al. 2023). Encouraging the sustainable application of biochar-based catalytic and remediation technologies is essential, not only for economic and social benefits but also for addressing and mitigating the environmental challenges associated with fossil fuels and hazardous wastes.

To assess recent academic contributions in the field of biochar research, a bibliometric analysis was conducted in the "Scopus core collection" using the Boolean search string "TITLE-ABS-KEY ("biochar" AND "energy" AND "water" AND "environment")" for the past decade (2014–2023). The parsing and analysis of the Scopus database were executed using the bibliometrix package in R (Aria and Cuccurullo 2017). Microsoft Excel was employed for the analysis of publication and citation overviews, while VOSviewer software version 1.6.19 was used for keyword co-occurrence analysis. As of October 23, 2023, the search yielded a total of 302 documents from 133 sources. The corpus comprised eight document types, with research articles being the most prevalent (223; 73.8%), followed by review articles (47; 15.6%), conference papers (11; 3.6%), book chapters (11; 3.6%), conference reviews (7; 2.3%), books (1; 0.3%), errata (1; 0.3%), and notes (1; 0.3%). The majority of documents, 285 (94.37%), were in English, while 17 documents (5.62%) were in Chinese. Over the period 2014–2023, China emerged as the leading contributor to biochar research, with a total of 160 publications and 4313 citations. Figure 2a illustrates the growth in publication and citation counts over the years, increasing from 5 publications and 2 citations in 2014 to 86 publications and 2869 citations in 2023. The Scopus database was then imported into VOSviewer 1.6.17 software to generate a co-occurrence map of all keywords used in the publications. Full counting was chosen as the counting method, with a minimum keyword occurrence set to 5. A total of 422 keywords met this specified criterion, with "biochar" being the most prominent keyword (237 occurrences), followed by "charcoal" (138

occurrences), "adsorption" (124 occurrences), "pyrolysis" (92 occurrences), and "biomass" (65 occurrences), as shown in Fig. 2b. The network visualization unveils links between keywords organized into five distinct clusters. The red cluster comprises 167 keywords, primarily associated with the characteristics and applications of biochar. The green cluster (101 keywords) is focused on charcoal utilization, while the blue cluster (76 keywords) contains terms primarily associated with wastewater treatment. The yellow cluster (63 keywords) concentrates on the adsorption process, and the purple cluster (15 keywords) is centered around chemical analysis.

In response to the growing interest in biochar-based engineered materials (such as catalysts, adsorbents, and electrodes) and the lack of comprehensive studies in this field as evident in bibliometric analysis, this review aims to provide an up-to-date overview of biochar research and highlight recent progress in the fabrication, characterization, and applications of functionalized biochar materials, with a specific emphasis on their significance in the domains of energy conversion and storage, wastewater treatment, carbon capture and conversion, and soil amelioration. Firstly, this review delves into the recent advances in widely used thermochemical conversion processes, notably pyrolysis and hydrothermal carbonization (HTC), for the advanced production of biochar materials from a variety of biomass sources, with an emphasis on improving their quality. More importantly, particular emphasis is placed on critically examining various functionalization strategies, including (i) ball milling, (ii) templating, (iii) molten salt activation, (iv) chemical activation, (v) metal impregnation, (vi) heteroatom doping, (vii) plasma treatment, and (viii) electrospraying, all aimed at enhancing the physicochemical properties (like surface area, porosity, chemical functional groups, and thermal stability) and electrochemical characteristics (such as electrical conductivity, redox activity, and electrochemical stability) of pristine biochar materials. Subsequently, the review explores the development of advanced characterization techniques for engineered biochar materials, including SEM-TEM, XRD, BET, TGA, XPS, FTIR, and Raman spectroscopy. Lastly, the application advances of engineered biochar materials are systematically summarized and discussed in the following areas: (i) water splitting; (ii) fuel cells; (iii) supercapacitors; (iv) wastewater treatment and resource recovery; (v) $CO_2$ capture and reduction; (vi) soil amelioration. Additionally, the review evaluates the technology readiness levels (TRLs) of biochar-based technologies and highlights research gaps and perspectives for further research and potential commercialization.
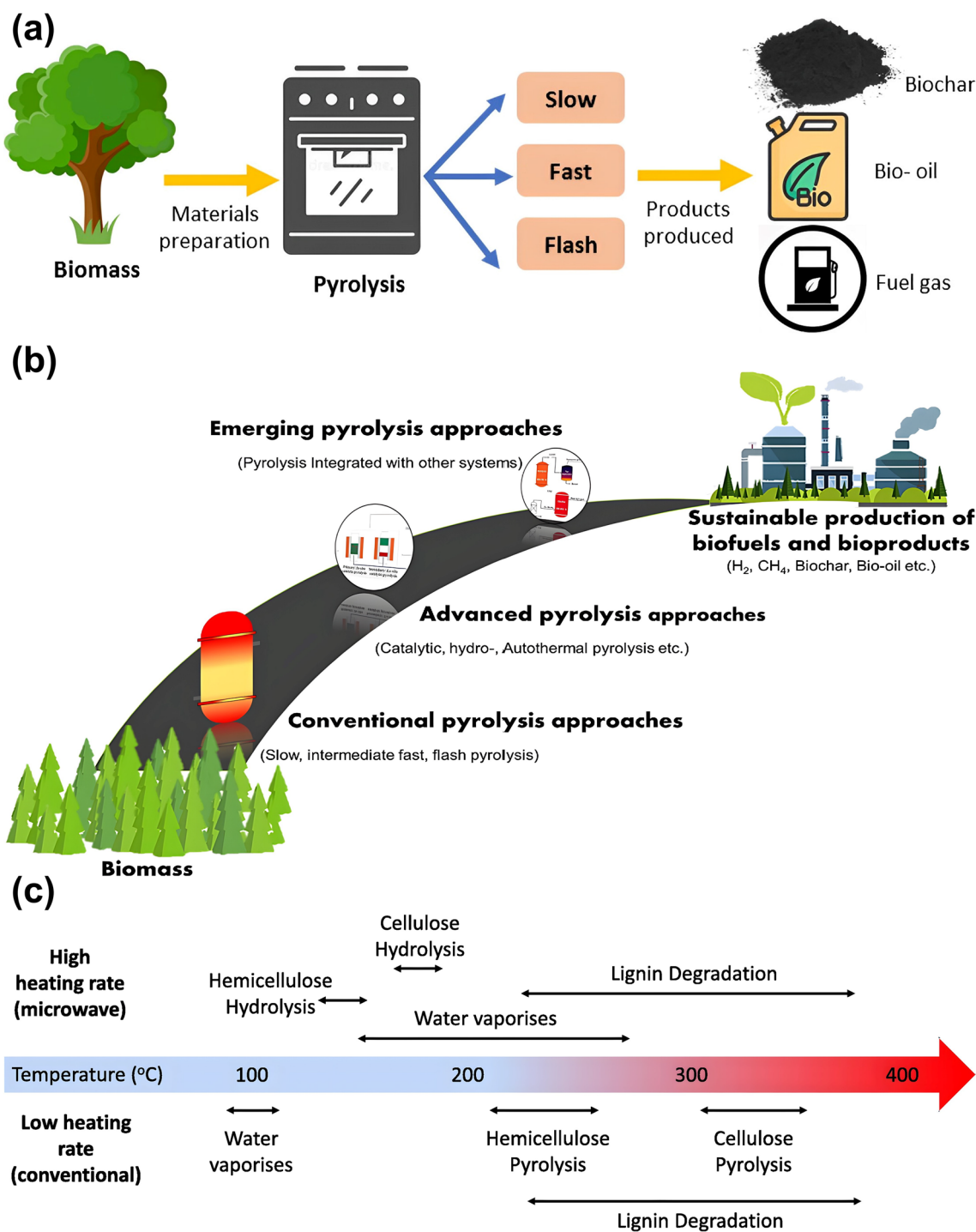
**Fig. 2** **a** Trends in publication and citation counts. **b** Co-occurrence of all keywords

## 2 Biochar production techniques

### 2.1 Pyrolysis

Pyrolysis refers to the thermal degradation of biomass sources, such as plant residues or organic wastes, into carbon-rich bio-products, including biochar, bio-oil, and syngas, at temperatures typically ranging from 400 to 800 °C within an inert gas environment (e.g., $N_2$, Ar). Pyrolysis usually occurs in a tubular furnace, and the characteristics and distribution of pyrolytic products derived from a particular biomass source are predominantly determined by the operational parameters, which encompass temperature, heating rate, and residence time (Khan et al. 2022c). The general concept of the pyrolysis

process for the conversion of biomass into biochar, bio-oil, and fuel gases is illustrated in Fig. 3a. The pyrolysis process involves a multitude of chemical reactions, including dehydration, devolatilization, depolymerization, isomerization, aromatization, and charring (Khan et al. 2023a). However, at its core, pyrolysis can be simplified into three main mechanisms: devolatilization, isomerization, and char formation. Initially, the biomass is subjected to a drying process within the temperature range of 100–200 °C to eliminate water vapors. Then it undergoes devolatilization within the temperature range of 200–400 °C. During this phase, biomass precursors start to decompose, releasing volatiles such as $CO_2$, $CH_4$,

**(a)**



**(b)**



**(c)**



**Fig. 3 a** Schematic depiction of the pyrolysis process (Amalina et al. 2022), Copyright © 2022, The Authors, Elsevier. **b** Various approaches employed in biomass pyrolysis (Vuppaladadiyam et al. 2022), Copyright© 2022, Elsevier. (**c**) Heating scheme for conventional and microwave-assisted pyrolysis (Robinson et al. 2022), Copyright© 2022, Elsevier

and numerous organic gases as by-products. In the temperature range of 250–500 °C, the bonds between the monomer units break, leading to depolymerization. This process continues, causing the monomers to become volatile. Finally, at temperatures ranging from 450 to 550 °C, a fragmentation process occurs, where covalent bonds

between the monomer units become interconnected, resulting in the formation of solid material called biochar, primarily composed of carbon, with some ash content (Naveed et al. 2024).

Vuppaladadiyam et al. (2022) analyzed recent progress in biomass pyrolysis, categorizing it into conventional, advanced, and emerging approaches to promote the sustainable development of bioproducts (e.g., biochar, bio-oil, $CH_4$, $H_2$, etc.), as illustrated in Fig. 3b. Conventional pyrolysis approaches can be divided into four primary categories primarily based on operational parameters: (i) slow pyrolysis, (ii) intermediate pyrolysis, (iii) fast pyrolysis, and (iv) flash pyrolysis. The heating rate can be viewed as a pivotal parameter that not only defines the pyrolysis category but also influences the product distribution. Typically, slow pyrolysis aims to maximize the production of biochar, whereas intermediate, fast, and flash pyrolysis prioritize the production of bio-oil. Advanced pyrolysis techniques have the potential to overcome the limitations associated with conventional pyrolysis processes. Their primary goal is to enhance both the yield and quality of pyrolysis products while also enabling more precise control over the desired pyrolytic product. These techniques encompass various approaches, including catalytic pyrolysis, hydropyrolysis, co-pyrolysis, and microwave-assisted pyrolysis, each offering unique advantages and opportunities for optimizing the pyrolysis process (Gohar et al. 2022). Microwave-assisted pyrolysis is an innovative approach to biomass conversion that can offer rapid heating, improved efficiency, and better control over the pyrolysis process, making it particularly well-suited for biochar production (Potnuri et al. 2023). Microwave-induced rapid heating demonstrates its ability to significantly reduce the necessary pyrolysis temperatures for breaking down cellulose and hemicellulose constituents. The heating rate emerges as the pivotal factor driving the specific outcomes in microwave-assisted pyrolysis. Microwave heating, being independent of heat transfer limitations, typically results in rapid heating rates. However, when using low microwave power or domestic microwave ovens, the heating rate becomes slow and is comparable to conventional heating approaches (Robinson et al. 2022). In instances of rapid heating rates, such as with microwave heating, water evaporates rapidly. This leads to elevated pressure within the biomass, raising its boiling point and causing liquid water to persist within the biomass even at temperatures well above 100 °C. This water triggers the hydrolysis of hemicellulose at approximately 130 °C, with furfural being the primary product. Cellulose hydrolysis occurs at around 175 °C, yielding levoglucosan as the primary product. Further heating leads to the decomposition of lignin until it transforms into a carbon-rich biochar product. For instance, in their study, Robinson et al. (2022) indicated that microwave-assisted pyrolysis can effectively break down hemicellulose at 145 °C, whereas conventional heating necessitates temperatures as high as 210 °C for the same process. Similarly, cellulose decomposition can occur at 180 °C when using microwave heating, in contrast to the 300 °C required in conventional approaches. Lignin decomposition, on the other hand, follows similar reaction pathways to those observed in conventional pyrolysis, primarily because it has limited hydrolyzable linkages (Dos Santos et al. 2019). The heating scheme for both conventional and microwave-assisted pyrolysis is depicted in Fig. 3c. The emerging pyrolysis approaches primarily focus on the circular economy and involve the integration of pyrolysis with other thermochemical processes, such as gasification, or biochemical processes like anaerobic digestion (AD). These innovative approaches aim to enhance resource recovery by mitigating the shortcomings inherent in each process (Vuppaladadiyam et al. 2022).

The intrinsic characteristics of biochar, including its elemental composition, proximate composition, pH levels, surface area, and pore volume, can be impacted by both the choice of biomass feedstock and the precise parameters employed during pyrolysis. For example, Song et al. (2021) produced biochar from Kentucky bluegrass waste biomass through a pyrolysis process at three distinct temperatures (350, 550, and 750 °C) with a residence time of 2 h. The reported biochar yields were 40.0%, 12.0%, and 8.0% at pyrolysis temperatures of 350, 550, and 750 °C, respectively. The ultimate analysis of the biochar's elemental composition revealed that as the pyrolysis temperature increased from 350 to 750 °C, the C element content increased from 64.0% to 69.0%, while the O content decreased from 17.5% to 6.4% and the N content decreased from 2.7% to 2.2%. Additionally, the proximate analysis indicated an increase in ash content from 11.6% to 21.6% as the pyrolysis temperature increased from 350 to 750 °C. The pH of the resulting biochars was measured at 6.4 for BC-350, 7.0 for BC-550, and 7.1 for BC-750. Moreover, the specific surface area (SSA) and total pore volume (TPV) of the biochar increased with the rising pyrolysis temperature up to 550 °C, where they reached their maximum values of 190 $m^2$ $g^{-1}$ and 0.14 $cm^3$ $g^{-1}$, respectively. However, further elevating the pyrolysis temperature to 750 °C resulted in a reduction in both SSA (118 $m^2$ $g^{-1}$) and TPV (0.04 $cm^3$ $g^{-1}$) of biochar. Figure 4a illustrates the impact of pyrolysis temperature on biochar production yield. As the pyrolysis temperature rises, the biochar yield diminishes, with a smaller reduction observed at higher temperature ranges. The most significant decrease in biochar
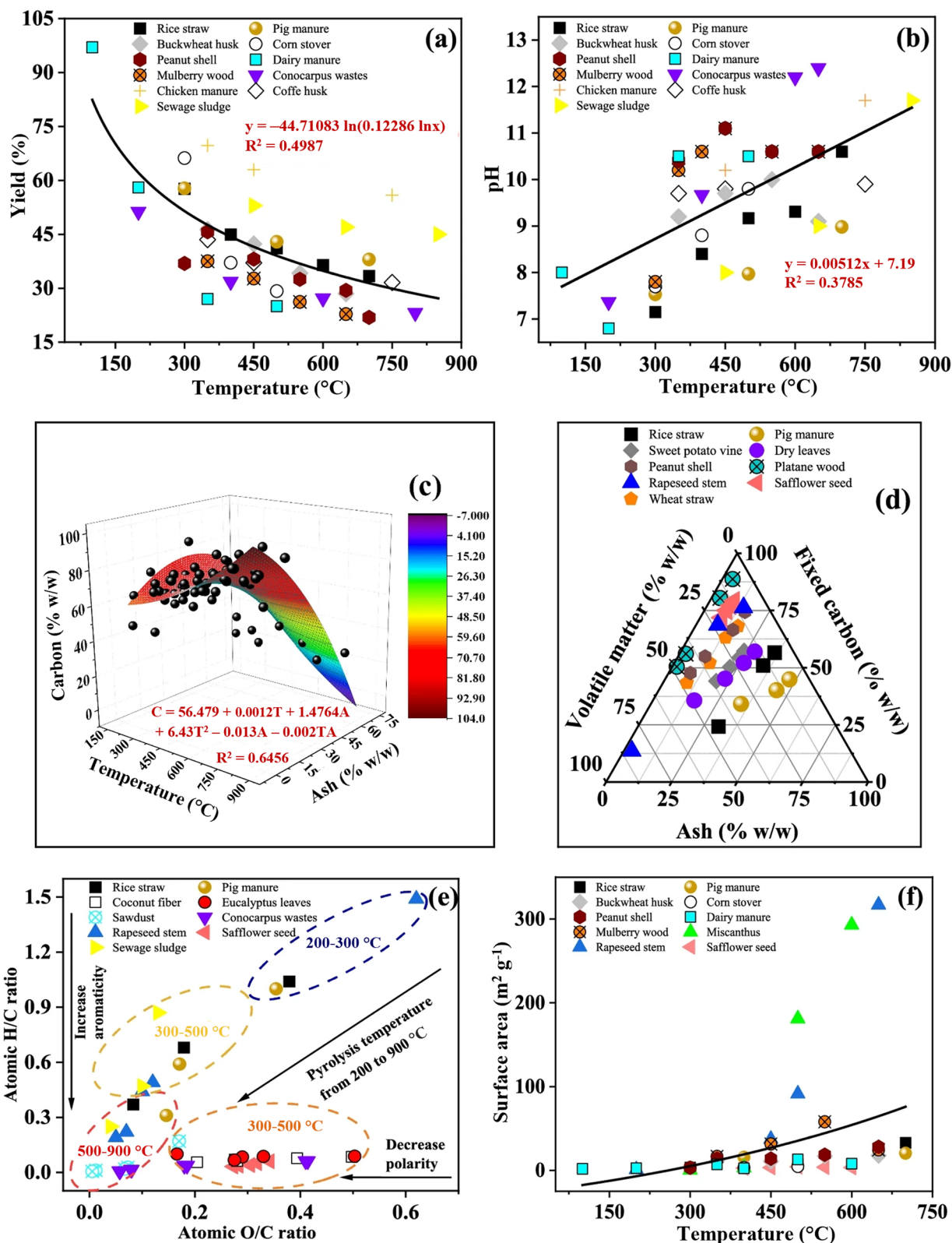
**Fig. 4** **a** Percentage yields and (**b**) pH trends of biochars; **c** Variations in carbon content of biochar with pyrolysis temperature and ash content; **d** Ternary diagram illustrating ash content, volatile matter, and fixed carbon; **e** Van Krevelen diagram depicting pyrolytic biochar characteristics; **f** Surface areas of biochars with increasing temperatures (Yang et al. 2022a), Copyright [©] 2022, The Authors, Springer Nature

yield occurs within the temperature range of 200–400 °C. For instance, when processing corn stalks, the biochar yield experiences a 27.7% decline when the temperature rises from 300 to 400 °C, whereas the decline is only 8.9% when the temperature rises from 500 to 600 °C (Sun et al. 2017). According to Fig. 4b, as the pyrolysis temperature rises, the pH level increases. This pH increase is attributed to the removal of organic acids from the biomass precursor during decomposition reactions, resulting in higher alkalinity (Yang et al. 2022a). Figure 4c depicts the variation in the fixed carbon (FC) content of biochar as influenced by both pyrolysis temperature and ash content. The ternary diagram in Fig. 4d reveals that as pyrolysis temperature rises, the biochar composition shifts from predominantly comprising volatile matter (VM) to predominantly comprising FC. For instance, in their research, Zhao et al. (2018) observed a significant alteration in the composition of rapeseed stem biochar as the temperature was raised from 200 to 700 °C. Within this temperature range, the VM content decreased from 81.8% to 9.3%, while the ash content rose from 3.0% to 14.1%, and the FC content enriched from 13.3% to 75.2%. In Fig. 4e, it is evident that as the temperature rises during pyrolysis, the rate of decrease in O/C ratios surpasses that of H/C ratios, indicating a shift towards enhanced aromaticity. Figure 4f illustrates that as the pyrolysis temperature rises, the surface area of the biochar also expands. This occurs because elevated temperatures trigger the thermal cracking of pore-blocking substances, thereby enhancing the externally accessible surface area. The elevated temperatures prompt the release of volatiles and the creation of more micro/meso pores in the biochar structure. Additionally, the breakdown of aliphatic alkyls and ester groups, along with the exposure of the aromatic core at elevated temperatures, can contribute to the expansion of the surface area (Tomczyk et al. 2020). However, it is worth noting that estimating the surface area solely based on temperature is not feasible, and further increases in temperature may not necessarily lead to continued surface area growth; in fact, it may even cause a decrease. Table 1 provides a comprehensive overview of both the pyrolysis parameters and the inherent characteristics of biochar produced from a diverse range of biomass feedstocks.

### 2.1.1 Limitations of pyrolysis

Pyrolysis is a commonly utilized thermochemical conversion technology for transforming organic wastes into biochar, but it comes with certain limitations:

(1) The properties of biochar can vary significantly depending on biomass feedstock, pyrolysis conditions, and post-treatment, making it difficult to achieve consistent quality for specific applications. Establishing industry-wide standards for biomass selection, preparation, and pyrolysis parameters is essential to ensure product uniformity.

(2) The pyrolysis process necessitates high heating temperatures (400–800 °C), consuming significant energy, especially for large-scale operations. Integrating renewable energy sources such as solar or bioenergy to power pyrolysis plants, optimizing process parameters, and harnessing waste heat can significantly reduce overall energy consumption.

(3) Pyrolysis can lead to the loss of certain nutrients present in the biomass, affecting the nutrient content of the biochar. Implementing techniques like slow pyrolysis and adjusting process parameters can help minimize nutrient loss.

(4) There is a lack of standardized methods for characterizing and testing biochar. Developing and implementing standardized protocols for biochar characterization is imperative to guarantee product quality and streamline broader market acceptance.

## 2.2 Hydrothermal carbonization

Hydrothermal carbonization (HTC) facilitates the creation of biochar materials, often referred to as hydrochar, at relatively low temperatures typically ranging from 180 to 250 °C and under moderate pressures (subcritical conditions) of up to 6.0 MPa, with water serving as the reaction medium. This process eliminates the necessity for pre-drying biomass, operates under mild conditions, and is notable for its relatively modest energy consumption. During the HTC processing of biomass, a variety of complex chemical reactions, including hydrolysis, decarboxylation, dehydration, condensation, polymerization, and aromatization, occur concurrently (Khan et al. 2023d). The conversion process begins by breaking down biomass components such as cellulose, hemicellulose, and lignin through hydrolysis reactions. Typically, hemicellulose undergoes hydrolysis at around 180 °C, lignin undergoes hydrolysis at ~ 200 °C, and cellulose's hydrolysis occurs at temperatures exceeding 200 °C, resulting in the formation of smaller molecules like sugars, organic acids, and others (Świątek et al. 2020). At elevated temperatures, these hydrolysis products can undergo dehydration, leading to the formation of furans, aldehydes, and other intermediate compounds. These intermediate compounds then undergo condensation and polymerization reactions, ultimately forming solid carbonaceous materials that eventually become hydrochar. As the reaction progresses, these carbonaceous materials undergo further transformations, including aromatization and graphitization, which increase the carbon content and enhance the stability of the hydrochar. After the completion of the

**Table 1** Characteristics of biochars produced from various biomass sources via the pyrolysis process

| Biomass | Pyrolysis conditions | Biochar yield (wt.%) | Elemental composition (wt.%, dry basis) | | | Proximate composition (wt.%, dry basis) | | | pH | $S_{BET}$ (m² g⁻¹) | $V_T$ (cm³ g⁻¹) | References |
|---|---|---|---|---|---|---|---|---|---|---|---|---|
| | | | C | O | N | FC | VM | Ash | | | | |
| Sawdust | 500 °C, 18 °C min⁻¹, 4 h | 28.3 | 75.8 | 8.4 | 0.3 | 72.0 | 17.5 | 9.9 | 9.1 | 203.0 | 0.13 | Zhao et al. (2013); Zhao et al. (2014) |
| Grass | 500 °C, 18 °C min⁻¹, 4 h | 27.8 | 62.1 | 17.8 | 2.8 | 59.2 | 18.9 | 20.8 | 11.0 | 3.3 | 0.01 | |
| *Chlorella* | 500 °C, 18 °C min⁻¹, 4 h | 40.2 | 39.3 | 12.6 | 3.4 | 17.4 | 29.3 | 52.6 | 11.4 | 2.8 | 0.01 | |
| Wheat straw | 350 °C, 18 °C min⁻¹, 4 h | 52.5 | 59.8 | 22.1 | 0.6 | 53.2 | 31.3 | 14.7 | 8.7 | 3.5 | 0.01 | |
| | 500 °C, 18 °C min⁻¹, 4 h | 29.8 | 62.9 | 18.8 | 0.7 | 63.7 | 17.6 | 18.0 | 10.1 | 33.2 | 0.05 | |
| | 650 °C, 18 °C min⁻¹, 4 h | 26.8 | 68.9 | 17.1 | 0.5 | 72.1 | 11.1 | 16.2 | 10.2 | 182.0 | 0.09 | |
| Peanut shell | 500 °C, 18 °C min⁻¹, 4 h | 32.0 | 73.7 | 9.6 | 7.8 | 72.9 | 16.0 | 10.6 | 10.5 | 43.5 | 0.04 | |
| Cow manure | 500 °C, 18 °C min⁻¹, 4 h | 57.2 | 43.7 | 0.5 | 2.0 | 14.7 | 17.2 | 67.5 | 10.2 | 21.9 | 0.03 | |
| Bone dregs | 500 °C, 18 °C min⁻¹, 4 h | 48.7 | 40.2 | 9.6 | 3.1 | 10.5 | 11.0 | 77.6 | 11.3 | 113.0 | 0.30 | |
| Shrimp hull | 500 °C, 18 °C min⁻¹, 4 h | 33.4 | 52.1 | 0.7 | 5.6 | 18.9 | 26.6 | 53.8 | 10.1 | 13.3 | 0.04 | |
| Pig manure | 200 °C, 18 °C min⁻¹, 4 h | 98.0 | 37.0 | 27.2 | 1.3 | 12.6 | 50.7 | 35.7 | 8.2 | 3.6 | – | |
| | 350 °C, 18 °C min⁻¹, 4 h | 57.5 | 39.1 | 24.8 | 2.0 | 34.7 | 27.4 | 37.2 | 9.7 | 4.3 | 0.02 | |
| | 500 °C, 18 °C min⁻¹, 4 h | 38.5 | 48.7 | 15.3 | 2.3 | 40.2 | 11.0 | 48.4 | 10.5 | 47.4 | 0.07 | |
| | 650 °C, 18 °C min⁻¹, 4 h | 35.8 | 50.3 | 0.8 | 2.6 | 19.2 | 10.7 | 69.6 | 10.8 | 42.4 | 0.06 | |
| Wastepaper | 500 °C, 18 °C min⁻¹, 4 h | 36.6 | 58.8 | 2.1 | 1.6 | 16.4 | 30.0 | 53.5 | 10.0 | 133.0 | 0.08 | |
| Wastewater sludge | 500 °C, 18 °C min⁻¹, 4 h | 45.9 | 30.6 | 20.8 | 2.9 | 20.6 | 15.8 | 61.9 | 8.8 | 71.6 | 0.06 | |
| Rapeseed stem | 500 °C, 20 °C min⁻¹, 10 min | – | 74.5 | 12.4 | 1.1 | 66.4 | 23.7 | 8.0 | – | 46.7 | 0.05 | Zhao et al. (2018) |
| | 500 °C, 20 °C min⁻¹, 60 min | – | 74.1 | 10.8 | 1.1 | 68.1 | 19.6 | 10.7 | – | 98.4 | 0.11 | |
| | 500 °C, 20 °C min⁻¹, 100 min | – | 77.1 | 10.3 | 1.1 | 69.5 | 19.8 | 10.2 | – | 91.4 | 0.06 | |
| Pinewood | 450 °C, 450 °C min⁻¹, 30 s | 24.7 | 75.5 | 20.5 | 0.2 | 86.3 | 8.9 | 4.1 | – | 185.0 | 0.18 | Mohanty et al. (2013) |
| | 450 °C, 2 °C min⁻¹, 30 min | 44.5 | 81.4 | 15.3 | 0.3 | 86.4 | 8.2 | 4.6 | – | 166.0 | 0.17 | |
| Wheat straw | 450 °C, 450 °C min⁻¹, 30 s | 21.6 | 64.8 | 31.2 | 0.8 | 87.9 | 7.7 | 3.6 | – | 184.0 | 0.18 | |
| | 450 °C, 2 °C min⁻¹, 30 min | 41.2 | 65.2 | 31.5 | 0.9 | 88.1 | 7.2 | 3.9 | – | 178.0 | 0.18 | |
| Timothy grass | 450 °C, 450 °C min⁻¹, 30 s | 22.8 | 63.7 | 30.8 | 1.9 | 87.7 | 8.3 | 3.1 | – | 203.0 | 0.20 | |
| | 450 °C, 2 °C min⁻¹, 30 min | 43.8 | 67.5 | 28.2 | 1.9 | 88.4 | 7.5 | 3.5 | – | 179.0 | 0.19 | |
| Corn cob | 350 °C, 2 h | 32.3 | 67.7 | 22.0 | 1.3 | – | – | 4.1 | 9.5 | 15.6 | – | Yu et al. (2020b) |
| | 650 °C, 2 h | 22.9 | 72.2 | 15.9 | 1.0 | – | – | 8.1 | 9.8 | 44.4 | – | |
| Rice straw | 350 °C, 2 h | 42.8 | 46.6 | 17.7 | 1.1 | – | – | 30.5 | 9.0 | 24.1 | – | |
| | 650 °C, 2 h | 24.1 | 39.8 | 12.4 | 0.6 | – | – | 45.1 | 10.2 | 62.0 | – | |
| Wheat straw | 350 °C, 2 h | 36.6 | 62.9 | 19.8 | 1.3 | – | – | 11.3 | 9.1 | 13.8 | – | |
| | 650 °C, 2 h | 25.3 | 58.5 | 15.0 | 0.9 | – | – | 22.8 | 9.8 | 36.8 | – | |
| Wastewater sludge | 400 °C, 35 °C min⁻¹, 60 min, N₂; 7.5 L min⁻¹ | 54.7 | 21.4 | 20.4 | 3.3 | 22.5 | 22.8 | 53.1 | 7.5 | 7.6 | 0.04 | Aktar et al. (2022) |

**Table 1** (continued)

| Biomass | Pyrolysis conditions | Biochar yield (wt.%) | Elemental composition (wt.%, dry basis) | | | Proximate composition (wt.%, dry basis) | | | pH | $S_{BET}$ (m² g⁻¹) | $V_T$ (cm³ g⁻¹) | References |
|---|---|---|---|---|---|---|---|---|---|---|---|---|
| | | | C | O | N | FC | VM | Ash | | | | |
| | 400 °C, 35 °C min⁻¹, 60 min, $CO_2$; 7.5 L min⁻¹ | 54.1 | 20.6 | 18.0 | 3.2 | 22.2 | 20.0 | 55.7 | 6.5 | 11.1 | 0.06 | |
| | 500 °C, 35 °C min⁻¹, 60 min, $N_2$; 7.5 L min⁻¹ | 50.3 | 16.3 | 17.2 | 2.6 | 23.6 | 13.6 | 63.0 | 9.9 | 17.5 | 0.07 | |
| | 500 °C, 35 °C min⁻¹, 60 min, $CO_2$; 7.5 L min⁻¹ | 47.5 | 14.2 | 21.3 | 2.4 | 24.1 | 13.6 | 61.7 | 7.3 | 30.0 | 0.06 | |
| | 600 °C, 35 °C min⁻¹, 60 min, $N_2$; 7.5 L min⁻¹ | 46.2 | 14.2 | 18.5 | 2.0 | 24.3 | 10.2 | 64.3 | 11.3 | 32.0 | 0.06 | |
| | 600 °C, 35 °C min⁻¹, 60 min, $CO_2$; 7.5 L min⁻¹ | 46.2 | 13.2 | 20.2 | 2.1 | 25.0 | 10.1 | 64.3 | 8.1 | 45.5 | 0.06 | |
| Kentucky bluegrass | 350 °C, 2 h | 40.0 | 64.0 | 17.5 | 2.7 | – | – | 11.6 | 6.4 | 2.6 | 0.01 | Song et al. (2021) |
| | 550 °C, 2 h | 12.0 | 68.7 | 8.8 | 2.5 | – | – | 17.7 | 7.0 | 190.0 | 0.14 | |
| | 750 °C, 2 h | 8.0 | 69.0 | 6.4 | 2.2 | – | – | 21.6 | 7.1 | 118.0 | 0.04 | |
| Alfalfa | 350 °C, 10 °C min⁻¹, 2 h | 47.7 | 68.8 | 14.4 | 4.9 | 34.5 | 58.4 | 7.1 | 5.8 | 3.5 | – | Choi and Kan (2019) |
| | 450 °C, 10 °C min⁻¹, 2 h | 30.7 | 71.1 | 12.0 | 4.7 | 58.5 | 32.4 | 9.1 | 5.7 | 4.0 | – | |
| | 550 °C, 10 °C min⁻¹, 2 h | 28.3 | 69.5 | 8.7 | 4.0 | 53.3 | 30.7 | 16.0 | 6.1 | 183.0 | – | |
| | 650 °C, 10 °C min⁻¹, 2 h | 27.5 | 72.2 | 8.5 | 4.6 | 56.9 | 29.5 | 13.6 | 8.1 | 405.0 | – | |

HTC process, the hydrochar is isolated from the process water through filtration.

The primary product of interest in HTC is hydrochar, and a higher lignin content in the biomass precursor leads to an increased yield of hydrochar. Additionally, liquid by-products such as bio-oil and gaseous by-products like $CO_2$, $CH_4$, $H_2$, and others can undergo further processing for their utilization as biofuels or chemicals in the context of a circular economy (Cavali et al. 2023). For example, Mannarino et al. (2022) produced hydrochar from food waste through the HTC process (Fig. 5a). The resulting hydrochar possessed characteristics well-suited for use as a solid biofuel, boasting a higher heating value (HHV) of 23.7 MJ kg$^{-1}$. In the context of resource recovery and a circular economy approach, the process water resulting from HTC was subjected to anaerobic digestion (AD) to generate $CH_4$. Combusting both hydrochar and $CH_4$ yielded a notable energy recovery. In another study, Scrinzi et al. (2022) synthesized hydrochar by subjecting organic waste digestate to HTC, aligning with the principles of a circular economy. Figure 5b provides a visual representation of the process. The resulting hydrochars influenced the distribution of vital nutrients such as N and P. Notably, the hydrochar co-compost exhibited strong biological stability. Meanwhile, HTC liquors underwent testing in biochemical methane potential (BMP) assessments to evaluate their feasibility for recycling within AD. Recently, there has been a notable surge of interest in the utilization of microwave-assisted hydrothermal carbonization (MHTC) for the production of hydrochar. For instance, Wang et al. (2022b) utilized MHTC to produce hydrochar from sewage sludge (Fig. 5c). The resulting hydrochar displayed elevated porosity, with SSA of 24.0 m$^2$ g$^{-1}$ and TPV of 0.19 cm$^3$ g$^{-1}$.

Liang et al. (2022) produced hydrochars by subjecting forest waste to HTC at temperatures ranging from 200 to 280 °C in 20 °C intervals while maintaining a residence time of 1 h. Their findings indicated that as the HTC temperature increased, there was a gradual reduction in the yield of hydrochar, with the lowest yield recorded at 280 °C, amounting to 42.83%. The proximate and ultimate analyses of hydrochar demonstrated that as the HTC temperature elevated from 200 to 280 °C, the FC content and C element content increased from 19.67% to 45.08% and from 54.38% to 70.75%, respectively. This increase was attributed to the continuous release of VM during the HTC process. Simultaneously, the O element content gradually decreased from 31.39% to 19.95%, and the ash content decreased from 7.55% to 2.66% in the resulting hydrochars. The HHV of the hydrochar exhibited a gradual increase as the HTC temperature rose. At 280 °C, the hydrochar attained its peak HHV at

28.78 MJ kg$^{-1}$, which was 1.46 times greater than that of the initial biomass. The SSA of the hydrochar also expanded as the HTC temperature increased, peaking at 2.92 m$^2$ g$^{-1}$ when the temperature reached 240 °C. Nevertheless, as the HTC temperature was further increased to 280 °C, the SSA of the hydrochar decreased to 0.91 m$^2$ g$^{-1}$. The temperature plays a crucial role in HTC as it triggers a variety of complex reactions in the subcritical zones. Figure 6a illustrates how the hydrochar yield (%) is affected by the temperature (°C) during the HTC process. When the HTC temperature rises, the hydrochar yield diminishes, and this reduction is less pronounced at higher temperature levels. The most significant drop in hydrochar yield is observed between 150 and 250 °C. Regarding pH levels, despite showing an upward trend with rising temperature, hydrochars still maintained a slightly acidic to mildly alkaline nature, with pH values falling in the range of 6–8, as depicted in Fig. 6b. This stands in contrast to pyrolytic biochars, which have notably heightened pH characteristics. The pH of hydrochars is primarily influenced by the creation of organic acids during hydrolysis reactions (Yang et al. 2022a). According to Fig. 6c, the carbon content demonstrates a strong correlation with both HTC temperature and ash content, indicating the feasibility of precisely tailoring hydrochar with the desired carbon and ash content by modifying the HTC temperature. Figure 6d illustrates a ternary diagram representing the proximate composition of hydrochar, including FC, VM, and ash content. Figure 6e demonstrates that as the HTC temperature rises, there is a decrease in the atomic O/C and H/C ratios, which can be attributed to the extent of condensation and polymerization reactions. This transformation results in a shift of hydrochar towards greater aromaticity and improved stability (Fernández-Sanromán et al. 2021). The physicochemical and structural attributes of hydrochars derived from HTC processing of various biomass sources are summarized in Table 2.

### 2.2.1 Limitations of hydrothermal carbonization

Hydrothermal carbonization (HTC) is a promising technology for creating biochar from organic sources by subjecting them to high temperature and pressure conditions in the presence of water. However, it comes with certain limitations:

(1) HTC can be relatively time-consuming, taking several hours to complete. This slow kinetics can hinder its scalability for industrial-scale biochar production.

(2) Running HTC reactors at high pressures demands specialized equipment, which can be expensive to install and maintain.
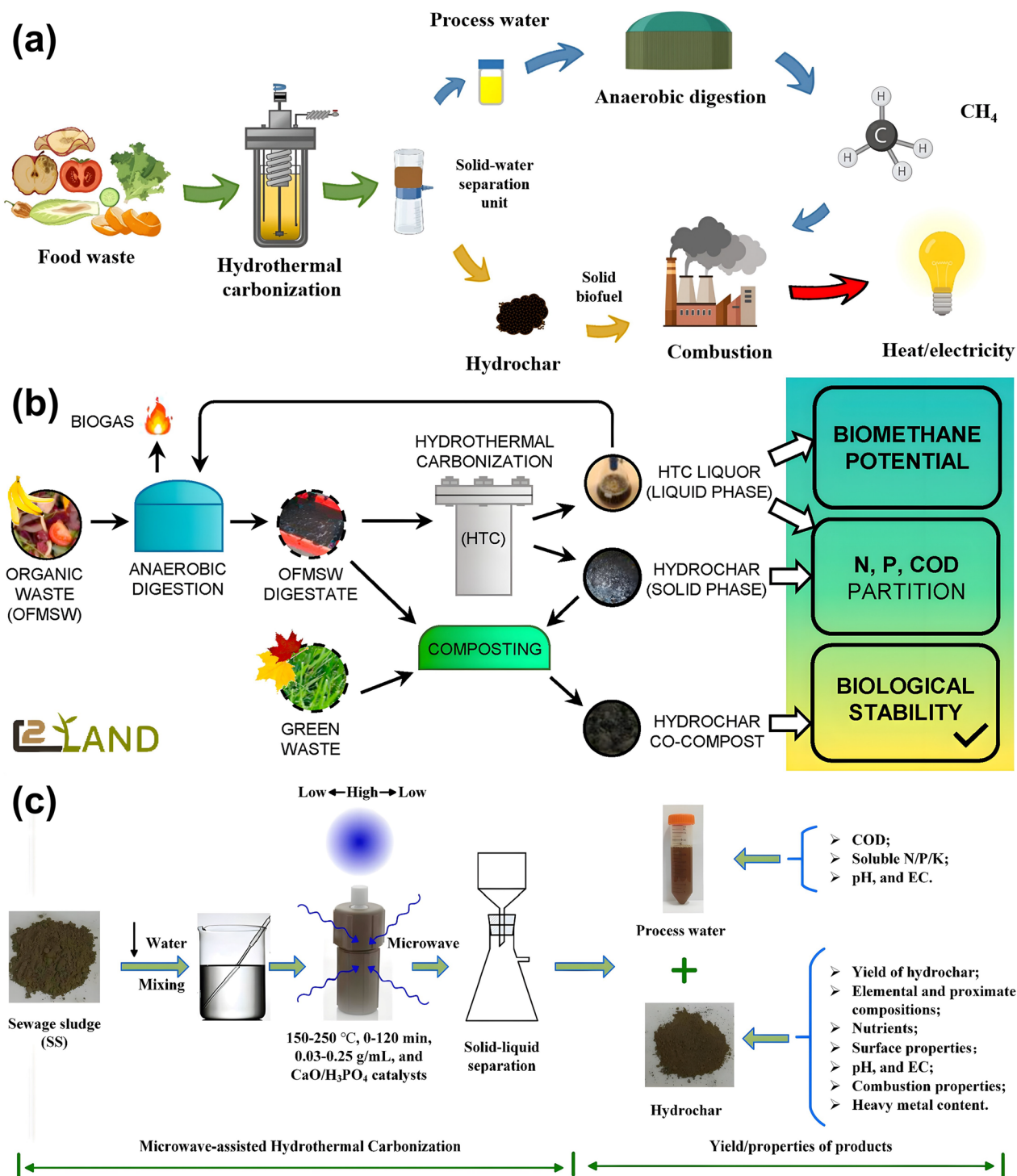
**Fig. 5  a** Hydrochar production from food waste via HTC process (Mannarino et al. 2022), Copyright © 2022, Elsevier. **b** HTC of organic waste digestate (Scrinzi et al. 2022), Copyright© 2022, Elsevier. **c** Hydrochar synthesis using microwave-assisted HTC process (Wang et al. 2022b), Copyright© 2022, Elsevier

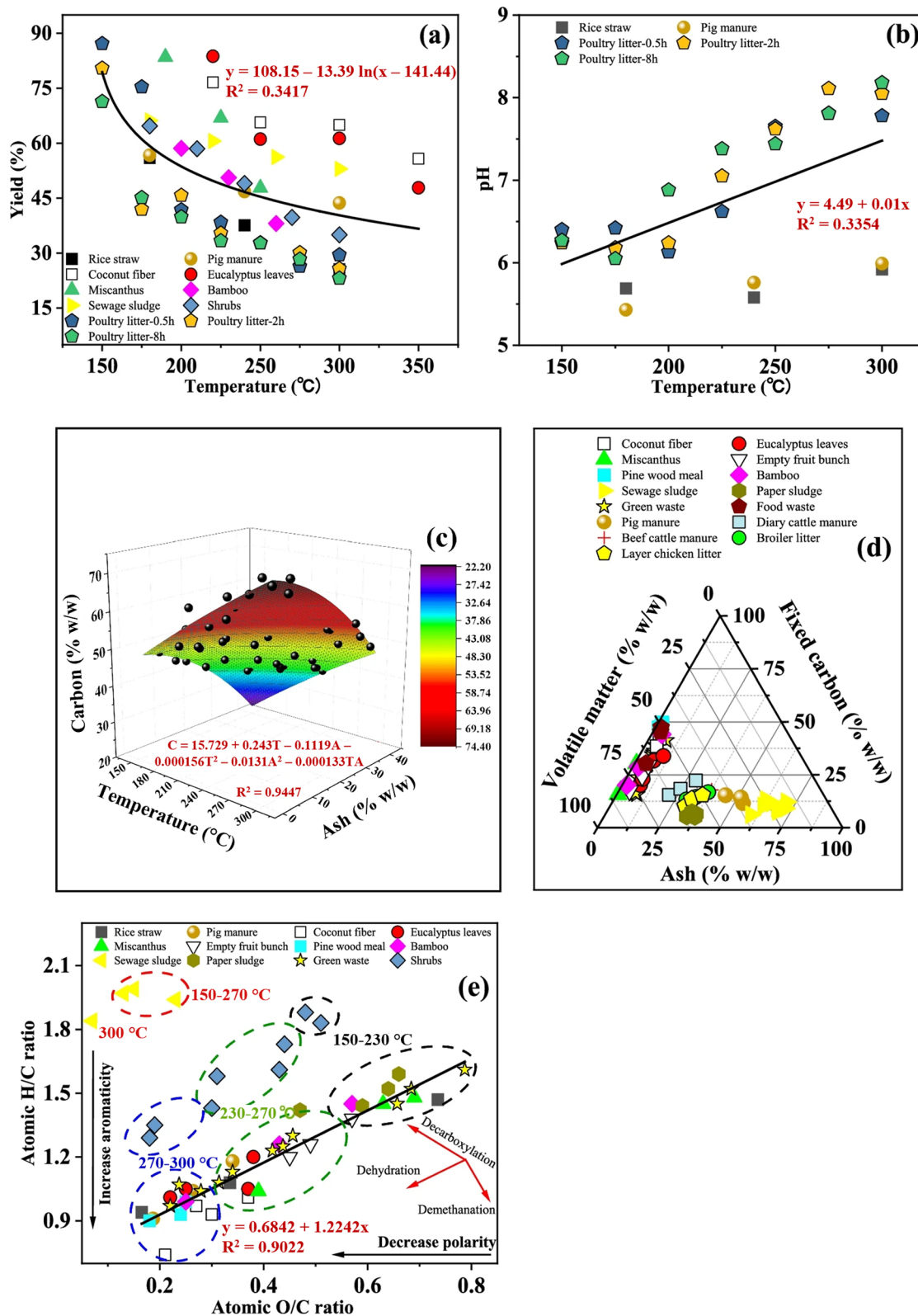**Fig. 6 a** Percentage yields and (**b**) pH trends of hydrochar; **c** Variation in the carbon content of hydrochar with temperature and ash content; **d** Ternary diagram illustrating ash content, volatile matter, and fixed carbon; **e** Van Krevelen diagram depicting hydrochar characteristics (Yang et al. 2022a), Copyright © 2022, The Authors, Springer Nature

**Table 2** Characteristics of hydrochar obtained from HTC processing of biomass

| Biomass | HTC conditions | Hydrochar yield (wt.%) | Elemental composition (wt.%, dry basis) | | | Proximate composition (wt.%, dry basis) | | | HHV (MJ kg$^{-1}$) | $S_{BET}$ (m$^2$ g$^{-1}$) | References |
|---|---|---|---|---|---|---|---|---|---|---|---|
| | | | C | O | N | FC | VM | Ash | | | |
| Forest waste | 200 °C, 1 h, 10 MPa | 69.9 | 54.4 | 31.4 | 0.8 | 19.7 | 72.8 | 7.6 | 22.2 | 2.3 | Liang et al. (2022) |
| | 220 °C, 1 h, 10 MPa | 63.9 | 58.2 | 30.6 | 0.8 | 23.3 | 71.9 | 4.8 | 23.5 | 2.7 | |
| | 240 °C, 1 h, 10 MPa | 53.2 | 60.7 | 27.4 | 0.9 | 30.9 | 63.6 | 5.5 | 24.6 | 2.9 | |
| | 260 °C, 1 h, 10 MPa | 45.8 | 67.8 | 21.1 | 0.9 | 39.7 | 55.7 | 4.7 | 27.7 | 1.7 | |
| | 280 °C, 1 h, 10 MPa | 42.8 | 70.8 | 19.9 | 1.2 | 45.1 | 52.3 | 2.7 | 28.8 | 0.9 | |
| Maize straw | 220 °C, 60 min, 30 MPa | 71.2 | 56.5 | 33.2 | 0.9 | 21.5 | 74.9 | 3.6 | 22.8 | 2.0 | Wang et al. (2020a) |
| | 250 °C, 60 min, 30 MPa | 51.6 | 66.8 | 25.3 | 1.1 | 38.4 | 60.3 | 1.3 | 27.0 | 3.7 | |
| | 280 °C, 60 min, 30 MPa | 35.8 | 73.0 | 18.1 | 1.4 | 47.3 | 50.7 | 2.1 | 29.9 | 2.4 | |
| | 310 °C, 60 min, 30 MPa | 28.9 | 75.8 | 16.1 | 1.3 | 53.6 | 44.8 | 1.6 | 30.8 | 1.8 | |
| | 340 °C, 60 min, 30 MPa | 27.2 | 77.4 | 14.2 | 1.6 | 59.1 | 39.1 | 1.9 | 31.2 | 1.5 | |
| | 280 °C, 15 min, 30 MPa | 45.8 | 71.4 | 19.4 | 1.6 | 46.2 | 51.6 | 2.1 | 29.2 | 2.5 | |
| | 280 °C, 30 min, 30 MPa | 37.6 | 72.5 | 19.2 | 1.2 | 46.4 | 52.0 | 1.7 | 29.6 | 2.4 | |
| | 280 °C, 90 min, 30 MPa | 35.6 | 73.2 | 18.4 | 1.4 | 48.7 | 49.8 | 1.6 | 29.8 | 2.0 | |
| | 280 °C, 120 min, 30 MPa | 35.3 | 73.5 | 18.2 | 1.3 | 51.3 | 47.1 | 1.6 | 29.9 | 1.8 | |
| Livestock manure | 250 °C, 60 min | 61.9 | 45.0 | 12.0 | 2.8 | 22.0 | 42.3 | 35.7 | 18.2 | – | Jang et al. (2022) |
| | 270 °C, 60 min | 58.1 | 46.1 | 7.0 | 2.7 | 23.0 | 37.1 | 39.9 | 18.8 | – | |
| | 300 °C, 60 min | 54.7 | 47.7 | 5.1 | 2.7 | 25.1 | 33.9 | 41.0 | 19.3 | – | |
| Municipal waste | 150 °C, 40 min, 10 bar | 61.5 | 52.9 | 35.4 | 5.1 | 25.8 | 69.0 | 5.3 | 20.4 | – | Abdoli and Ghasemzadeh (2024) |
| | 170 °C, 40 min, 10 bar | 59.5 | 54.4 | 33.6 | 4.6 | 26.4 | 66.9 | 6.7 | 22.5 | – | |
| | 190 °C, 40 min, 10 bar | 56.9 | 58.7 | 29.5 | 4.2 | 27.0 | 66.0 | 7.0 | 24.8 | – | |
| | 210 °C, 40 min, 10 bar | 52.7 | 61.9 | 26.3 | 4.3 | 29.7 | 65.1 | 5.2 | 26.4 | – | |
| | 230 °C, 40 min, 10 bar | 47.5 | 66.6 | 22.7 | 3.9 | 31.0 | 61.1 | 7.9 | 27.6 | – | |
| Oil palm trunk | 180 °C, 30 min | – | 51.4 | 40.6 | 0.0 | 13.0 | 82.4 | 1.9 | 19.6 | – | Prasongthum et al. (2023) |
| | 200 °C, 30 min | – | 53.4 | 38.1 | 0.1 | 17.2 | 80.4 | 2.4 | 19.9 | – | |
| | 220 °C, 30 min | – | 55.1 | 36.1 | 0.2 | 23.7 | 73.6 | 2.8 | 21.9 | – | |
| | 240 °C, 30 min | – | 62.4 | 28.6 | 0.3 | 34.1 | 62.7 | 3.2 | 24.1 | – | |
| | 180 °C, 60 min | – | 51.9 | 39.8 | 0.1 | 13.3 | 84.6 | 2.1 | 19.9 | – | |
| | 200 °C, 60 min | – | 54.8 | 36.9 | 0.2 | 19.7 | 78.2 | 2.2 | 21.8 | – | |
| | 220 °C, 60 min | – | 56.9 | 34.5 | 0.2 | 27.1 | 70.3 | 2.6 | 22.9 | – | |
| | 240 °C, 60 min | – | 66.3 | 24.8 | 0.5 | 41.3 | 55.5 | 3.2 | 26.4 | – | |
| Waste wood chip | 210 °C, 60 min | – | 56.6 | 37.2 | 0.4 | 22.4 | 77.7 | 0.7 | 22.6 | – | Wang et al. (2023b) |
| | 240 °C, 60 min | – | 66.8 | 27.6 | 0.4 | 40.7 | 59.3 | 1.6 | 26.2 | – | |
| | 270 °C, 60 min | – | 71.5 | 22.9 | 0.4 | 53.0 | 47.0 | 1.3 | 28.3 | – | |

**Table 2** (continued)

| Biomass | HTC conditions | Hydrochar yield (wt.%) | Elemental composition (wt.%, dry basis) | | | Proximate composition (wt.%, dry basis) | | | HHV (MJ kg$^{-1}$) | S$_{BET}$ (m$^2$ g$^{-1}$) | References |
|---|---|---|---|---|---|---|---|---|---|---|---|
| | | | C | O | N | FC | VM | Ash | | | |
| Loquat seeds | 150 °C, 2 h, 5 bar | 13.2 | 50.4 | 41.0 | 2.7 | 13.0 | – | 0.8 | 19.1 | – | Kalderis et al. (2023) |
| | 150 °C, 4 h, 5 bar | 15.0 | 54.3 | 37.4 | 2.5 | 15.9 | – | 0.8 | 20.9 | – | |
| | 150 °C, 6 h, 5 bar | 17.6 | 57.5 | 34.4 | 2.4 | 19.8 | – | 0.6 | 22.3 | – | |
| | 200 °C, 2 h, 20 bar | 26.9 | 61.5 | 30.5 | 1.8 | 32.4 | – | 1.8 | 23.6 | – | |
| | 200 °C, 4 h, 20 bar | 30.0 | 64.8 | 27.0 | 1.8 | 38.0 | – | 1.8 | 25.2 | – | |
| | 200 °C, 6 h, 20 bar | 31.6 | 66.9 | 24.8 | 1.9 | 41.3 | – | 1.7 | 26.3 | – | |
| | 250 °C, 2 h, 60 bar | 24.9 | 67.6 | 24.1 | 2.0 | 32.9 | – | 2.0 | 26.2 | – | |
| | 250 °C, 4 h, 60 bar | 24.5 | 70.2 | 20.8 | 2.0 | 33.6 | – | 2.3 | 27.9 | – | |
| | 250 °C, 6 h, 60 bar | 24.3 | 75.6 | 15.2 | 2.2 | 35.9 | – | 2.0 | 30.6 | – | |
| Water hyacinth | 180 °C, 30 min | 50.1 | 39.8 | 39.7 | 1.2 | 8.9 | 77.3 | 13.8 | 16.5 | – | Poomsawat and Poomsawat (2021) |
| | 200 °C, 30 min | 43.2 | 46.2 | 37.8 | 1.0 | 17.0 | 73.5 | 9.5 | 18.8 | – | |
| | 220 °C, 30 min | 37.8 | 51.4 | 33.4 | 0.9 | 26.1 | 64.8 | 9.2 | 20.1 | – | |
| Cattail leaves | 180 °C, 30 min | 50.3 | 53.0 | 36.4 | 0.7 | 25.1 | 70.6 | 4.4 | 20.6 | – | |
| | 200 °C, 30 min | 48.7 | 54.4 | 35.6 | 0.7 | 27.2 | 68.9 | 3.9 | 21.7 | – | |
| | 220 °C, 30 min | 42.9 | 55.8 | 34.8 | 0.7 | 29.3 | 67.4 | 3.4 | 22.2 | – | |
| Sewage sludge | 200 °C, 20 min, 2 MPa | – | 41.8 | 10.6 | 5.2 | 11.7 | 55.6 | 32.8 | 19.0 | – | He et al. (2015) |
| | 220 °C, 20 min, 2.6 MPa | – | 41.4 | 9.1 | 4.5 | 12.4 | 51.8 | 35.8 | 18.5 | – | |
| | 240 °C, 20 min, 3.8 MPa | – | 41.6 | 6.3 | 4.1 | 11.5 | 49.6 | 38.9 | 18.7 | – | |
| | 260 °C, 20 min, 5.0 MPa | – | 42.9 | 5.3 | 3.9 | 15.2 | 47.1 | 37.8 | 19.4 | – | |
| | 280 °C, 20 min, 7.0 MPa | – | 44.6 | 3.9 | 3.8 | 23.6 | 37.7 | 38.7 | 20.2 | – | |
| | 300 °C, 20 min, 9.3 MPa | – | 44.5 | 4.0 | 3.7 | 43.0 | 18.2 | 38.8 | 20.3 | – | |
| Coconut shell | 180 °C, 30 min | 73.3 | 54.4 | 38.5 | 0.3 | 22.7 | 77.2 | 0.1 | 23.0 | – | Cheng et al. (2022) |
| | 180 °C, 60 min | 70.4 | 60.2 | 32.4 | 0.5 | 21.3 | 78.7 | 0.0 | 25.8 | – | |
| | 200 °C, 30 min | 67.5 | 61.4 | 31.5 | 0.3 | 24.8 | 75.1 | 0.1 | 26.1 | – | |
| | 200 °C, 60 min | 66.1 | 64.4 | 28.1 | 0.5 | 26.2 | 73.7 | 0.1 | 27.9 | – | |
| | 220 °C, 30 min | 63.1 | 65.7 | 27.6 | 0.3 | 34.8 | 65.1 | 0.1 | 27.6 | – | |
| | 220 °C, 60 min | 59.2 | 68.8 | 24.1 | 0.5 | 35.5 | 64.5 | 0.0 | 29.4 | – | |

(3) HTC is best suited for high-moisture biomass feedstocks like sewage sludge, algae, and food waste. Dry biomass feedstocks may require pre-treatment with water to ensure effective carbonization, which can add complexity to the process.

(4) HTC-derived biochar often exhibits reduced surface area and porosity, which can impact its adsorption and catalytic properties, making it less suitable for certain applications that require high surface area and porosity.

In summary, the choice between pyrolysis and HTC depends on specific factors such as the desired biochar properties, feedstock characteristics, and the intended application. Pyrolysis offers higher biochar quality with increased carbon content and stability but is more energy-intensive, while HTC has advantages in lower-temperature processing and better handling of high-moisture feedstocks but may yield biochar with lower aromaticity. Table 3 provides a clear comparison of the advantages and shortcomings of these two prominent biochar production techniques.

**Table 3** Comparative analysis of pyrolysis and hydrothermal carbonization processes for biochar production

| Process | Advantages | Shortcomings |
|---|---|---|
| Pyrolysis | • High-quality biochar with good porosity and surface area<br>• Shortened processing time<br>• High carbon content and stability<br>• Generation of valuable byproducts (bio-oil, syngas)<br>• Simple and well-established technology | • High temperatures required (400–800 °C)<br>• Necessitates dry feedstock, which can be energy-intensive<br>• Requires significant heat input, leading to higher operating costs<br>• Limited control over biochar characteristics<br>• Loss of nutrients in the feedstock |
| Hydrothermal carbonization (HTC) | • Moderate temperatures (180–250 °C)<br>• Lower energy consumption (can utilize self-generated heat)<br>• Capable of handling wet biomass, avoiding the need for pre-drying<br>• Higher carbon retention efficiency<br>• Preserves more nutrients in the biochar | • Relatively longer process duration<br>• Inferior biochar quality with lower surface area and more ash<br>• Low degree of graphitization and aromaticity<br>• High-pressure requirements and reactor corrosion<br>• Large quantity of wastewater produced in the process |

## 3 Functionalization strategies for biochar

The raw biochar produced through pyrolysis or HTC typically exhibits unfavorable physicochemical and structural characteristics, including reduced pores, diminished surface area, and fewer surface functional groups, all of which can impact its performance in numerous applications. The following sections describe emerging biochar functionalization techniques, including (i) ball milling, (ii) templating, (iii) molten salt activation, (iv) chemical activation, (v) metal impregnation, (vi) heteroatom doping, (vii) plasma treatment, and (viii) electrospraying. These techniques aim to enhance the physicochemical properties (such as surface area, porosity, chemical functional groups, and thermal stability), electrochemical characteristics (like electrical conductivity, redox activity, and electrochemical stability), and surface active sites (such as Bronsted acid sites, Lewis acid sites, base sites, and redox sites) of raw biochar, leading to the development of highly active and porous functionalized biochar materials that demonstrate outstanding performance across various applications, including energy conversion and storage, wastewater treatment, and environmental remediation.

### 3.1 Ball milling

Ball milling is becoming increasingly popular as an environmentally friendly and economical technology for producing innovative biochar-based porous nanomaterials that exhibit enhanced physicochemical properties, garnering significant interest across various applications. The utilization of ball milling for the upcycling of biomass waste into high-quality biochar can promote sustainable development and the establishment of a circular economy. In this mechanochemical technology, the kinetic energy of the moving balls is transferred to the milled feedstock, resulting in the breaking of chemical bonds and leading to improved surface morphologies (Tiwari et al. 2022). The essential stages of the ball milling process are illustrated in Fig. 7. Both the macroscopic and microscopic characteristics impact the final biochar product's quality. Nonetheless, achieving the desired quality of biochar material through ball milling also depends on several operational parameters, such as milling type, ball size, vibrational amplitude, rotational type, milling medium, speed, duration, and feedstock-to-balls ratio (Shen et al. 2020). It is equally essential to fine-tune the operational parameters of ball milling to enable cost-effective large-scale production of biochar-based nanomaterials that align with specific applications. Moreover,
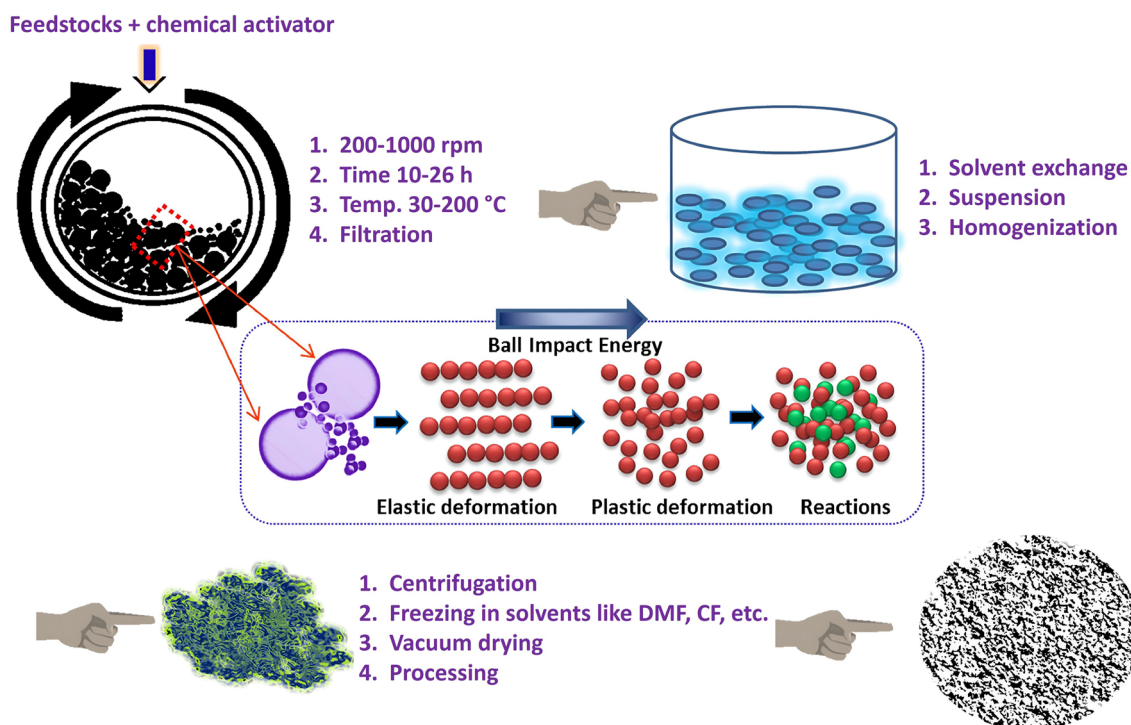
**Fig. 7** General layout of the ball milling process for the fabrication of biochar-based nanomaterials (Tiwari et al. 2022), Copyright © 2022, The Authors, Elsevier

the high-energy ball milling process can occasionally generate localized temperatures exceeding 100 °C and localized pressures reaching several MPa. These elevated temperature and pressure conditions can be employed for the synthesis of micro- and nano-sized biochar particles (Xing et al. 2013). In a study conducted by Kumar et al. (2020), the authors outlined the latest developments in employing a ball milling approach to produce cost-effective and eco-friendly biochar-based nanomaterials with a high surface area, a good porous structure, various functional groups, and an improved particle size distribution. They also explored a range of operational parameters, including milling type, processing time, and feedstock-to-balls ratio, which affect the physicochemical characteristics and potential applications of ball-milled biochar.

### 3.1.1  Limitations of ball milling
Ball milling represents a greener approach for producing biochar-based nanomaterials from biomass resources. Nevertheless, there are some recognized limitations associated with this method, including:

(1) The purity and uniformity of the ball-milled biochar can vary due to disparities in the hardness and particle size of the input materials and milling balls within the container. To circumvent these issues, it is advisable to employ appropriate pre-treatment procedures and use feedstock with comparable hardness and mineral composition.

(2) There is a lack of control over particle morphology, leading to the formation of agglomerates and the presence of residual strain, especially when dealing with crystalline nanoparticles.

(3) Challenges in accurately measuring temperature, pressure, and friction between the ball and feedstock during processing necessitate further theoretical investigations.

### 3.2 Templating
Biochar produced through HTC or pyrolysis processes often displays fewer pores, leading to a diminished surface area, which can impact its performance in numerous applications. Although raising the carbonization temperature can increase the surface area, it may compromise the surface's functional properties. Therefore, alternative methods are needed, and one effective approach is utilizing a template to generate the desired porous structure (Chen et al. 2022).

The template-directed carbonization process can be divided into the following three stages:

(1) Initial preparation of reaction precursors, which includes the template and biomass source.
(2) The carbonization process.
(3) The removal of the template to obtain porous bio-carbon.

One of the key benefits of this approach lies in its capacity to create well-organized porous structures based on different templates, a feat not attainable through activation methods. The templating method can be classified into two main categories: soft templates and hard templates (Castro-Gutiérrez et al. 2020), as depicted in Fig. 8a.

### 3.2.1 Soft templates
Soft templates are organic substances capable of generating mesoporous carbon materials with a hierarchically porous structure through their interaction with biomass precursors. By exclusively employing organic materials in the soft template process, one can obtain chemically pure carbon materials characterized by precisely controlled porous structures (Xu et al. 2023). Examples of soft templates include surfactants, block copolymers, and ionic micelles. When these compounds come into contact with carbon precursors, they undergo self-assembly to create micelles. This self-assembly occurs through a combination of hydrogen bonding, hydrophobic or hydrophilic interactions, and electrostatic forces, resulting in a coating on the precursor material (Kaur et al. 2022). Upon carbonization, these templates decompose, leaving behind a porous structure in the resulting carbon materials. Importantly, this approach eliminates the need for using toxic chemicals to remove the templates. Given the thermal instability of soft templates, a common approach for creating hierarchically porous carbon is to carry out carbonization at relatively low temperatures. For instance, Chu et al. (2022) employed a surfactant-templated method to create mesoporous carbons from lignin, a biomass source. The schematic representation for the synthesis of surfactant-templated mesoporous carbons is illustrated in Fig. 8b. The resulting carbon materials exhibit distinctive characteristics, including an SSA of 418 $m^2$ $g^{-1}$ and a TPV of 0.34 $cm^3$ $g^{-1}$.

### 3.2.2 Hard templates
Hard templates refer to inorganic porous solids, including substances like zeolites, silica, metal oxides, clay materials, and metal–organic frameworks (Zhu et al.
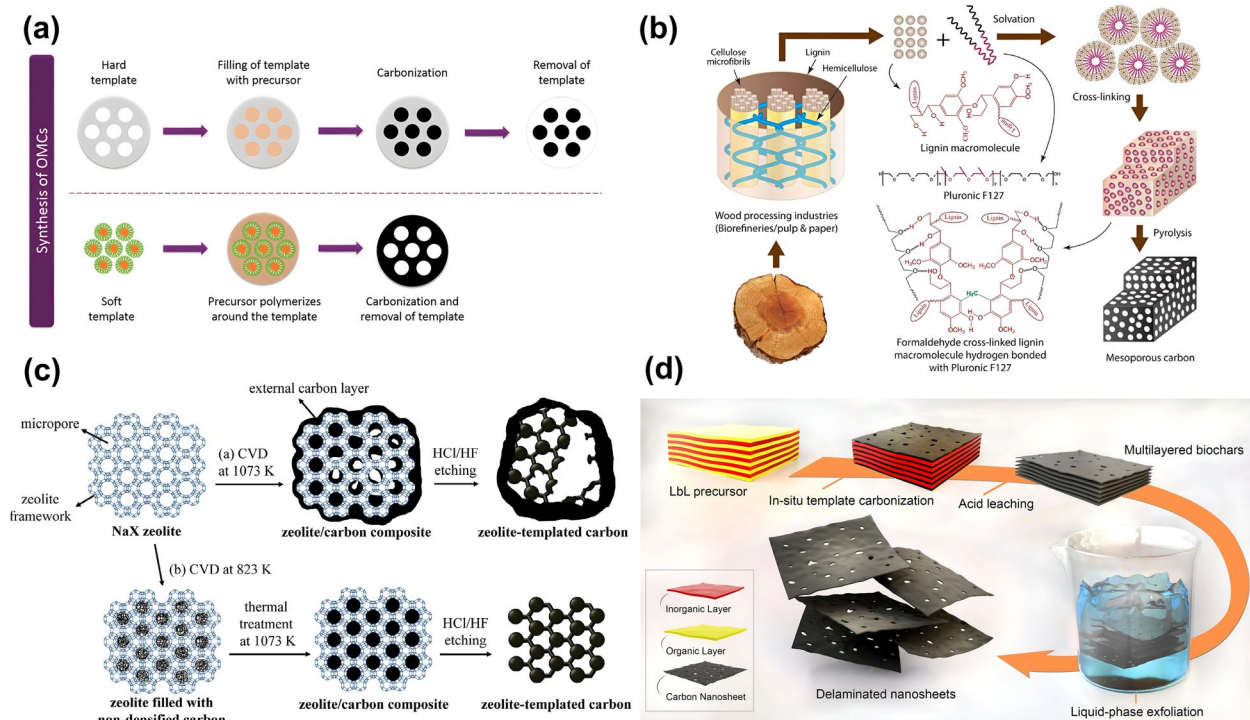


**Fig. 8** **a** Illustration of mesoporous carbons synthesis utilizing hard and soft template techniques (Castro-Gutiérrez et al. 2020), Copyright © 2020, The Authors, Frontiers. **b** Production of mesoporous carbon via soft template method (Chu et al. 2022), Copyright© 2022, Elsevier. **c** Fabrication of zeolite-templated carbon using hard template technique (Choi et al. 2015), Copyright© 2015, Elsevier. **d** Carbon nanosheets synthesis via in-situ template carbonization (Tian et al. 2021), Copyright© 2021, Elsevier

2019). Among these, silica stands out as the most frequently employed template. The fundamental concept behind the hard template method involves introducing monomer templates into biomass precursors through physical or chemical means. After the carbonization process and the subsequent removal of the templates, porous biocarbon materials are achieved. The chosen template enables the tailoring of the porous structure in the biocarbon materials. Unlike soft templates, hard templates are resistant to decomposition during the carbonization process. Consequently, post-treatment procedures like acid and water washing are typically required to eliminate any remaining template residue (Hsu et al. 2022). For instance, Choi et al. (2015) employed a chemical vapor deposition technique to produce top-notch zeolite-templated carbons (Fig. 8c). These newly synthesized carbons, known as ZTCs, exhibited remarkable characteristics, including SSA of over 2700 $m^2$ $g^{-1}$ and TPV exceeding 1.10 $cm^3$ $g^{-1}$. These properties allowed these carbon materials to surpass conventional activated carbons in terms of electrochemical performance and gas adsorption capabilities. In another study, Tian et al. (2021) synthesized Fe, N, S co-doped graphene-like carbon nanosheets using an in situ templated carbonization process, which was facilitated by the presence of well-arranged inorganic layers composed of $CaCO_3$ and $Fe_3C$. The schematic representation of the method for synthesizing these carbon nanosheets is illustrated in Fig. 8d. To eliminate the template layers, they employed acid leaching, resulting in the formation of delaminated biochars. Subsequently, these biochar layers underwent a liquid-phase exfoliation process to produce delaminated carbon nanosheets. Table 4 provides an overview of the

synthesis of porous carbon materials using the hard template-directed carbonization technique.

### 3.2.3 Limitations of templating method

The templated carbonization process employs soft or hard templates to produce structured biochar. While this method has its benefits, it also presents certain drawbacks:

(1) Choosing an appropriate template material is crucial for achieving the desired pore structure and biochar properties. The selection of the template material should be based on its compatibility with the feedstock and the intended application of the biochar.
(2) Removing templates after carbonization can pose challenges and may necessitate additional treatments, resulting in time delays and potential alterations to the final biochar properties.
(3) Incomplete removal of the template material can leave behind residue in the biochar, which can alter its physicochemical characteristics and potentially impact its suitability for specific applications.
(4) Although templating allows for structural control, achieving precise control over the incorporation of specific functional groups onto the biochar surface can be a demanding task.

### 3.3 Molten salt activation

Molten salt activation aims to streamline the biomass conversion process by consolidating it into a single thermochemical stage, which involves in situ activation through exposure to heat within a molten salt system. During this process, the thermal instability of biomass

**Table 4** Hard template-directed synthesis of porous carbon materials

| Biomass precursor | Template | Carbonization temperature (°C) | Template removal | $S_{BET}$ ($m^2$ $g^{-1}$) | $V_T$ ($cm^3$ $g^{-1}$) | References |
|---|---|---|---|---|---|---|
| Cornstalk | $CaCO_3$ | 800 | 1 M HCl and DI water washing | 2054 | 1.38 | Li et al. (2020b) |
| Almond | Poly-methyl methacrylate | 800 | 50 wt.% HCl washing | 1878 | 0.67 | Zeng et al. (2019) |
| Rice starch | Mesoporous $SiO_2$ | 900 | 5 wt.% HF washing | 488 | 1.14 | Wahab et al. (2018) |
| Lotus seed shell | $Na_2CO_3$ and $Na_3PO_4$ | 650 | HCl and DI water washing | 3188 | 3.20 | Hu et al. (2018) |
| Chitosan | $AlCl_3.6H_2O$ | 700 | 6 wt.% HCl and water washing | 554 | 0.78 | Jiang et al. (2019b) |
| Gelatin | Mesoporous $SiO_2$ | 800 | 10 wt.% HF washing | 818 | 1.05 | Qu et al. (2019) |
| Soybean milk powder | $CaCO_3$ nanospheres | 700 | 1 M HCl and DI water washing | 1208 | 0.70 | Chen et al. (2019) |
| Heavy fraction of bio-oil | Crayfish shell | 400 | Excess dilute HCl washing | 3095 | 1.66 | Luo et al. (2021) |
| Biomass pyrolysis oil | ZnO | 900 | 3 M HCl and DI water washing | 1770 | – | Hsu et al. (2022) |

can lead to its decomposition into solid (biochar), liquid (bio-oil), and gaseous (syngas) constituents, and this breakdown can be further enhanced by the impact of the ionic environment in the molten salt system (Yin et al. 2022). The resulting carbon material possesses a significant SSA, a well-structured pore arrangement, O-containing surface functional groups, and incorporated metal ions like $Na^+$, $Li^+$, $Mg^{2+}$, etc., making it suitable for a wide range of applications, including heterogeneous catalysis, wastewater treatment, $CO_2$ adsorption, and energy storage (Tiwari et al. 2022). To create the molten salt system, inorganic salts (such as alkali and alkaline earth metal halides, nitrates, carbonates, silicates, phosphates, etc.) are mixed in specific proportions (Zhu et al. 2023b). Molten salts offer advantages due to their ready availability, cost-effectiveness, favorable thermal stability, low vapor pressure, and efficient capacity to dissolve various impurities from biomass feedstock. Their high thermal conductivity and liquid nature allow for the efficient dispersion and rapid heating of biomass particles, thereby promoting the catalytic conversion process. Additionally, the ions in the molten salt system serve as pore-generating agents, allowing for the fine-tuning of both the microstructure and physicochemical characteristics of biocarbon materials (Xie et al. 2020). This phenomenon

occurs exclusively when the salt is in a molten state, above its melting point. Therefore, the use of salts with lower melting points will be necessary to minimize energy requirements. The utilization of salt ions, particularly cations, to enhance the reaction rate was validated through the use of carbonate salts. The results indicated a fourfold increase in the reaction rate when $Na_2CO_3$ and $K_2CO_3$ were mixed and a fivefold increase when $Li_2CO_3$ was employed. The alkali metals function as catalysts, facilitating the breaking of chemical bonds within the biomass components. This enhances reactivity, reduces conversion time, and allows for the creation of functionalized biochar in a single, on-the-spot activation step, while also incorporating the desired functional groups into the resulting biochar product (Zhou et al. 2023).

Numerous studies have explored the use of the molten salt activation process to develop functionalized biocarbon materials. For example, Yang et al. (2022b) fabricated porous carbon material derived from wood sawdust through a one-step molten salt carbonization and activation strategy using a combination of LiCl and KCl salts (Fig. 9a). The resulting carbon material exhibited a hierarchically microporous structure with a SSA of 614 $m^2 g^{-1}$, a TPV of 0.33 $cm^3 g^{-1}$, and an APD of 2.15 nm. In a study by Jia et al. (2020), N, S co-doped carbon
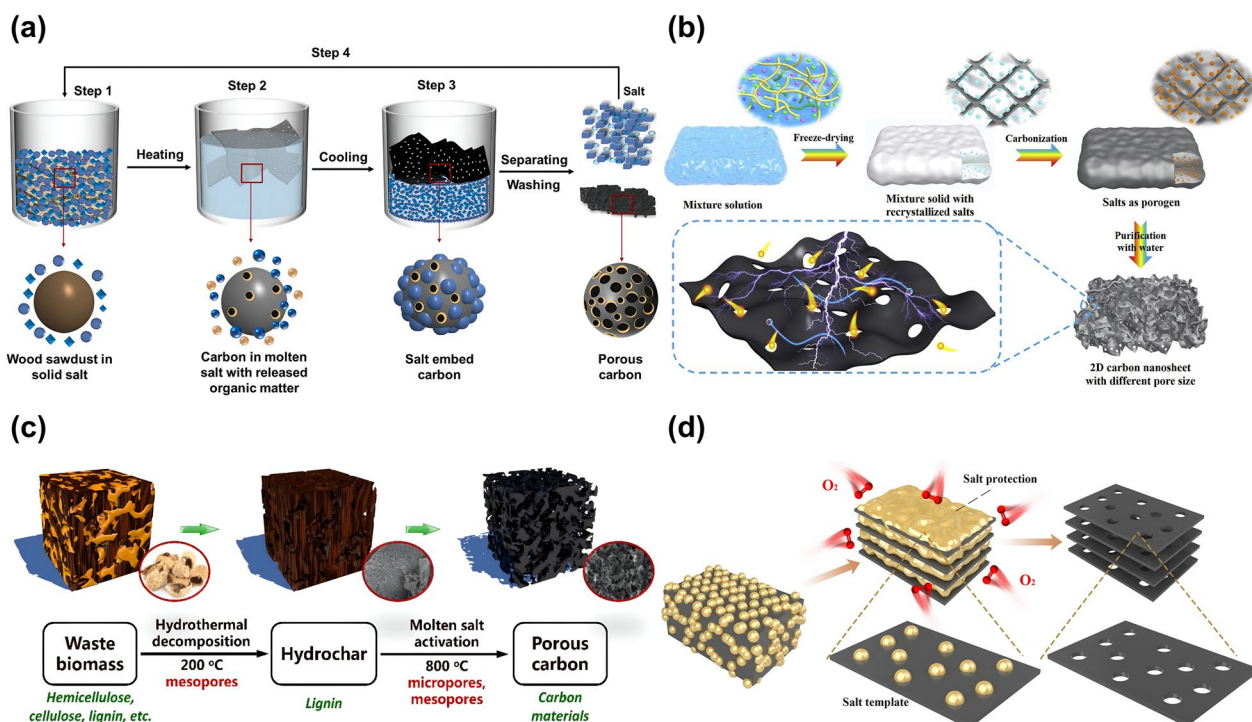


**Fig. 9 a** Schematic representation of porous carbon fabrication utilizing LiCl and KCl molten salts (Yang et al. 2022b), Copyright [©] 2022, Elsevier. **b** Synthesis of porous carbon sheets with KCl and $KNO_3$ molten salts (Jia et al. 2020), Copyright[©] 2020, Elsevier. **c** Molten salt activation of hydrochar using $Na_2CO_3$ and $K_2CO_3$ (Lei et al. 2021), Copyright[©] 2021, Elsevier. **d** Synthesis process for carbon nanosheets preparation with NaCl/KCl molten salt activator (Xue et al. 2021), Copyright[©] 2021, Elsevier

nanosheets resembling graphene were created using a molten salt activation technique (Fig. 9b). In this process, inorganic salts like KCl and $KNO_3$ served a dual role as templates and activating agents. The resulting biocarbon exhibited a hierarchical pore structure and a substantial SSA of 1753 $m^2$ $g^{-1}$. These characteristics facilitated the diffusion of electrolyte ions and charge transfer, ultimately leading to outstanding electrochemical performance in supercapacitors. In another study conducted by Lei et al. (2021), heteroatom-doped porous carbon was fabricated from peanut shell biomass using a combination of carbonization and molten salt activation processes (Fig. 9c). This was achieved by initially employing HTC to produce hydrochar and subsequently activating the hydrochar at 800 °C using a molten salt system composed of $Na_2CO_3$ and $K_2CO_3$ to produce porous carbon. The resulting biocarbon material exhibited a noticeably higher SSA, reaching as much as 1138 $m^2$ $g^{-1}$, along with a well-defined porous structure and a moderate level of heteroatom doping (O = 5.35 at.% and N = 1.02 at.%). These characteristics provided additional active storage sites and enhanced charge capacities. Deng et al. (2015) synthesized nitrogen-doped porous carbon from chitosan through a one-step molten salt carbonization and activation procedure. They created a hierarchically porous carbon material at 600 °C, which exhibited a SSA of 1582 $m^2$ $g^{-1}$, a substantial carbon content of 42 wt.%, and a notable nitrogen content of 9 wt.%. The molten salt used, $ZnCl_2$, was subsequently reclaimed at the end of the process. These porous carbon materials were then employed as high-performance electrodes in supercapacitors. Qi et al. (2020) generated porous ultrathin carbon nanosheets from agaric biomass using a reusable molten salt mixture composed of LiCl and KCl. These carbon nanosheets were utilized as anode materials for storing lithium and demonstrated improved specific capacity (795 mAh $g^{-1}$ at 0.1 A $g^{-1}$) along with exceptional cyclic stability (no capacity deterioration after 1000 cycles at 1 A $g^{-1}$). In a study by Xue et al. (2021), 2D porous carbon sheets were created from rice husk biomass through the use of a recyclable NaCl/KCl molten salt activator (Fig. 9d). The resulting porous carbon, when employed as an electrode material, featured a significant surface area with numerous open and easily accessible mesopores. It demonstrated a high capacitance of 288 F $g^{-1}$ at 0.5 A $g^{-1}$ and exhibited remarkable electrochemical stability, making it suitable for supercapacitors.

### 3.3.1 Limitations of molten salt activation
The molten salt activation is associated with certain limitations, which can be summarized as follows:

(1) It typically necessitates high temperatures, leading to elevated energy consumption and operational costs.
(2) The recycling of salts can pose significant challenges.
(3) The use of corrosive salts carries the risk of equipment corrosion.
(4) Reaction pathways can be unpredictable, leading to various by-products.
(5) Residual salt left on the biochar after activation can be problematic, potentially affecting the biochar's performance or necessitating additional treatment steps for removal.

### 3.4 Chemical activation
Biochar can undergo chemical activation using alkali hydroxides (e.g., KOH and NaOH), acids (e.g., $H_3PO_4$ and $H_2SO_4$), carbonate salts (e.g., $K_2CO_3$ and $Na_2CO_3$), or zinc chloride ($ZnCl_2$), either a one-step or two-step process, as depicted in Fig. 10. Chemical activation necessitates both the physical mixing of the activating agent with the carbon source and the subsequent elimination of any remnants of the activating agent after the activation process (Khan et al. 2021). During chemical activation, the activating agents penetrate the internal structure of the carbon precursor, triggering cross-linking polycondensation reactions between the carbon framework and the activating agents (Kazemi Shariat Panahi et al. 2020). Chemical activation is often recommended for creating top-notch porous carbons with well-defined pore structures and a significant SSA, thanks to its brief reaction duration and moderate operating temperature. In contrast to physical activation, chemical activation results in notably enhanced SSA, increased PV, and greater mesoporosity. This is because the formation of pores occurs through multiple chemical reactions during the activation process (Hameed et al. 2022). For instance, Wei et al. (2019) produced yeast-derived highly porous carbon using KOH activation at 850 °C for 1 h. They observed that the resulting porous carbon material exhibited an exceptionally high SSA of 3808 $m^2$ $g^{-1}$ and a TPV of 2.20 $cm^3$ $g^{-1}$. The chemical activation of biochar primarily leads to changes in its oxygen-related functional groups, notably carbonyl (C=O), hydroxyl (–OH), and carboxyl (–COOH). These functional groups are known to have a substantial impact on improving biochar's catalytic and adsorption characteristics. Introducing O-containing functional groups to the biochar's surface also enhances its affinity for water and boosts its overall performance in liquid-phase applications (Naqvi et al. 2023). The extent of porosity in the resultant porous carbon materials is
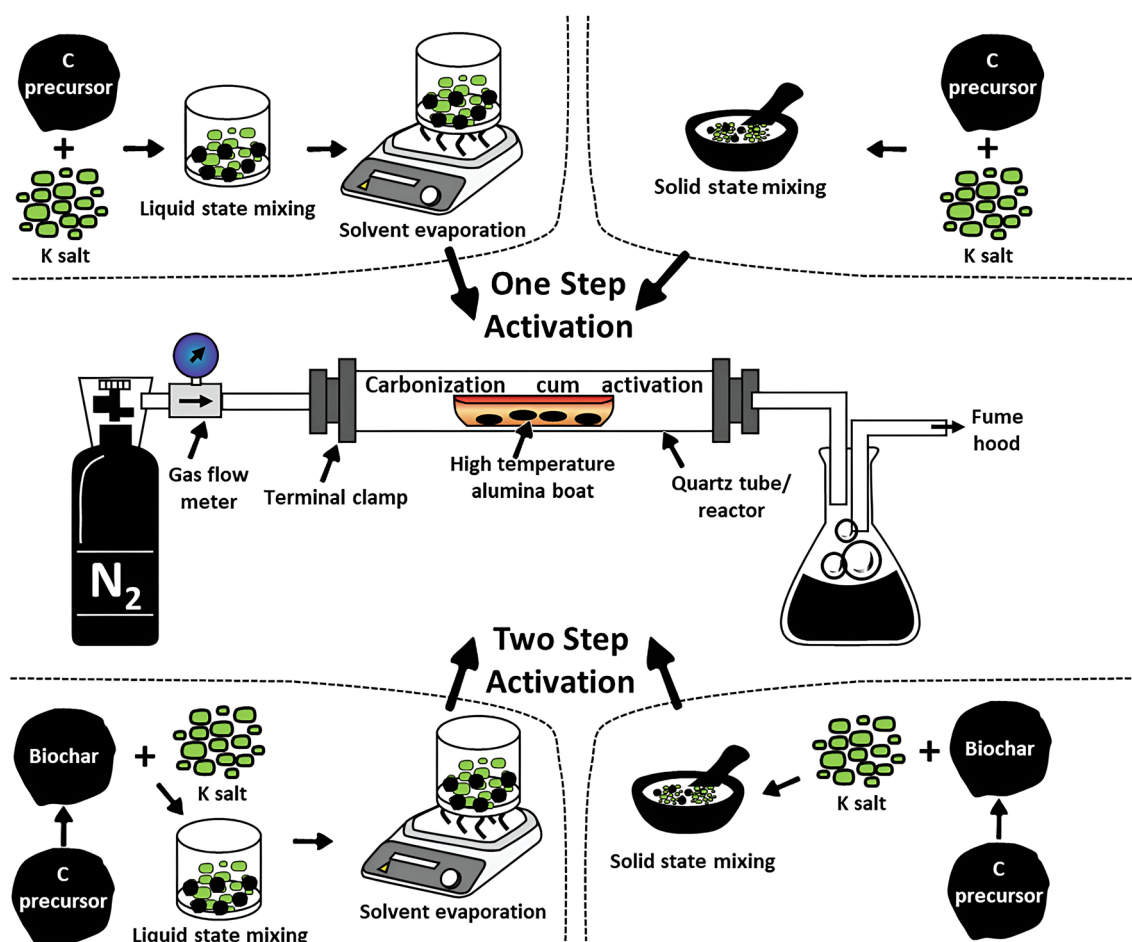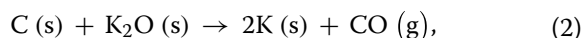
**Fig. 10** Approaches for producing porous functionalized biochar using chemical activation method (Singh et al. 2023), Copyright © 2023, Elsevier

influenced by both the chosen activating agent and process parameters, as well as the characteristics of the biomass used.

KOH stands out as the most prevalent and efficient activation agent for creating carbon structures with micro and mesopores (Yuan et al. 2022). It is capable of generating porous biochar materials with an extremely high SSA exceeding 3000 m$^2$ g$^{-1}$. The formation of a porous biochar with a well-defined hierarchical porous structure containing numerous micropores and mesopores during KOH activation is credited to the chemical reactions outlined in Eqs. (1)–(3) (He et al. 2023).

$$C\ (s)\ +\ 4KOH\ (s)\ \rightarrow\ K_2CO_3(s)\ +\ K_2O\ (s)\ +\ 2H_2(g),$$

$$C\ (s)\ +\ K_2O\ (s)\ \rightarrow\ 2K\ (s)\ +\ CO\ (g), \tag{2}$$

$$K_2CO_3(s)\ +\ 2C\ (s)\ \rightarrow\ 2K\ (s)\ +\ 3CO\ (g). \tag{3}$$

Sun et al. (2019a) synthesized KOH-activated porous carbon derived from the spongy flesh of sunflowers, which exhibited outstanding SSA and TPV values of 3072 m$^2$ g$^{-1}$ and 1.77 cm$^3$ g$^{-1}$, respectively. Similarly, Wei et al. (2018) reported that KOH-activated porous carbon derived from water chestnut had an ultra-large SSA of 3401 m$^2$ g$^{-1}$ and a TPV of 2.50 cm$^3$ g$^{-1}$. These findings indicate that chemical activation plays a significant role in the creation of top-notch porous carbons characterized by an improved SSA. Acid activation can remove surface impurities and ash from raw biochar while enhancing its porosity characteristics, particularly by augmenting the number of micropores and substantially raising its SSA (Naqvi et al. 2019). For instance, treating raw biochar with HCl boosted its SSA from 289 to 347 m$^2$ g$^{-1}$ (Mahmoud et al. 2012). Furthermore, acid treatment can also increase the presence of O-containing functional groups, thereby augmenting biochar's catalytic and adsorptive capabilities (Qin et al.

2020). The exact mechanism of $ZnCl_2$ activation is currently unclear (He et al. 2023). One theory suggests that when carbon precursors are impregnated with $ZnCl_2$ during activation, a dehydration process occurs. This, in turn, causes the carbon structure to undergo charring and aromatization, ultimately leading to the formation of the porous structure (He et al. 2023).

Figure 11 illustrates the comparison of SSA and mesoporosity for engineered biochar materials derived from different biomass sources. These engineered biochar materials are categorized into four groups based on their SSA and mesoporosity characteristics. Group I (e.g., biochar derived from basswood, loofa sponge, artemia cyst shell, etc.) has an SSA below 2000 $m^2\ g^{-1}$ and less than 40% mesoporosity. Group II (e.g., biochar derived from fishbone, rice husk, wood powders, etc.) exhibits an SSA below 2000 $m^2\ g^{-1}$ and mesoporosity exceeding 40%. Group III (e.g., biochar derived from peanut shells, chestnut, soybean root, etc.) features an SSA greater than 2000 $m^2\ g^{-1}$ and less than 40% mesoporosity. Lastly, Group IV (e.g., biochar derived from mixed crab shell and rice husk, *E. prolifera*, barley, etc.) exhibits an ultra-high SSA exceeding 2000 $m^2\ g^{-1}$ and mesoporosity higher than 40%. Table 5 summarizes various functionalized biochar materials derived from biomass sources using the chemical activation method,

along with their corresponding porosity features. In general, alkali-treated biochar is expected to exhibit a larger SSA and a more pronounced presence of surface graphitic carbon and aromatic functional groups (such as C=O, –OH, and –COOH), compared to biochar that undergoes acid or $ZnCl_2$ treatment.

### 3.4.1 Limitations of chemical activation

Chemical activation involves treating pristine biochar with chemical agents to produce porous activated carbon with improved physicochemical characteristics. While this approach offers several benefits, it also comes with certain limitations:

(1) The utilization of chemical agents, particularly strong acids and alkalis, can result in significant corrosion of the equipment, necessitating thorough cleaning to remove excessive residue that can have adverse environmental effects.
(2) Dealing with strong chemicals like HCl, $HNO_3$, $H_3PO_4$, or KOH can be hazardous, requiring proper safety precautions and equipment to avoid accidents.
(3) Achieving precise control over the creation of well-organized porous structures remains a challenging task in chemical activation techniques.
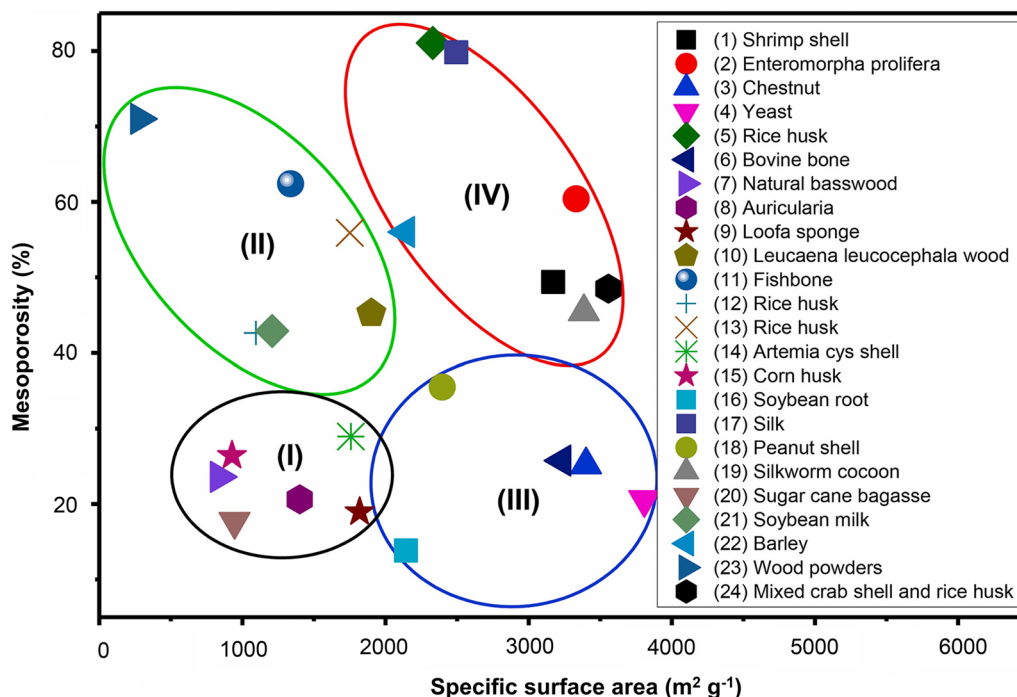


**Fig. 11** Surface area and pore size characteristics of engineered biochars derived from different biomass resources (Cuong et al. 2021), Copyright © 2021, Elsevier

**Table 5** Porosity characteristics of functionalized biochar materials prepared through the chemical activation method

| Biomass | Carbonization | | | Activation | | | $S_{BET}$ ($m^2\ g^{-1}$) | $V_T$ ($cm^3\ g^{-1}$) | References |
|---|---|---|---|---|---|---|---|---|---|
| | Technique | $T_c$ (°C) | $t_c$ (h) | Agent | $T_a$ (°C) | $t_a$ (h) | | | |
| Soybean root | Pyrolysis | 500 | 2 | KOH | 800 | 2 | 2143 | 0.94 | Guo et al. (2016) |
| Shrimp shell | Pyrolysis | 400 | 2 | KOH | 850 | 1 | 3171 | 1.93 | Qin et al. (2016) |
| Loofa sponge | Pyrolysis | 600 | 1 | KOH | 800 | 1 | 1819 | 0.95 | Feng et al. (2018a) |
| Kelp | Pyrolysis | 700 | 1 | KOH | 800 | 2 | 2614 | 1.40 | Sun et al. (2019b) |
| Pomelo peels | Pyrolysis | – | – | $ZnCl_2$ | 500 | 2 | 1361 | 1.57 | Lin et al. (2020) |
| Soybean hulls | Pyrolysis | 800 | 2 | KOH | 700 | 2 | 1232 | 0.54 | Zhu et al. (2017) |
| *Enteromorpha prolifera* | Pyrolysis | 500 | 1.5 | KOH | 750 | 1 | 3332 | 2.46 | Gao et al. (2014) |
| *Auricularia auricula* | HTC | 180 | 12 | KOH | 850 | 2 | 1401 | 0.90 | Feng et al. (2018b) |
| Olive tree pruning | Pyrolysis | 500 | 2 | $K_2CO_3$ | 800 | 1 | 1477 | 0.60 | Mamaní et al. (2019) |
| Persian ironwood | Pyrolysis | 500 | – | $H_3PO_4$ | 500 | 2 | 1802 | 0.83 | Nowrouzi et al. (2018) |
| Corn husk | Pyrolysis | – | – | KOH | 800 | 1 | 928 | 0.53 | Song et al. (2015) |
| Silk | Pyrolysis | – | – | $ZnCl_2$ | 900 | 1 | 2494 | 2.28 | Hou et al. (2015b) |
| Sugar cane bagasse | Pyrolysis | – | – | $CaCl_2$ | 800 | 2 | 946 | 1.39 | Liu et al. (2016) |
| Spent coffee ground | Pyrolysis | – | – | $K_2CO_3$ | 800 | 5 | 2337 | 1.15 | Kim et al. (2020) |
| *Artemia cyst* shell | Pyrolysis | 700 | 4 | KOH | 700 | 1 | 1758 | 0.76 | Zhao et al. (2015) |
| Watermelon peel | Pyrolysis | 800 | 3 | $KHCO_3$ | 800 | 3 | 2360 | 1.31 | Zhao et al. (2017) |
| Peanut shell | HTC | 180 | 48 | KOH | 800 | 1 | 2396 | 1.31 | Ding et al. (2015) |
| Silkworm cocoon | Pyrolysis | 450 | 0.5 | KOH | 900 | 2 | 3386 | 2.20 | Sun et al. (2018a) |
| Barley | Pyrolysis | – | – | $Cu_3(C_6H_5O_7)_2$ | 800 | 2 | 2140 | 1.16 | Wan et al. (2020a) |
| Rice husk | Pyrolysis | 600 | 1 | NaOH | 750 | 1 | 1789 | 1.15 | Chen et al. (2020) |
| *Leucaena leucocephala* | Pyrolysis | 400 | 1 | KOH | 800 | 2 | 1901 | 1.09 | Hou et al. (2015a) |
| Rice husk | Pyrolysis | 500 | 1 | KOH | 700 | 1 | 2804 | 1.80 | Liu et al. (2015) |
| Mixed crab shell and rice husk | HTC | 200 | 3 | KOH | 700 | 3 | 3557 | 2.02 | Peng et al. (2019) |
| Poplar catkins | Pyrolysis | 400 | 3 | $ZnCl_2$ | 800 | 2 | 1455 | 0.68 | Chang et al. (2019a) |

(4) Even after thorough washing, activated biochar may still contain residual chemicals, potentially affecting its appropriateness for certain applications.

### 3.5 Metal impregnation

In recent times, the incorporation of metal elements such as iron (Fe), cobalt (Co), nickel (Ni), manganese (Mn), or copper (Cu), among others, into the biochar matrix has become a notably effective approach for modifying its surface characteristics (Yang et al. 2022a). Pristine biochar can be modified by loading it with various metals or metal oxides through hydrothermal and co-precipitation methods using metal salts, oxides, or hydroxides. For instance, in a study conducted by Lin et al. (2019), biochar underwent impregnation with solutions of $KMnO_4$ and $Fe(NO_3)_3$, as well as $KMnO_4$ and $FeSO_4$. Subsequently, it underwent pyrolysis to synthesize Fe, Mn-modified biochar. The SSA of the resulting biochar varied significantly depending on the oxidation state of the Fe. Biochar impregnated with $Fe^{3+}$ exhibited a much larger SSA (208 $m^2\ g^{-1}$) compared to $Fe^{2+}$ (7.53 $m^2\ g^{-1}$) and the raw biochar (60.97 $m^2\ g^{-1}$). Additionally, $Fe^{3+}$ could form iron oxide on the biochar surface, demonstrating strong oxidation properties.

The metal impregnation approach involves blending carbon feedstock with metal precursors to create active sites within the biochar matrix, thus integrating active metallic components. In general, the fabrication of metal-impregnated biochar can be achieved using two approaches: (i) Immersing the biomass feedstock in a solution containing metal oxide salts before the pyrolysis process, as a pre-pyrolysis treatment; (ii) Submerging the biochar material in a solution containing metal ions after pyrolysis has occurred, as a post-pyrolysis treatment (Sizmur et al. 2017). Treating the carbon source with metal precursors such as manganese chloride ($MnCl_2$), magnesium chloride ($MgCl_2$), zinc chloride ($ZnCl_2$), and potassium permanganate ($KMnO_4$) results in the formation of their respective oxides on the biochar surface, as demonstrated by Tan et al. (2016). For example, pyrolysis of biomass pre-treated with $MgCl_2$ leads to the fabrication of porous MgO-biochar nanocomposites, which exhibit excellent adsorption efficiency (Zhang et al. 2012). In another investigation,

Kazemi Shariat Panahi et al. (2020) described various biochar modification techniques aimed at improving its ability to adsorb various inorganic pollutants, including metal cations (like $Cd^{2+}$, $Pb^{2+}$, $Zn^{2+}$, $Cu^{2+}$, $Hg^{2+}$) and oxy-anions (like $AsO_4^{3-}$, $PO_4^{3-}$), from water. Their findings indicated that the incorporation of iron or manganese oxides into the biochar structure significantly enhanced its oxy-anion adsorption capacity. This enhancement was attributed to the creation of entirely new active sites and functional groups on the biochar surface that were not present before.

Introducing metals into a biochar matrix not only improves its common surface properties such as SSA, pore structure, and surface functional groups but also boosts its electrical conductivity and redox potential due to the distinctive qualities of these metals. Consequently, this impregnation procedure leads to the development of versatile functional biochar materials that can be applied in diverse practical scenarios (Qin et al. 2020). To facilitate the ORR within a fuel cell, an effective electrocatalyst must possess specific characteristics, including a substantial SSA, a porous structure with a desired pore size distribution, adequate electrical conductivity, and mechanical strength to facilitate efficient mass transfer during the ORR process. N-doped porous carbon, when used alone, cannot meet all these criteria. Therefore, it is preferred to incorporate N sources in combination with metal dopants (e.g. Fe, Cu, Ni, Mn, Co, Ag, etc.) to produce metal-N-doped porous carbon materials, which function as efficient electrocatalysts for the ORR (Kaur et al. 2019). Numerous studies have indicated that the inclusion of metal elements into the biochar matrix through doping can greatly enhance the catalytic properties of biochar-based materials. For instance, Ohms et al. (1992) fabricated carbon-supported electrocatalysts for the ORR by using PAN as the nitrogen source, along with metal precursors such as metal sulfates ($MSO_4$, where M=Fe, Co, Ni, Mn, Cu) and zinc chloride ($ZnCl_2$). It was observed that under identical experimental conditions, different metals yielded varying levels of ORR catalytic activity. In an acidic environment, Co, Fe, and Mn demonstrated improved ORR performance, in that order. Both the Co and Fe-doped electrocatalysts exhibited comparable performance in an alkaline environment.

### 3.5.1 Limitations of metal impregnation

The metal impregnation technique, which involves the incorporation of metal nanoparticles onto the biochar surface, is used to improve its functional properties for various applications. Nevertheless, this approach has its own set of limitations:

(1) Depending on the specific application and conditions, there is a risk of metal leaching over time, which can have negative environmental impacts and reduce the long-term stability and effectiveness of the biochar material.

(2) Achieving a uniform dispersion of metal nanoparticles within the biochar matrix can be challenging. Agglomeration of metal particles can lead to variations in reactivity and performance.

(3) Metal doping can alter the porous structure of biochar. For example, the formation of metal oxides on the biochar surface may block or modify pore openings, affecting the accessibility of active sites within the biochar. This can impact the SSA available for adsorption or catalysis.

(4) The cost associated with impregnating the metal precursors can be significant, particularly for precious metals, making the process uneconomical for certain applications.

### 3.6 Heteroatom doping

The performance of carbon materials is significantly influenced by their porous structure as well as their surface functional groups. The structure of carbon materials can be tuned through suitable activation processes, leading to the development of various pore structures, including micro, meso, and macropores. Another approach to enhancing their performance is surface functionalization. The most prevalent technique for surface functionalization is heteroatom doping, which involves introducing elements like nitrogen (N), oxygen (O), sulfur (S), phosphorus (P), and boron (B) onto the carbon surface to enhance its functional properties (Yang et al. 2023b). Figure 12a illustrates the doping process of different heteroatoms in the carbon matrix. Doping is typically carried out through two methods: self-doping and external doping. Self-doping involves the direct carbonization of biomass precursors that already contain abundant heteroatoms, examples of which include medulla tetrapanacis, soybean, cattail wool, and houttuynia. On the other hand, external doping entails treating pristine biochar with external precursors like ammonia, urea, melamine, aniline, thiourea, boric acid, nitric acid, phosphoric acid, and so forth after the carbonization process. The steps involved in external doping, including pre-carbonization, activation, and heteroatom doping, are complex, costly, and require significant energy input (Yang et al. 2023b).

### 3.6.1 N-doping

Nitrogen (N) is the predominant heteroatom utilized for doping in the fabrication of functional biochar-based materials. Various biomass sources, including enoki
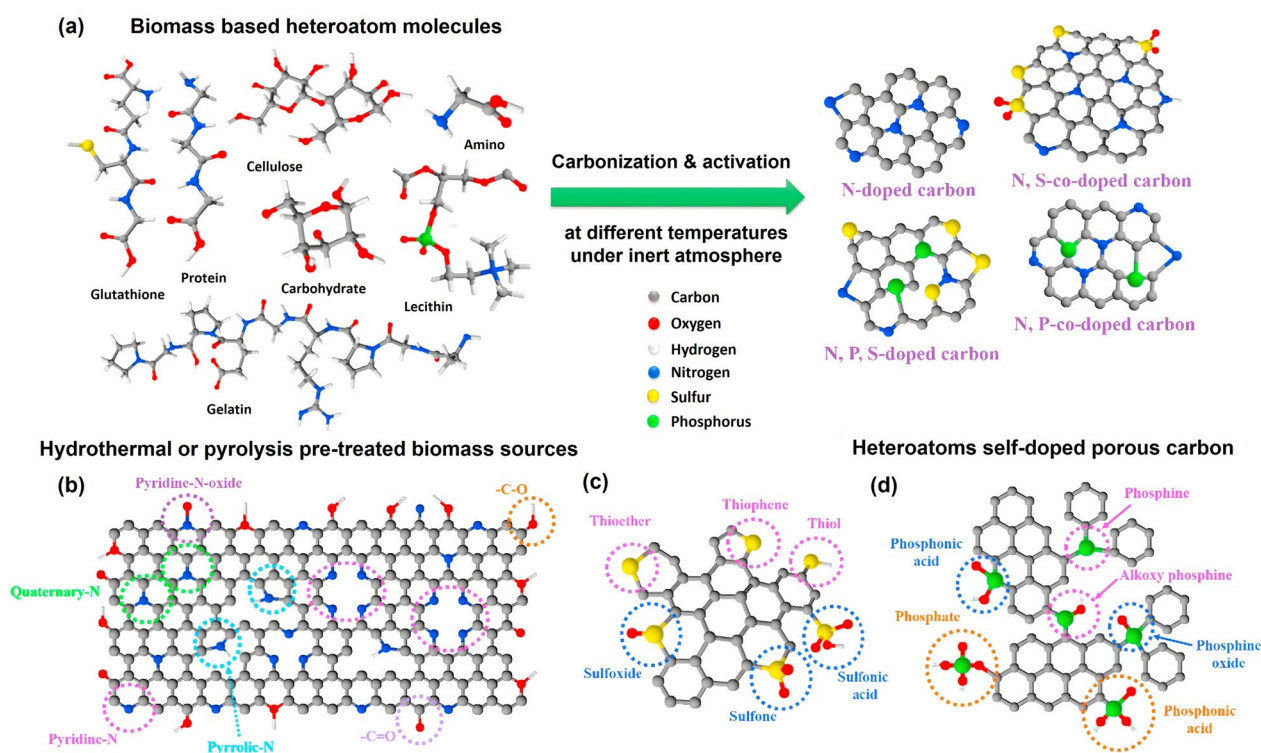
**Fig. 12** Interactions of heteroatoms during the doping process in the fabrication of (**a**) N, P, S-doped, **b** N-doped, **c** S-doped, and **d** P-doped porous bio-carbons (Gopalakrishnan and Badhulika 2020), Copyright © 2020, Elsevier

mushrooms, palm residue, soybean dregs, chitosan, peanut shells, food waste, chicken feathers, and tobacco stems, inherently possess substantial N content (Yang et al. 2023b). Through a thermochemical conversion process, these biomass sources can be transformed into functional carbon materials with N atoms inherited from the original biomass. Conversely, N-rich additives such as urea, ammonia, ammonium salts, melamine, and aniline can be employed to manufacture enriched N-doped carbon materials. The introduction of N atoms into the $sp^2$ carbon matrix results in the formation of four different bonding states: pyridine-N, pyrrolic-N, graphitic-N, and oxidized pyridine-N (Gopalakrishnan and Badhulika 2020), as depicted in Fig. 12b. Biomass-derived carbon materials contain multiple O-containing functional groups, and these, in combination with N, play an important role in Faradaic reactions. Therefore, the incorporation of N into the biochar matrix brings about changes in its structural symmetry and produces more active sites, which are beneficial for enhancing electrochemical performance and contributing to redox reactions.

The effectiveness of N-doping in biochar matrix can be attributed to several factors: (i) N is the neighboring element to carbon, and this proximity allows for the adjustment of the number of electrons as a result of doping; (ii) N acts as an electron donor, providing more electrons to the interconnected carbon network. This, in turn, enhances electronic conductivity; (iii) N possesses an atomic radius similar to that of carbon, which reduces lattice mismatching and promotes structural compatibility; (iv) The configuration of the C-N bond behaves like n-type materials, making it suitable for a wide range of applications (Gopalakrishnan and Badhulika 2020). For instance, Chang et al. (2019b) fabricated an N-doped hierarchical porous carbon material derived from Firmiana simplex biomass. This carbon material exhibited substantial microporosity (86.8%) and had small mesopores ranging from 2 to 4 nm. The resulting carbon material had a notably high SSA of 2351 $m^2$ $g^{-1}$ and exhibited minimal internal resistance for efficient charge transfer. When employed as an electrode material, this porous carbon achieved an outstanding specific capacitance of 836 F $g^{-1}$ at a current density of 0.2 A $g^{-1}$ in a 2 M $H_2SO_4$ solution.

### 3.6.2 S-doping

Sulfur (S), belonging to the oxygen (O) group family, exhibits similar functional groups to O, such as thiols, thioethers, and sulfoxides, when it binds with carbon, just as O forms bonds with carbon through functional

groups like alcohols, ethers, and peroxides. It possesses a greater atomic radius compared to carbon, and this leads to the creation of defects within the biochar structure, which then act as active sites for redox reactions (Wan et al. 2020b). The introduction of S atoms into the sp$^2$ carbon leads to the creation of a bandgap, the incorporation of localized states, and the formation of diverse S-containing groups, including thiol, thioether, thiophene, sulfoxide, sulfone, and sulfonic acid (Yang et al. 2023b), as depicted in Fig. 12c. For instance, Demir et al. (2018) successfully fabricated S-doped micro/mesoporous carbon from lignin, a biomass source, using an in situ carbonization-activation strategy. The resulting carbon material contained up to 3.2 wt.% of S, as confirmed by XPS, and possessed a substantial SSA of 660 m$^2$ g$^{-1}$, featuring numerous micropores and mesopores in the structure. When this S-doped micro/mesoporous carbon was used as the electrode material in supercapacitors, it exhibited a noteworthy specific capacitance of 225 F g$^{-1}$ at a current density of 0.5 A g$^{-1}$. Furthermore, it showcased exceptional performance when employed as an electrocatalyst for the ORR in a 0.1 M KOH electrolyte.

### 3.6.3 P-doping

Phosphorus (P), categorized as an n-dopant element and belonging to the nitrogen (N) group family, shares similar doping characteristics with N (which has a smaller atomic radius of 0.070 nm) and S (with an atomic radius of 0.104 nm). However, due to its larger atomic radius of 0.110 nm, P-doping results in an expanded interlayer spacing, which leads to the creation of electrochemically active sites (Soltani et al. 2021). When it comes to P-doping, H$_3$PO$_4$ is the primary activator preferred. The incorporation of P into the biochar matrix leads to the introduction of a substantial quantity of P–O functional groups, which, in turn, improves the electrochemical characteristics of the biochar (Yang et al. 2023b). The process of incorporating P into the biochar matrix initially introduces unstable reduced states. Over time, these states undergo gradual oxidation due to exposure to oxygen groups, resulting in the formation of various oxidized P-containing functional groups. These groups include phosphine, alkoxy phosphine, phosphine oxide, phosphate, and phosphonic acid (Gopalakrishnan and Badhulika 2020), as depicted in Fig. 12d. P-doping in a biochar matrix exhibits greater electron-donating capabilities and displays stronger n-type behavior compared to N-doping. Thus, P-doping promotes charge delocalization and asymmetric spin density, resulting in enhanced electrochemical characteristics of the biochar materials.

### 3.6.4 Multi-heteroatoms doping

Apart from single heteroatom doping with N, S, P, or B, certain researchers have delved into co-doping carbon precursors with two or more distinct heteroatoms to enhance their catalytic performance. Their findings suggest that introducing multiple heteroatoms simultaneously into the carbon matrix results in increased catalytic activity compared to carbon materials doped with just one heteroatom (Yang et al. 2023b). For example, Dong et al. (2021) prepared N, P-doped mesoporous carbon material assisted by a SiO$_2$ template for use in water splitting and supercapacitor applications. The resulting carbon material exhibited a mesoporous structure and had a SSA of 593 m$^2$ g$^{-1}$. The significant presence of N and P in this synthesized carbon material facilitated electron transfer, leading to a substantial improvement in its electrocatalytic performance for the HER and its specific capacitance for supercapacitors. When employed as the electrode material in supercapacitors, this SiO$_2$ template-assisted N, P-doped mesoporous carbon displayed a notably high specific capacitance of 219 F g$^{-1}$ at 1 A g$^{-1}$. Additionally, as an electrocatalyst for the HER, it demonstrated excellent electrocatalytic performance with a small Tafel slope of 52 mV dec$^{-1}$ and a low overpotential of 298 mV at 10 mA cm$^{-2}$. In another investigation, Gasim et al. (2023) fabricated N, S, B-tri-doped biochar from sawdust biomass using a single-step calcination technique for its application as a peroxymonosulfate (PMS) activator for tetracycline (TC) removal. To introduce these three different heteroatoms (N, S, and B) into the biochar matrix, boric acid and thiourea were employed as precursors.

### 3.6.5 Limitations of heteroatom doping

Heteroatom doping, which involves introducing elements like N, O, S, B, or P onto the biochar surface, is a common method for creating functionalized biochar materials. While this method offers numerous benefits, it also has certain limitations:

(1) The effectiveness of heteroatom doping can significantly rely on the choice of precursor material and the specific conditions employed during the doping process.
(2) Achieving a high level of doping efficiency and uniform distribution of heteroatoms across the biochar surface can be challenging.
(3) The effectiveness of heteroatom doping may be specific to certain applications.
(4) The stability and durability of the introduced heteroatoms can fluctuate depending on the biochar environment.

### 3.7 Plasma activation

Plasma activation serves as an effective technique for altering the surface properties of biochar materials, enabling the creation of functional variants. Within the plasma modification process, the generation of high-energy electrons and active radicals facilitates the introduction of heteroatoms and the corresponding active sites into the porous carbon structure (Saleem et al. 2023). In particular, the plasma modification technique is eco-friendly as it eliminates the need for toxic chemical reagents when compared to chemical activation processes. It is important to highlight that plasma modification has the potential to augment the presence of N-containing or O-containing functional groups within biochar materials (Zhou et al. 2022a). Non-thermal plasma modification is highly suitable for large-scale industrial production of functionalized biochar materials due to its environmentally friendly nature. It has demonstrated its reliability in enhancing surface properties while preserving the overall physicochemical characteristics of biochar materials. The presence of free electrons, energetic ions, and active radicals during plasma treatment leads to the surface modification of biochar. For instance, in cold oxygen plasma, active oxygen radicals may be generated, which can interact with the $sp^2$ hybridized C=C bonds, thereby introducing defects in the biochar matrix (Kandel et al. 2022). Figure 13a illustrates the functionalization of pristine biochar through plasma treatment employing different activating agents, including air, $O_2$, $N_2$, Ar, $H_2$, $HF_6$, and $NH_3$. Wu et al. (2021) conducted non-thermal plasma activation using $N_2$ to introduce N-doping into porous

carbon derived from lilac and lotus seedpods. This was done to enhance the performance of the biomass-derived carbon material when used as an electrode in supercapacitors. $N_2$ is both non-toxic and highly cost-effective, with easy and inexpensive production. Importantly, the $N_2$ plasma activation process does not result in any emissions of pollutants. After $N_2$ plasma activation, there was a significant increase in the N-containing functional groups within the resulting porous carbons. As a result, the specific capacitances of the porous carbon electrodes exhibited substantial improvements, reaching 343 F $g^{-1}$ (a 60% increase) for lilac-derived carbon and 332 F $g^{-1}$ (a 65% increase) for lotus seedpod-derived carbon. In another study conducted by Hu et al. (2020), a total of 12 raw biochars were subjected to Ar/$NH_3$ plasma activation to incorporate amino groups onto their surfaces. The illustration of Ar/$NH_3$ plasma activation is depicted in Fig. 13b. To enhance the effectiveness of surface amination, these biochars were first subjected to ball milling before undergoing plasma treatment. In Fig. 13c, it can be observed that the N content on the surfaces of plasma-treated ball-milled biochars (referred to as PBMBs) falls within the range of 3.6% to 6.8%, which is notably higher compared to that of milled biochars. The quantity of amino groups on these PBMBs falls within the range of approximately $3.22 \times 10^{16}$ to $4.84 \times 10^{16}$ per mg of biochar. Additionally, these biochars, which have undergone both plasma treatment and ball milling, exhibit a considerable increase in SSA compared to untreated raw biochars (Fig. 13d).
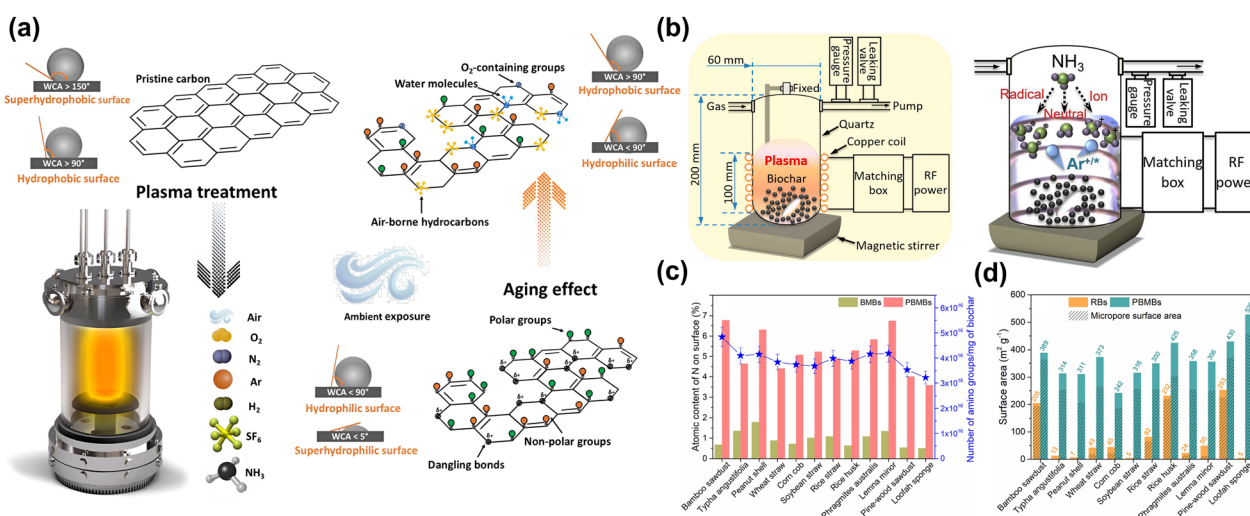


**Fig. 13 a** Schematic depiction of plasma activation of pristine biochar (Ortiz-Ortega et al. 2021), Copyright © 2021, Elsevier. **b** Representation of radio-frequency (RF) Ar/$NH_3$ plasma activation; **c** Quantification of N content and –$NH_2$ groups; **d** Surface area characteristics of engineered biochars (Hu et al. 2020), Copyright© 2020, Elsevier

### 3.7.1 Limitations of plasma activation

Plasma activation of biochar is a relatively novel and promising technique that involves using plasma to modify the physicochemical and structural properties of pristine biochar for various applications. However, like any technology, it has its limitations. Some of the key limitations of plasma activation of biochar include:

(1) Plasma activation of biochar requires a significant amount of energy, which can make the activation process expensive and less environmentally friendly if the energy source is not renewable.

(2) The mechanisms underlying plasma activation of biochar are not fully understood, which can hinder the optimization of the activation process for specific applications

(3) The quality and physicochemical characteristics of functionalized biochar produced through plasma activation can vary depending on the biomass feedstock used, making it challenging to achieve consistent results.

(4) Depending on the biomass precursor and process conditions, plasma activation may generate undesirable byproducts.

## 3.8 Electrospraying

Electrospraying represents an innovative approach to producing high-quality functional carbon materials from biomass resources. The engineered carbon structures, which not only exhibit enhanced electrical conductivity but also offer additional benefits such as 3D interconnected networks, improved ion diffusion, and enhanced charge transfer, play a pivotal role in significantly boosting the electrochemical performance of biochar-based materials (Cao et al. 2021b). This technique involves electrospraying a suspension containing biochar particles and a binding agent, followed by a carbonization process. Electrospraying is an electrohydrodynamic process in which a mixture of biochar and binding agent can be atomized using a high DC voltage, resulting in particle formation (Guo et al. 2022). A typical electrospraying setup consists of four main components: a high-voltage supply, a metallic needle, a syringe pump, and an electrically grounded collector. For instance, Guo et al. (2023) employed an electrospray-carbonization approach to produce $SiO_x$/Fe–N-C composites, utilizing rice husks as the biomass feedstock. The synthesis process of fabricating $SiO_x$/Fe–N–C is depicted in Fig. 14a. The process commenced with the cleaning and acid treatment of rice husks, followed by calcination to yield $SiO_2$ powder. This powder consisted primarily of a biomass framework and $SiO_2$ nanoparticles. Subsequently, a precursor solution, comprising polyacrylonitrile (PAN), $SiO_2$ nanoparticles,

and $Fe(acac)_3$, was employed to fabricate $SiO_x$/Fe–N–C microspheres via the electrospray-carbonization process. The SEM image in Fig. 14b shows that the $SiO_x$/Fe–N–C composites have an irregular spherical shape. Figure 14c illustrates the TEM analysis of the $SiO_x$/Fe–N–C microspheres. EDS elemental mapping confirmed the presence of elements such as Fe, Si, O, C, and N in the $SiO_x$/Fe–N–C composites (Fig. 14d). Furthermore, Fig. 14e depicts the identification of individual Fe atoms (highlighted in yellow circles) and a limited number of atomic clusters (indicated by red circles) within the $SiO_x$/Fe–N–C product.

Cao et al. (2021b) integrated electrospraying and carbonization techniques to fabricate multi-layered carbon structures resembling honeycombs, referred to as HMC, using wood-derived lignin biomass, as depicted in Fig. 14f. They accomplished this by blending polymethyl methacrylate (PMMA) with lignin, resulting in the formation of lignin/PMMA microspheres through electrospraying. Subsequently, they directly carbonized these microstructures to synthesize the HMC. The microstructural features and pore size of the resulting carbon materials could be adjusted by varying the applied voltage during the electrospraying process. In this method, PMMA served a dual purpose: it improved the ability to spray lignin and acted as a template for creating intricate 3D interconnected carbon structures. The resulting carbon material displayed fascinating characteristics, featuring a hierarchical porous structure comprising micropores, mesopores, and macropores. Furthermore, its specific capacitance as an electrode material in supercapacitors surpassed that of the majority of lignin-based carbon materials reported in previous studies. This simple and efficient method is in harmony with environmental standards, paving the way for the advancement of eco-friendly energy storage devices.

### 3.8.1 Limitations of electrospraying method

The electrospray-carbonization is a relatively new technique for the synthesis of functional carbon materials, which involves electrospraying a suspension containing carbon precursor and a binding agent to form micro or nanoscale droplets, followed by carbonization to generate biocarbon with enhanced electrical conductivity and specific functional characteristics. While this process offers several advantages, it also has its limitations:

(1) Specialized equipment, such as electrospray devices and carbonization facilities, is necessary for the electrospray-carbonization process. The setup and maintenance of this equipment can be both costly and complex.
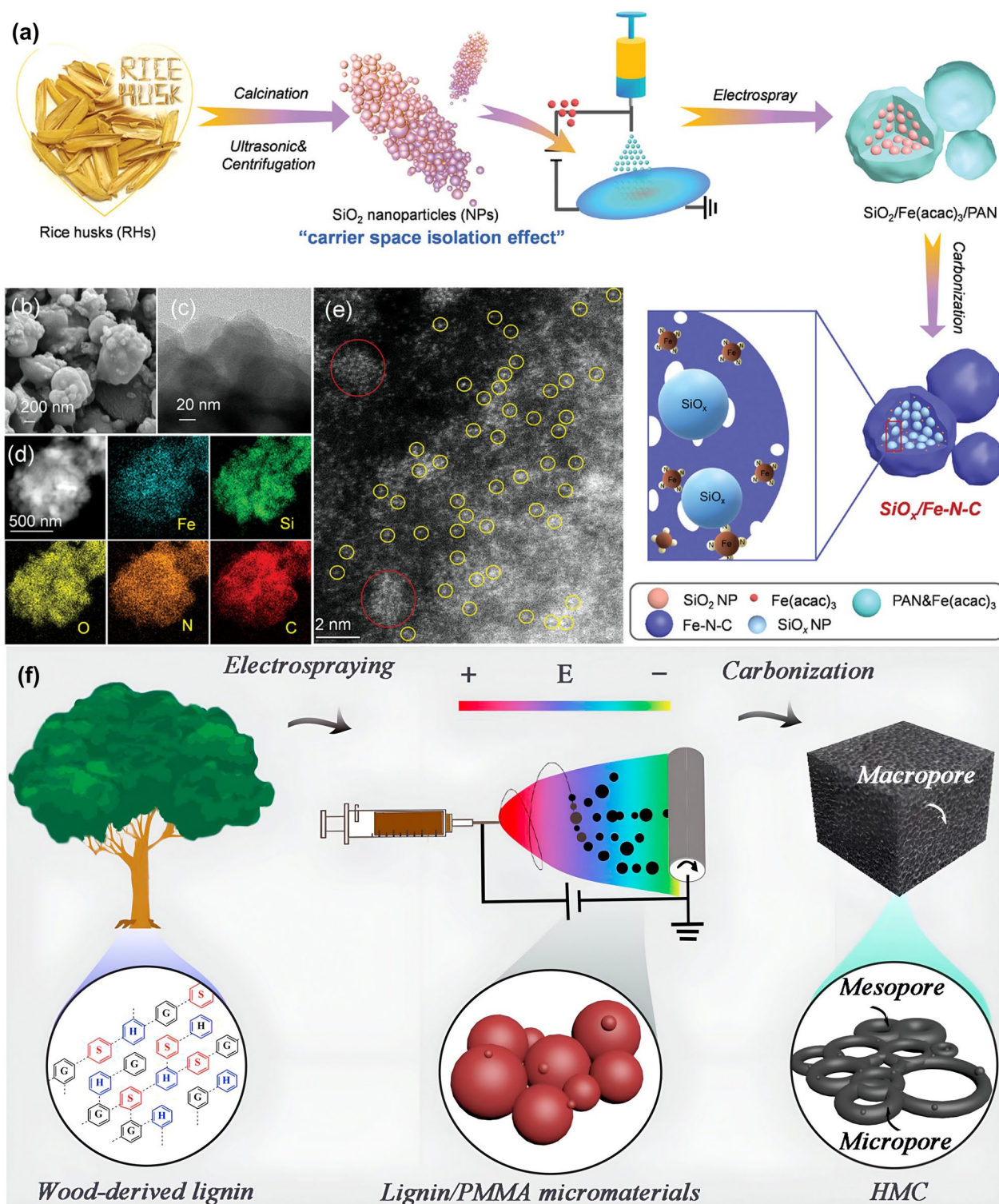
**Fig. 14 a** Schematic representation of SiO$_x$/Fe−N−C synthesis via electrospray-carbonization method; **b** SEM, **c** TEM, **d** EDS, and **e** AC-HAADF-STEM images of SiO$_x$/Fe−N−C (Guo et al. 2023), Copyright © 2023, The Authors, John Wiley & Sons. **f** Fabrication of HMC from wood-derived lignin through electrospray-carbonization method (Cao et al. 2021b), Copyright© 2021, Elsevier

(2) The selection of biomass precursor is critical for this process. Not all precursor materials may be suitable for electrospray-carbonization, limiting the versatility of the technique.

(3) Electrospray is often a slow process, which can restrict the production rate of functionalized biochar materials compared to alternative synthesis methods.

(4) The cost associated with producing functionalized biochar using the electrospray-carbonization process may be higher compared to other methods, primarily due to the specialized equipment and energy requirements.

(5) The electrospray-carbonization process is a relatively new technique, and there may still be aspects of the process that are not fully understood or optimized.

In summary, biochar functionalization techniques offer versatile tools to tailor the pore structure and surface chemical properties of biochar, making it suitable for diverse energy and environmental applications. Techniques such as ball milling, templating, molten salt activation, and chemical activation excel at significantly enhancing porosity and surface area, resulting in biochar with exceptional capacity for adsorption and interaction. On the other hand, techniques like metal impregnation, heteroatom doping, and plasma treatment focus on modifying surface functional groups and chemical reactivity, potentially unlocking catalytic abilities. Choosing the right modification hinges on the desired properties for the intended application. For example, high surface area and microporosity are vital for adsorption, while specific functional groups might be key for catalysis. Excitingly, combining multiple modifications allows us to reap the benefits of both, maximizing both surface area and functionality. Table 6 provides a concise overview of various biochar functionalization techniques, highlighting their impact on these crucial aspects.

## 4 Characterization of functionalized biochar

Functionalization plays a crucial role in modifying the physical, chemical, and structural characteristics of biochar, enhancing its efficacy for diverse applications such as catalysis, adsorption, charge storage, and soil amendment. The characterization of functionalized biochar is essential for understanding its properties and forecasting its performance in diverse energy and environmental contexts. Various techniques are available for characterizing functionalized biochar, each offering distinct insights into its physical, chemical, and surface features. Table 7 summarizes the key properties of functionalized biochar along with advanced characterization techniques to evaluate them.

### 4.1 Pore structure

Functionalized biochar possesses a highly porous structure featuring a complex network of micropores, mesopores, and macropores. Activation of biochar with alkalis or acids creates more pores and channels, making it a more effective adsorbent for pollutants and a better catalyst for energy conversion reactions. Scanning electron microscopy (SEM) is a valuable tool for obtaining high-resolution images of the surface morphology of functionalized biochar materials. It allows for the visualization of pores, cracks, and other features on the biochar surface, providing insights into its physical structure. In addition to SEM, transmission electron microscopy (TEM) is an advanced imaging technique that plays a crucial role in examining the internal structure of functionalized biochar materials at nanoscale resolutions. For instance, Huang et al. (2023b) performed SEM-TEM analysis to examine the surface morphologies and internal structures of two composite materials: one consisting of nano zero-valent iron (nZVI) loaded onto undoped biochar ($BC_{900}$), referred to as nZVI@$BC_{900}$, and the other comprising nano zero-valent iron (nZVI) loaded onto phosphorus-doped biochar ($P_1$-$BC_{900}$), denoted as nZVI@$P_1$-$BC_{900}$. Regarding nZVI@$BC_{900}$, the nZVI particles exhibited a spherical morphology with diameters ranging from ~ 400 to 600 nm, and the distribution of these particles appeared to be irregular, as shown in Fig. 15a. High-resolution transmission electron microscopy (HR-TEM) images, displayed in Fig. 15b, provided additional evidence of the presence of nZVI spherical particles on the $BC_{900}$ substrate, highlighting the presence of a discernible oxide shell with a thickness ranging from 10 to 18 nm. In contrast, for nZVI@$P_1$-$BC_{900}$, the nZVI spheres exhibited smaller particle sizes, with diameters ranging from 70 to 200 nm, and these particles were found to be more uniformly distributed on the $P_1$-$BC_{900}$ substrate (Fig. 15c). Additionally, the HR-TEM images of nZVI@$P_1$-$BC_{900}$ provided further confirmation of the presence of nano-cracks within the nZVI nanosphere, without any noticeable oxide layer (Fig. 15d–f).

Zhang et al. (2021) conducted SEM-TEM analysis to assess the external morphologies and internal structures of hierarchically porous carbon materials derived from Ulmus pumila (UP) biomass, which were activated using potassium bicarbonate ($KHCO_3$). These materials were labeled as HPC-UP-2, HPC-UP-4, HPC-UP-6, and HPC-UP-8. When examining the mass ratio of $KHCO_3$ to UP, represented as "x," at a value of 2, HPC-UP-2 exhibited a limited amount of pore structure, and distinct blocks

**Table 6** Comparison of biochar functionalization techniques

| Technique | Description | Pros | Cons |
|---|---|---|---|
| Ball milling | Mechanical grinding using balls to break down large particles, increasing surface area and pore volume | • Simple and cost-effective<br>• Effective for increasing surface area and porosity<br>• Uniform particle size | • Limited control over functional groups<br>• Possibility of contamination from milling media<br>• Lack of control over particle morphology |
| Templating | Using hard or soft templates to create specific pore structures | • Highly tunable pore size and distribution<br>• Tailored porosity and surface area<br>• Controlled morphology leading to improved performance | • Complex and often multi-step process<br>• May not allow for fine-tuning of surface chemistry<br>• Template removal can be challenging |
| Molten salt activation | High-temperature treatment with molten salts (e.g., KCl, NaCl) to increase surface area and porosity | • Highly effective in creating microporosity<br>• Tailorable surface chemistry with different salts<br>• Effective for non-porous precursors | • Energy-intensive<br>• Corrosive salts require special handling<br>• Recycling of salts can be challenging |
| Chemical activation | Treatment with acids (e.g., $H_2SO_4$, $H_3PO_4$), alkalis (e.g., KOH, NaOH), or oxidizing agents (e.g., $H_2O_2$) to develop pores and surface functional groups | • Highly effective for increasing surface area and porosity<br>• Tunable surface chemistry<br>• Introduces specific functionalities like amine or carboxyl groups | • Corrosive chemicals require caution<br>• May contain residual chemicals<br>• Can generate hazardous byproducts |
| Metal impregnation | Loading metal nanoparticles (e.g., Fe, Co, Ni, Cu, Mn) onto biochar surface to enhance catalytic activity and surface functionality | • Introduces specific catalytic sites<br>• Creates new adsorption sites for specific pollutants<br>• Enhances redox properties | • Uniform dispersion of metal nanoparticles can be challenging<br>• Potential for metal leaching and toxicity<br>• May be expensive for certain metals, especially precious metals |
| Heteroatom doping | Introducing heteroatoms (e.g., N, S, P, B) into the biochar structure to improve conductivity, catalytic activity, and adsorption capacity | • Improves catalytic activity<br>• Enhances adsorption capacity and selectivity for specific pollutants<br>• Improves electron transfer | • Controlled doping can be challenging<br>• May affect the durability and stability of biochar<br>• Potential for leaching of dopants |
| Plasma treatment | Exposing biochar to high-energy plasma (such as $N_2$, Ar, or $NH_3$) to modify surface chemistry | • Introduces diverse functional groups<br>• Increases surface area and porosity<br>• Improves wettability and reactivity | • High energy consumption<br>• Plasma treatment parameters need careful control<br>• Potential for surface damage |
| Electrospraying | Application of high-voltage electric field to boost electrical conductivity and charge transfer capabilities of biochar | • Controlled particle size and morphology<br>• Increases electrical conductivity<br>• Improves ion diffusion | • Requires specialized equipment and expertise<br>• Energy-intensive<br>• Can be time-consuming |

**Table 7** Key properties of functionalized biochar materials and corresponding characterization techniques

| Properties | Characterization techniques |
| --- | --- |
| Pore structure | Scanning electron microscopy (SEM), Transmission electron microscopy (TEM) |
| Elemental composition | CHNS elemental analysis, Energy-dispersive X-ray spectroscopy (EDS), X-ray photoelectron spectroscopy (XPS) |
| Surface functional groups | Fourier-transform infrared spectroscopy (FTIR) |
| Crystallinity and phase composition | X-ray diffraction (XRD) |
| Thermal stability | Thermogravimetric analysis (TGA) |
| Surface area and porosity | Brunauer–Emmett–Teller (BET) analysis |
| Graphitization degree and aromaticity | Raman spectroscopy |
| Electrical conductivity | Four-point probe method, Electrochemical impedance spectroscopy (EIS) |

were still visible, as depicted in Fig. 15h. As the value of x gradually increased, the blocks transformed into pores, resulting in an overall enhancement of porosity within the carbon structure (Fig. 15i–k). However, upon reaching x = 8, there was no noticeable alteration in the porosity and structure of HPC-UP-8 compared to HPC-UP-6, indicating that the activation effect of $KHCO_3$ ceased to have a significant impact once x reached a value of 6. The microstructure of HPC-UP-6 was further analyzed through TEM, revealing a hierarchical porous configuration that includes macro-, meso-, and micropores (Fig. 15l–o).

### 4.2 Elemental composition

Biochar is predominantly composed of carbon (C), yet it incorporates various other elements, including hydrogen (H), oxygen (O), and nitrogen (N), along with additives and minerals like calcium (Ca), potassium (K), phosphorus (P), and sulfur (S). The proportions of these elements are crucial in determining the properties and potential applications of functionalized biochar materials. Advanced characterization techniques, such as CHNS elemental analysis, energy-dispersive X-ray spectroscopy (EDS), and X-ray photoelectron spectroscopy (XPS), are employed to measure the elemental composition of functionalized biochar.

Carbon content is typically assessed using CHNS elemental analyzers, which quantify the amounts of carbon (C), hydrogen (H), nitrogen (N), and sulfur (S) in a biochar sample. EDS, often used in conjunction with SEM or TEM, provides valuable insights into the elemental composition of engineered biochar materials, helping understand the distribution of various elements within the material (Fig. 15g, p–s). XPS is another valuable surface analysis technique used to examine the elemental composition and chemical states of elements present on the surface of functionalized biochar materials. Regarding elemental composition, XPS facilitates the identification and quantification of elements on the biochar surface, including carbon (C), oxygen (O), nitrogen (N), as well as any potential elements that might be present as additives or impurities. It is also capable of discerning between distinct chemical states of elements present on the biochar's surface, including various forms of carbon (like $sp^2$=C, $sp^3$–C, C–O, C=O, O=C–O), diverse oxygen states (such as –OH, C=O, –COOH), and different nitrogen configurations (e.g., N–O, N–Q, N–5, N–6, –$NH_2$, etc.) (Hamid et al. 2022).

In XPS, the C 1s, O 1s, and N 1s spectra are crucial spectral regions employed for the assessment of the surface chemistry of engineered biochar materials. These spectra correspond to the binding energies of electrons emitted from carbon (C), oxygen (O), and nitrogen (N) elements located on the biochar surface upon excitation by X-rays. The C 1s spectrum offers insights into diverse chemical states of carbon atoms, encompassing $sp^2$=C (graphitic carbon), $sp^3$–C (aliphatic carbon), as well as various other configurations, including C–O, C=O, and O=C–O. The O 1s spectrum furnishes details regarding the oxygen's chemical states, which encompass the identification of various O-containing functional groups such as hydroxyl (–OH), carbonyl (C=O), and carboxyl (–COOH). The N 1s spectrum furnishes insights into the nitrogen's chemical states, allowing the identification of diverse N-containing functional groups such as amino (–$NH_2$), amine oxide (N–O), and nitrile (C≡N) present on the engineered biochar surface (Egyir et al. 2022).

Numerous research studies have delved into the utilization of XPS to evaluate the surface chemistry of engineered biochar materials. For example, Li et al. (2022a) employed XPS to analyze biochars derived from different crop straws, examining their elemental composition and chemical states. Among all the tested biochars, RI-HBCK displayed the highest surface content of O (30.9 wt.%) and N (0.8 wt.%), which can be attributed to the activation process involving potassium bicarbonate ($KHCO_3$), as depicted in Fig. 16a. The C 1s spectrum of RI-HBCK was deconvoluted into five distinct states, representing
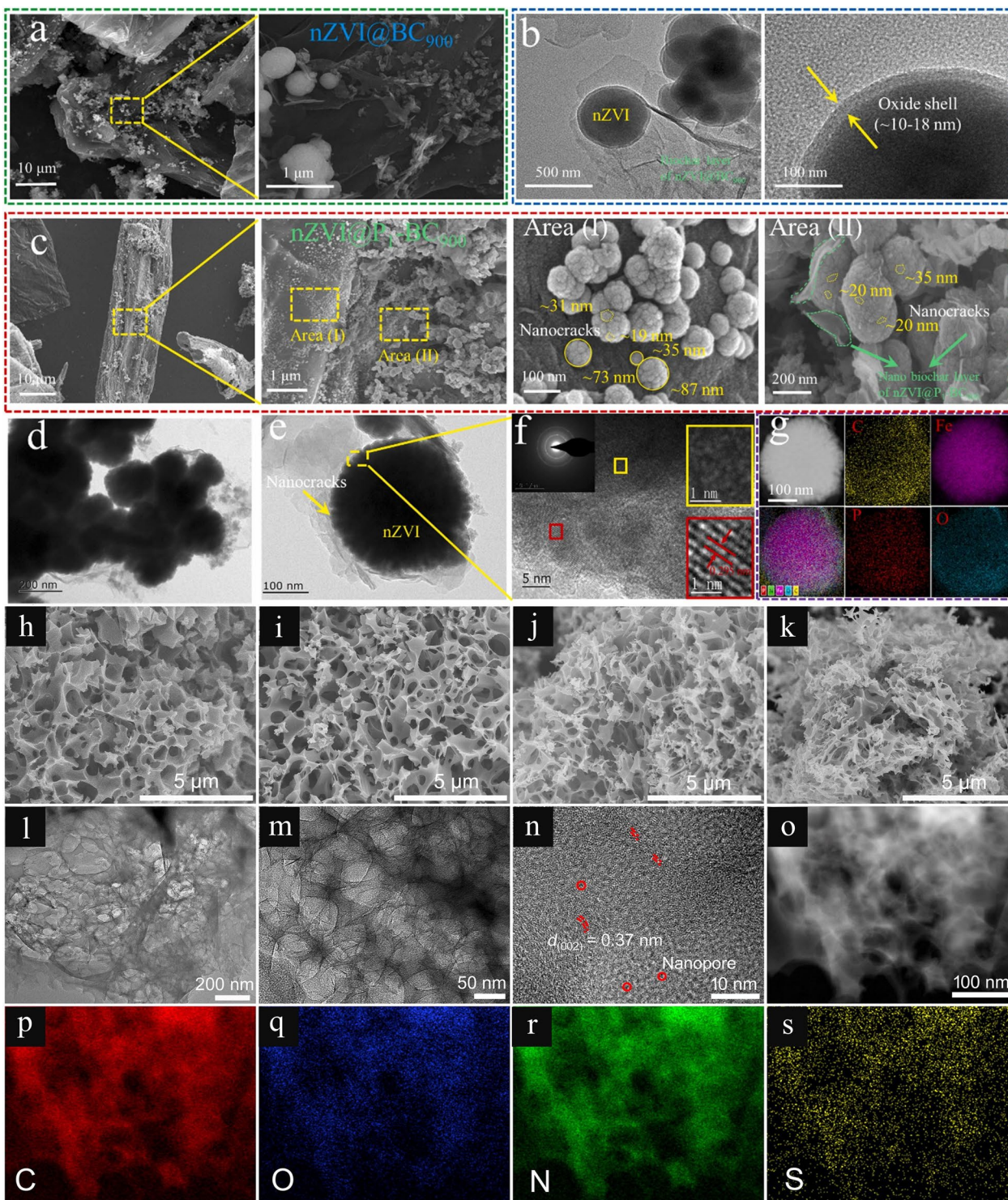
**Fig. 15** **a** SEM and (**b**) TEM micrographs of nZVI@BC_900; **c** SEM and (**d–f**) TEM micrographs of nZVI@P_1-BC_900; **g** EDS elemental mappings of nZVI@P_1-BC_900 (Huang et al. 2023b), Copyright © 2023, Elsevier. **h–k** SEM micrographs of hierarchical porous carbons (HPC-UP-2, HPC-UP-4, HPC-UP-6, and HPC-UP-8); **l–o** TEM micrographs and (**p–s**) EDS elemental mappings of HPC-UP-6 (Zhang et al. 2021), Copyright© 2021, Elsevier
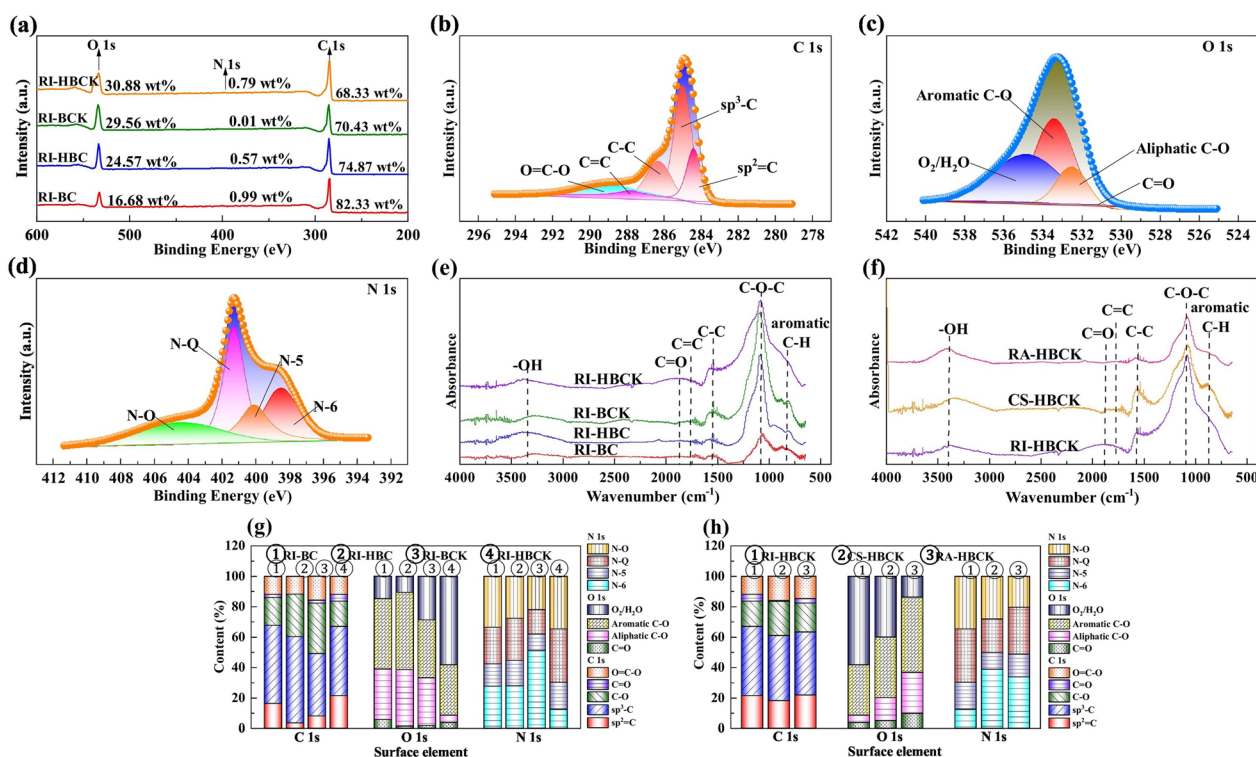
**Fig. 16** **a** XPS full scan; **b** C 1s, **c** O 1s, and (**d**) N 1s XPS spectra of rice straw-derived biochar (RI-HBCK); FTIR spectra of (**e**) RI-BCs and (**f**) HBCKs; Peak resolution results of (**g**) RI-BCs and (**h**) HBCKs (Li et al. 2022a), Copyright © 2022, Elsevier

$sp^2$=C, $sp^3$–C, C–O, C=O, and O=C–O, with corresponding binding energies of 284.7, 285.4, 286.2, 287.4, and 288.7 eV, as illustrated in Fig. 16b. Within the O 1s spectrum of RI-HBCK, a range of oxygen's chemical states was discernible, encompassing C=O, aliphatic C–O, aromatic C–O, and adsorbed $O_2/H_2O$. These oxygen states were associated with distinct binding energies, specifically 531.2, 532.5, 533.0, and 534.8 eV, respectively, as shown in Fig. 16c. In the N 1s spectrum of RI-HBCK, distinct peaks were observed, corresponding to different nitrogen states, specifically pyridinic nitrogen (N–6), pyrrolic nitrogen (N–5), quaternary nitrogen (N–Q), and nitroso nitrogen (N–O), as depicted in Fig. 16d. These nitrogen species had binding energies of 398.5, 400.1, 401.3, and 402.9 eV, respectively. HBCKs exhibited specific ratios of $sp^2$=C, C–O, and O=C–O, with the largest proportion being $sp^3$–C, aromatic C–O, and $O_2/H_2O$, as illustrated in Fig. 16g, h. This composition suggests that HBCKs possess not only an ordered aromatic carbon structure and surface imperfections but also exhibit a certain degree of wettability.

### 4.3 Surface functional groups
Functionalized biochar contains various surface functional groups, such as hydroxyl (–OH), carbonyl (C=O), carboxyl (–COOH), amino (–NH₂), and aromatic (C=C) groups, which play a crucial role in its reactivity and interactions with other molecules. Fourier-transform infrared spectroscopy (FTIR) is a powerful tool employed for examining the surface functional groups and chemical bonds present in biochar materials. Additionally, it can reveal potential alterations in surface functionality following the modification processes of biochar and shed light on the significance of these functional groups in specific applications (Khan et al. 2022a). Numerous research studies have explored the use of FTIR spectroscopy to analyze functional groups within biochar materials. For instance, Li et al. (2022a) employed FTIR spectroscopy to investigate the chemical bonds and functional groups within various biochar materials. The FTIR spectra of biochars obtained by the KHCO₃ activation of hydrochars (referred to as HBCKs) revealed the presence of specific functional groups, including –OH ($\sim$3410 cm$^{-1}$), C=O ($\sim$1740 cm$^{-1}$), C=C ($\sim$1670 cm$^{-1}$), C–O–C ($\sim$1109 cm$^{-1}$), and aromatic C–H ($\sim$817 cm$^{-1}$). In comparison to the other three biochars, HBCKs displayed significantly higher intensities of C=C and C–C bonds, as evidenced by the FTIR spectra depicted in Fig. 16e, f. In another study conducted by Sun et al. (2020), the FTIR spectra of biochars derived from oak and apple tree wood

indicated the existence of various functional groups, including the –OH group at 3760 cm$^{-1}$, aromatic C=C groups at 1360 cm$^{-1}$ and 1450 cm$^{-1}$, and aromatic C–C groups at around 760 cm$^{-1}$.

## 4.4 Crystallinity and phase composition

The degree of crystallinity in biochar is a key factor influencing its reactivity and stability, with higher crystallinity often indicating a more ordered structure. To unravel the crystalline structure and phase composition of functionalized biochars, X-ray diffraction (XRD) stands out as a valuable technique. Despite being primarily carbon-based, functionalized biochar can also incorporate various metal and mineral contents, depending on the choice of biomass feedstock and specific conditions during carbonization and modification processes. XRD analysis is crucial for identifying these crystalline phases and providing detailed insights into the composition and atomic arrangement within these crystal structures.

For instance, Yihunu et al. (2019) conducted an XRD analysis to investigate the crystallinity and phase composition of activated biochar (referred to as BTS) and activated hydrochar (denoted as HTS) derived from teff straw. The XRD patterns of BTS and HTS are presented in Fig. 17a. The sharp peak observed at 24° was attributed to the presence of graphitic carbon, indicating an increase in crystallinity within the BTS structure. Peaks appearing at 16.2° and 27.3° corresponded to $Si(P_2O_7)$ planes, while those at 42° and 26.5° signified the presence of phosphorus oxynitride (denoted as NOP), further indicating a crystalline structure in BTS. In the case of HTS, two distinct peaks emerged at approximately 14.4° and 26°, signifying the presence of $AlPO_4$ planes.

## 4.5 Thermal stability

The thermal stability of functionalized biochar plays a crucial role in its application across various energy and environmental contexts. Thermogravimetric analysis (TGA) stands out as a widely utilized analytical technique for investigating the thermal characteristics and decomposition patterns of bio-carbon materials. This technique entails exposing the sample to a meticulously controlled
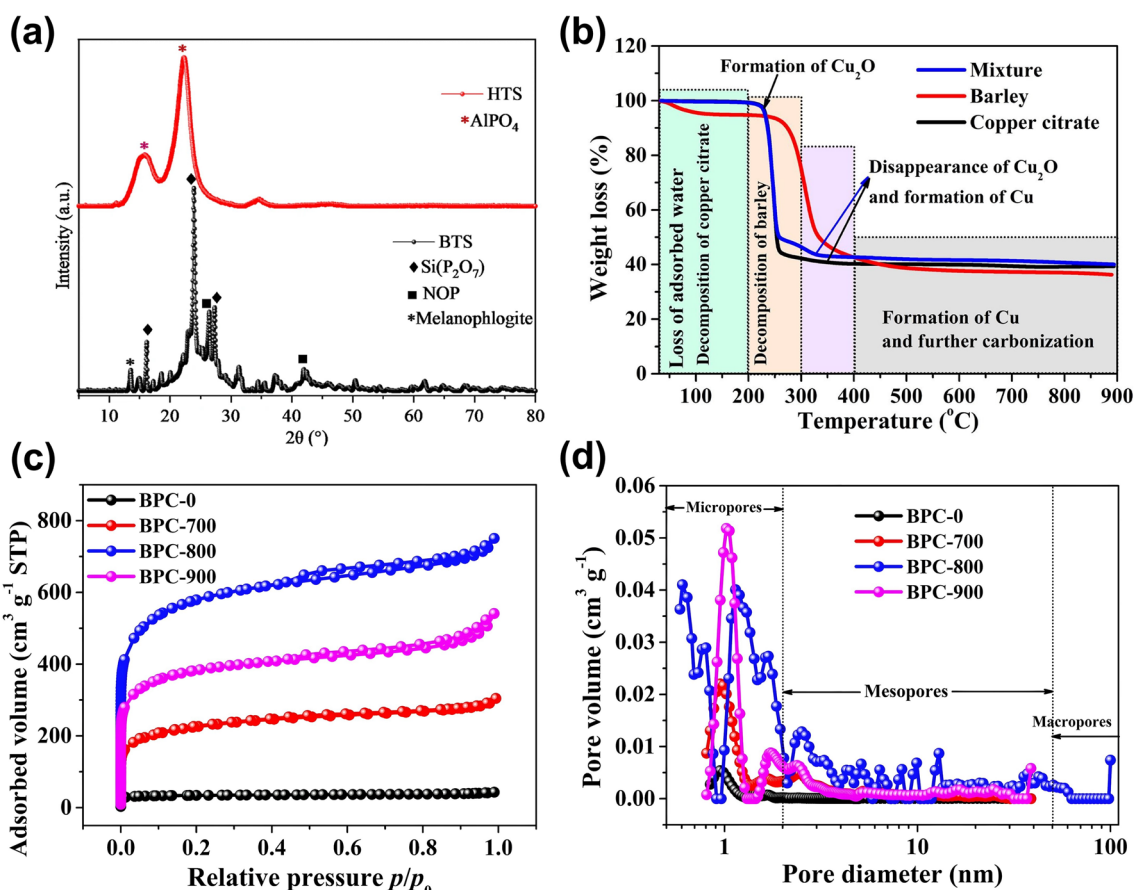


**Fig. 17** **a** XRD patterns of BTS and HTS (Yihunu et al. 2019), Copyright © 2019, Springer Nature. **b** TGA profiles of barley biomass, copper citrate activator, and their resulting bio-carbon (Wan et al. 2020a), Copyright© 2020, Elsevier. **c** N$_2$ adsorption–desorption isotherms and **d** NLDFT pore size distribution of barley-derived porous carbons (Wan et al. 2020a), Copyright© 2020, Elsevier

heating regimen within an inert gas environment, typically using nitrogen ($N_2$), while concurrently monitoring alterations in its weight with respect to temperature. TGA of bio-carbon materials offers valuable insights into their thermal stability, decomposition behavior, and the composition of volatile and non-volatile constituents (Naqvi et al. 2018b).

Numerous research studies have delved into the use of TGA to investigate the thermal characteristics of biomass-derived materials. For instance, in a study conducted by Wan et al. (2020a), TGA was employed to investigate the thermal behaviors of barley biomass, a copper (II) citrate activator, and a mixture of barley and copper (II) citrate over a temperature range of 25–900 °C under a nitrogen ($N_2$) environment, with a heating rate of 10 °C min$^{-1}$, as depicted in Fig. 17b. The primary aim of this analysis was to gain deeper insights into their pyrolysis and activation behaviors. Regarding the barley biomass, a weight loss of 5.3% was observed between 25 and 200 °C, attributed to the evaporation of water vapor. Subsequently, a significant weight loss of ~ 52.1% occurred between 200 and 400 °C, which can be ascribed to the thermal degradation of barley components. Following this, there was a gradual weight loss of 6.4% from 400 to 900 °C, associated with further carbonization of the barley biomass. In the case of the mixture containing barley biomass and copper (II) citrate activator (1:12), only a minimal weight loss of 0.8% was noted between 25 and 200 °C, primarily due to the evaporation of water vapor from the mixture. However, a substantial weight loss of approximately 52.8% occurred between 200 and 300 °C, which significantly exceeds the weight loss observed for fresh barley. This increase can be attributed to the thermal decomposition of both copper (II) citrate and barley components, coupled with strong interactions between these two constituents. These interactions lead to the formation of $Cu_2O$ and partial carbonization of barley. In the temperature range of 300 and 400 °C, a weight loss of 3.7% is associated with the removal of mineral contents and impurities present in the carbon source, along with the gradual transformation of $Cu_2O$ into Cu. Finally, the minimal weight loss observed from 400 to 900 °C can be attributed to the ongoing carbonization of barley and the complete reduction of $Cu_2O$ to Cu.

### 4.6 Surface area and porosity

Specific surface area (SSA) and porosity are crucial parameters for functionalized biochar materials, significantly influencing their efficacy in diverse applications such as catalysis, adsorption, charge storage, and soil amendment. Brunauer–Emmett–Teller (BET) analysis is a highly prevalent analytical technique employed to assess the SSA, porosity, pore size distribution, and

hysteresis (indicative of non-uniform surfaces) of engineered biochar materials. This technique entails the adsorption and desorption of nitrogen gas ($N_2$) at varying relative pressures ($p/p_0$). The resulting dataset, referred to as $N_2$ adsorption–desorption isotherms, furnishes valuable insights into the surface area and porosity characteristics of biochar materials (Kasera et al. 2022). The shape of the $N_2$ adsorption–desorption isotherm can be used to estimate the pore size distribution within the biochar material. For example, a Type I isotherm, featuring a sharp adsorption curve and the absence of hysteresis, is indicative of biochar material primarily composed of micropores (Issaka et al. 2022). Non-local density functional theory (NLDFT) models are employed to compute the porosity of biochar materials, encompassing both pore size and pore size distribution, using datasets derived from $N_2$ adsorption–desorption isotherms, which aids in assessing the accessibility of pores to various reaction molecules (Yang et al. 2023a). Biochar materials can exhibit diverse pore categories, including micropores (< 2 nm), mesopores (2–50 nm), and macropores (> 50 nm).

Many research investigations have explored the use of the BET method to assess the SSA and TPV of engineered biochar materials. For example, Wan et al. (2020a) utilized the BET method to determine the SSA and TPV of barley-derived N, S co-doped porous carbons (BPC-0, BPC-700, BPC-800, BPC-900). The $N_2$ adsorption–desorption isotherms of various carbon materials are depicted in Fig. 17c. BPC-0 displayed the lowest SSA at 132.1 m$^2$ g$^{-1}$, indicating limited porosity in the absence of copper (II) citrate activator. In contrast, BPC-800 showcased an exceptionally high SSA of 2139.6 m$^2$ g$^{-1}$ and a substantial TPV of 1.16 cm$^3$ g$^{-1}$, confirming the crucial role of copper (II) citrate activation in the creation of highly porous carbon materials. Conversely, the SSAs of BPC-700 and BPC-900 were measured at 822.6 and 1422.3 m$^2$ g$^{-1}$, respectively. The lower value for BPC-700 was attributed to an incomplete carbonization-activation at 700 °C, while the higher value for BPC-900 might be the outcome of excessive carbonization-activation, potentially accompanied by pore collapse, at 900 °C. Figure 17d illustrates the pore size distribution of various carbon materials derived from barley. For BPC-0 and BPC-700, the predominant pore sizes fall within the 0.8–1.2 nm range, indicating a typical microporous carbon structure. In contrast, BPC-800 exhibits a well-developed distribution of micropores spanning 0.6–2.0 nm, a significant number of mesopores ranging from 2.0–14.1 nm, and a few macropores spanning 50.6–100.0 nm. This combination of pore sizes is a defining characteristic of hierarchically porous carbon materials.

### 4.7 Graphitization degree and aromaticity

The graphitization degree and aromaticity are key properties of functionalized biochar that play a crucial role in tailoring it for specific applications, including energy storage (as electrodes in supercapacitors), environmental remediation (as adsorbents for pollutants), and agriculture (as soil amendments). Raman spectroscopy is a robust analytical technique employed to investigate these properties by detecting laser light scattering. It offers valuable insights into various aspects, including the chemical composition, the existence of ordered carbon structures such as aromatic rings and graphene-like sheets, the degree of crystallinity, and the surface functionality of engineered biochar materials.

The D and G bands represent two significant spectral features within Raman spectroscopy. The D band is linked to structural disorder or defects within the biochar framework, which arises due to the presence of $sp^3$-hybridized carbon atoms or structural imperfections in the carbon lattice (Sun et al. 2020). The position and intensity of the D band can provide information about the degree of disorder or nature of defects in the biochar materials, such as edge defects, vacancies, or functional groups. A higher D band intensity indicates a higher degree of disorder or more defects. The G band, on the other hand, is associated with the vibrations of $sp^2$-hybridized carbon atoms arranged in a hexagonal lattice, similar to those found in graphite and well-ordered carbon structures. The position and intensity of the G band can provide insights into the degree of graphitization or the presence of ordered carbon structures in biochar materials. A sharp G band indicates a higher degree of graphitization (Cao et al. 2021a). The intensity ratio of the D and G bands ($I_D/I_G$) is often used to assess the degree of graphitization. A lower $I_D/I_G$ ratio suggests a more graphitic and ordered structure, while a higher ratio indicates a more disordered or defective structure. For instance, the rise in the $I_D/I_G$ ratio, going from 0.94 in raw biochar to 0.99 in Fe-modified biochar ($Fe_2O_3$@BC), indicates the presence of defective sites induced by the addition of Fe (Rong et al. 2019).

Several research investigations have explored the use of Raman spectroscopy to examine the surface functionality and graphitic structure of functionalized biochar materials. For example, Schmies et al. (2023) investigated biochar materials derived from sawdust (SD) biomass to assess their surface chemistry using Raman spectroscopy. The results are depicted in Fig. 18a, where the
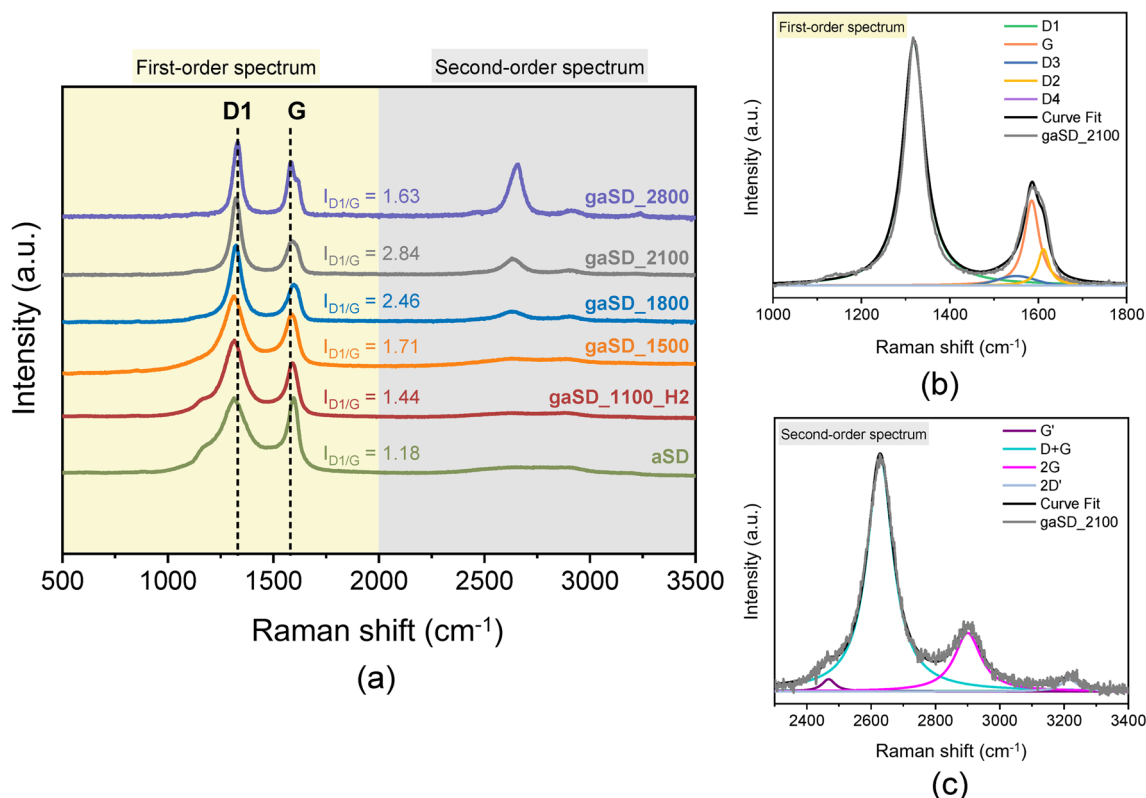


**Fig. 18 a** Raman spectra of sawdust-derived biochars, **b** curve fitting of first-order spectra, and (**c**) curve fitting of second-order spectra (Schmies et al. 2023), Copyright © 2023, The Authors, MDPI

$D_1$ band, positioned at around 1350 cm$^{-1}$, represents imperfections within the carbon structure. Additionally, the G band, situated at ~ 1580 cm$^{-1}$, predominantly signifies well-ordered structures with sp$^2$-hybridized carbon atoms organized in a hexagonal lattice. The $I_{D1}$/$I_G$ ratios of the biochars exhibited a consistent upward trend, ranging from 1.18 to 2.84, as the temperature was elevated from 1100 to 2100 °C. However, after elevating the temperature from 2100 to 2800 °C, the $I_{D1}/I_G$ ratio decreased from 2.84 to 1.63, indicating an enhancement in crystallinity in the gaSD-2800. In the first-order spectrum (Fig. 18b), the $D_1$, $D_2$, and $D_4$ bands originated from disordered graphitic planes, while the $D_3$ band was associated with the presence of amorphous carbon structures and heteroatoms. In the second-order spectrum (Fig. 18c), one can observe the D + G band at around 2650 cm$^{-1}$ and the 2G band at ~ 2950 cm$^{-1}$.
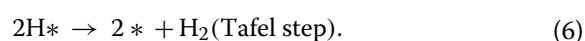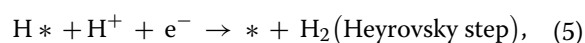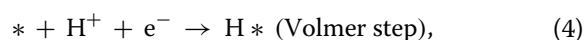
## 4.8 Electrical conductivity

Certain modifications, such as metal and heteroatom doping, have been proven effective in enhancing the electrical conductivity of biochar, making it suitable for various electrochemical applications, particularly as electrodes in supercapacitors. The four-point probe method stands out as a widely utilized and highly accurate technique involving four electrodes to measure the resistance of functionalized biochar and calculate its conductivity. Electrochemical impedance spectroscopy (EIS) is another valuable technique that provides insights into the frequency-dependent conductivity behavior, offering information about charge transport mechanisms. Additionally, cyclic voltammetry (CV) and galvanostatic charge–discharge (GCD) are techniques that further evaluate the conductivity and charge storage capabilities of functionalized biochar.

## 5 Applications of functionalized biochar in energy conversion, wastewater treatment, and environmental remediation
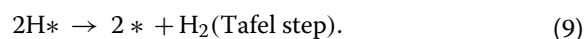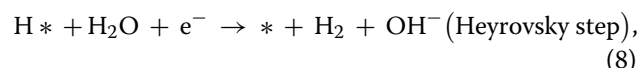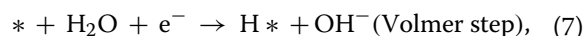
### 5.1 Water splitting

Water splitting is an environmentally friendly process that involves separating water molecules ($H_2O$), a green resource, into hydrogen ($H_2$) and oxygen ($O_2$) gases. This process holds immense promise as $H_2$ is regarded as a clean and sustainable energy carrier capable of substituting fossil fuels, thereby mitigating the environmental issues associated with their use (Chen et al. 2023). Electrolysis stands out as a prominent approach for water splitting, relying on electricity to facilitate the separation of $H_2O$ molecules into $H_2$ and $O_2$. During electrochemical water splitting, two pivotal half-reactions take place: the hydrogen evolution reaction (HER) and the oxygen evolution reaction (OER).

The HER, a two-electron transfer process that takes place at the cathode of an electrolyzer, generates $H_2$ gas. Depending on the chosen electrode material and electrolyte solution, the HER can occur in acidic or alkaline environments. In an acidic electrolyte, the process initiates with the Volmer step (Eq. (4)), where a proton (H$^+$) from the electrolyte adsorbs onto the electrode surface, gaining an electron (e$^-$) to become an adsorbed hydrogen atom (H*). The subsequent Heyrovsky step (Eq. (5)) involves the interaction of H$^+$ and e$^-$ with H*, resulting in the production of $H_2$, which then desorbs from the surface (Wang et al. 2021b). In certain instances, a less common pathway occurs, where two adjacent H* species combine to form $H_2$, known as the Tafel step (Eq. (6)).

$$* + H^+ + e^- \rightarrow H* \text{ (Volmer step)}, \tag{4}$$

$$H* + H^+ + e^- \rightarrow * + H_2 \left(\text{Heyrovsky step}\right), \tag{5}$$

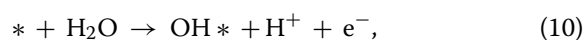$$2H* \rightarrow 2* + H_2 \text{(Tafel step)}. \tag{6}$$

On the other hand, under alkaline conditions, the $H_2O$ molecule approaches the active sites of the electrode surface and splits into an adsorbed hydrogen atom (H*) and a hydroxyl ion (OH$^-$). This step is referred to as the Volmer step (Eq. (7)) and involves breaking a strong O–H bond, often making it the rate-determining step in alkaline HER. In the following Heyrovsky step (Eq. (8)), an adsorbed hydrogen atom (H*) reacts with another $H_2O$ molecule and an electron (e$^-$) from the electrode, forming an $H_2$ molecule and another OH$^-$ ion. Finally, in the Tafel step (Eq. (9)), two adsorbed hydrogen atoms (H*) combine to produce an $H_2$ molecule, which subsequently desorbs from the catalyst surface.

$$* + H_2O + e^- \rightarrow H* + OH^- \text{(Volmer step)}, \tag{7}$$

$$H* + H_2O + e^- \rightarrow * + H_2 + OH^- \left(\text{Heyrovsky step}\right), \tag{8}$$
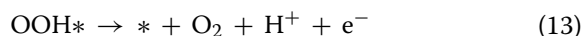
$$2H* \rightarrow 2* + H_2 \text{(Tafel step)}. \tag{9}$$

The key transition state in the HER mechanism is the adsorbed hydrogen atom (H*) on the catalyst surface for both acidic and alkaline media.

For OER, which is a four-electron transfer process that occurs at the anode to produce $O_2$, the mechanism is notably complex and requires a higher overpotential than HER (Kulkarni et al. 2023). The reactions describing the OER mechanism are as follows:

In acidic media:

$$* + H_2O \rightarrow OH* + H^+ + e^-, \tag{10}$$

$$OH* \to O* + H^+ + e^- \tag{11}$$

$$O* + H_2O \to OOH* + H^+ + e^- \tag{12}$$

$$OOH* \to * + O_2 + H^+ + e^- \tag{13}$$

In alkaline media:

$$* + OH^- \to OH* + e^- \tag{14}$$

$$OH* + OH^- \to O* + H_2O + e^- \tag{15}$$
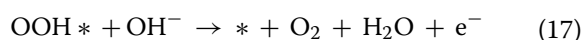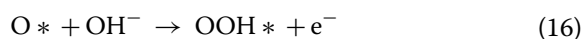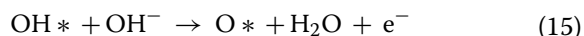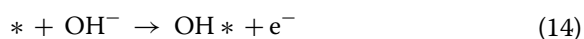
$$O* + OH^- \to OOH* + e^- \tag{16}$$

$$OOH* + OH^- \to * + O_2 + H_2O + e^- \tag{17}$$
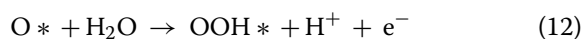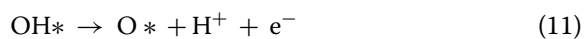
The OER process involves key transition states such as adsorbed hydroxyl (OH*), oxygen (O*), and peroxide (OOH*) species on the catalyst surface.

Researchers are continuously striving to enhance the energy efficiency, cost-effectiveness, and scalability of water-splitting technologies, aiming to make $H_2$ production more sustainable and economically viable. Simultaneously, they are actively engaged in the quest for novel catalysts to replace or improve upon platinum (Pt), ruthenium (Ru), and iridium (Ir)-based catalysts, which are expensive and scarce. One promising innovation in this pursuit is the development of functionalized biochar catalysts derived from bio-sources (Yang et al. 2023b). By leveraging the unique characteristics of functionalized biochar, such as its high surface area, porosity, electrical conductivity, presence of heteroatoms, and diverse functional groups (e.g., –OH, C=O, –COOH, C=C, –NH$_2$), along with incorporating active metallic species, it is possible to boost reaction kinetics and reduce overpotentials, ultimately diminishing the energy requirements for the HER and the OER processes (Ramos et al. 2022).

As part of these efforts, a diverse range of bio-carbon catalysts has been developed for water splitting. For example, in a research study conducted by Xia et al. (2022a), S-doped biochar catalysts, denoted as S-Came and SA-Came, were synthesized using Camellia japonica flowers as the source material. The primary aim of this study was to investigate their potential applications in overall water splitting. To assess the electrochemical performance of both S-Came and SA-Came catalysts, a three-electrode system with a 1.0 M KOH electrolyte solution was employed for both the HER and the OER. Electrochemical impedance spectroscopy (EIS) analysis was conducted on the synthesized biochar catalysts to investigate the charge transfer kinetics. The resulting Nyquist impedance plot disclosed that SA-Came exhibited the shortest vertical line on the plot, with the lowest solution resistance ($R_s$) at 1.90 Ω and the lowest charge-transfer resistance ($R_{ct}$) at 0.27 Ω, confirming faster ion diffusion rates at the electrode–electrolyte interface. The Nyquist admittance plot indicated that the knee frequency of SA-Came, measuring 470.75 Hz, surpassed that of C-AC (31.97 Hz) and S-Came (218.39 Hz), signifying that SA-Came had lower $R_{ct}$ value compared to the other electrocatalysts. To illustrate the catalytic activity of the synthesized bio-carbon materials, the electrochemical specific surface area (ECSA) was measured at 576.25, 140.75, and 1186.0 cm$^2$, and the capacitance current (CC) was recorded at 23.05, 5.63, and 47.44 mF cm$^{-2}$ for C-AC, S-Came, and SA-Came, respectively. The notably increased ECSA and CC values for SA-Came indicate a greater number of active sites and more effective electron transfer capabilities for both the HER and the OER processes. To assess the HER performance, linear sweep voltammetry (LSV) tests were conducted on the S-Came and SA-Came catalysts, along with commercially available activated carbon (C-AC). A commercial Pt/C catalyst, widely recognized as a benchmark for HER, served as the reference electrode material and demonstrated an exceptionally low HER overpotential of 63 mV at 10 mA cm$^{-2}$. Notably, SA-Came outperformed its counterparts, achieving superior HER performance with an impressively low overpotential of 154 mV, surpassing both S-Came and C-AC when targeting a current density of 10 mA cm$^{-2}$. Furthermore, SA-Came displayed the lowest Tafel slope, measuring at 89.92 mV dec$^{-1}$, outperforming both S-Came and C-AC catalysts, underscoring the electrocatalytic efficiency and superior reaction kinetics of SA-Came for the HER. When SA-Came was employed as an anode material in the OER, it demonstrated a low overpotential of 340 mV at a current density of 10 mA cm$^{-2}$, and its Tafel slope was found to be a mere 86.01 mV dec$^{-1}$. The chronoamperometry (CA) curves of SA-Came, recorded at different potentials (−0.25, −0.35, and −0.45 V vs. RHE), exhibited minimal variations and maintained stability for more than 50,000 s. This prolonged resilience underscores its robustness in a highly alkaline environment. Having achieved impressive catalytic activity in both the HER (with an overpotential of 154 mV and Tafel slope of 89.92 mV dec$^{-1}$) and the OER (with an overpotential of 340 mV and Tafel slope of 86.01 mV dec$^{-1}$) at 10 mA cm$^{-2}$, Xia et al. (2022a) proceeded to construct a laboratory-scale water electrolyzer using SA-Came as the catalytic material for both the anode (OER) and cathode (HER) in a 1.0 M KOH aqueous electrolyte, as depicted in Fig. 19a. The LSV curve for overall water splitting revealed a 494 mV overpotential at a current density of 10 mA cm$^{-2}$, as shown in Fig. 19b. Additionally, the SA-Came electrodes exhibited significant stability over 24 h, as demonstrated in Fig. 19c. The
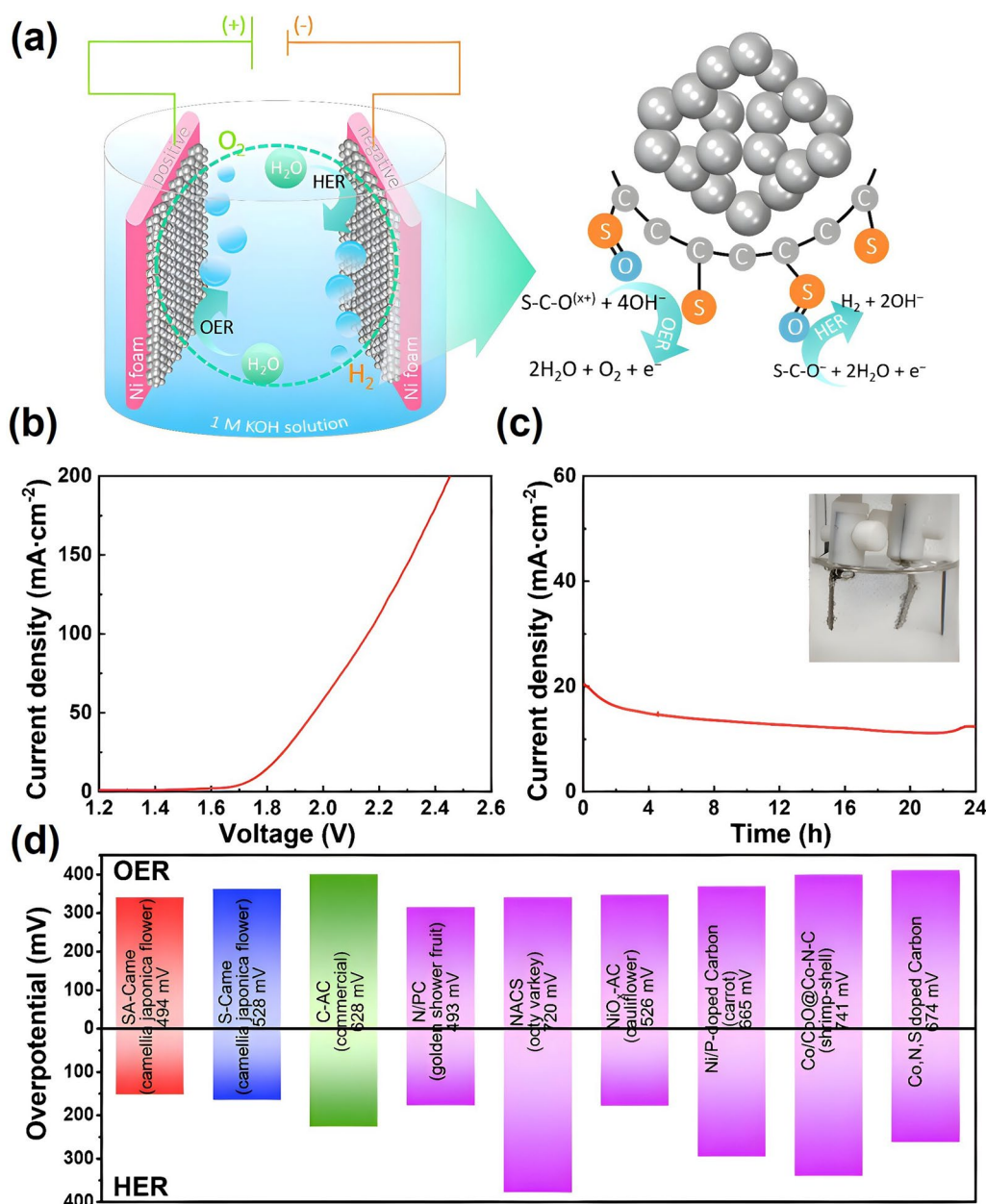
**Fig. 19** **a** Schematic illustration of the water splitting system; **b** LSV and (**c**) CA curves of the SA-Came water splitting system; **d** Comparative evolution of S-doped carbon catalysts for HER and OER overpotentials (Xia et al. 2022a), Copyright © 2022, The Authors, John Wiley & Sons

catalytic activity of the SA-Came catalyst was compared with other S-doped carbon catalysts, and it exhibited the lowest overpotential, as depicted in Fig. 19d. This result highlights SA-Came as an outstanding catalytic material for water electrolysis.

In a recent study conducted by Yan et al. (2023), a functionalized biochar material, denoted as Ni-Mn-S@Ni-Co-LDH@CCs, was developed from chitosan for application in overall water splitting. The electrocatalytic performance of the synthesized catalyst

in both HER and OER was systematically examined within a 1.0 M KOH electrolyte solution. In the context of HER, the Ni-Mn-S@Ni-Co-LDH@CCs catalyst demonstrated exceptional performance, outperforming its counterparts (Fig. 20a). It exhibited superior catalytic activity with a remarkably low overpotential of 97.8 mV, surpassing CCs (199.2 mV), Ni-Co-LDH (159.8 mV), and Ni-Mn-S (125.6 mV) when targeting a current density of 10 mA cm$^{-2}$, as depicted in Fig. 20b. In addition, Ni-Mn-S@Ni-Co-LDH@CCs exhibited
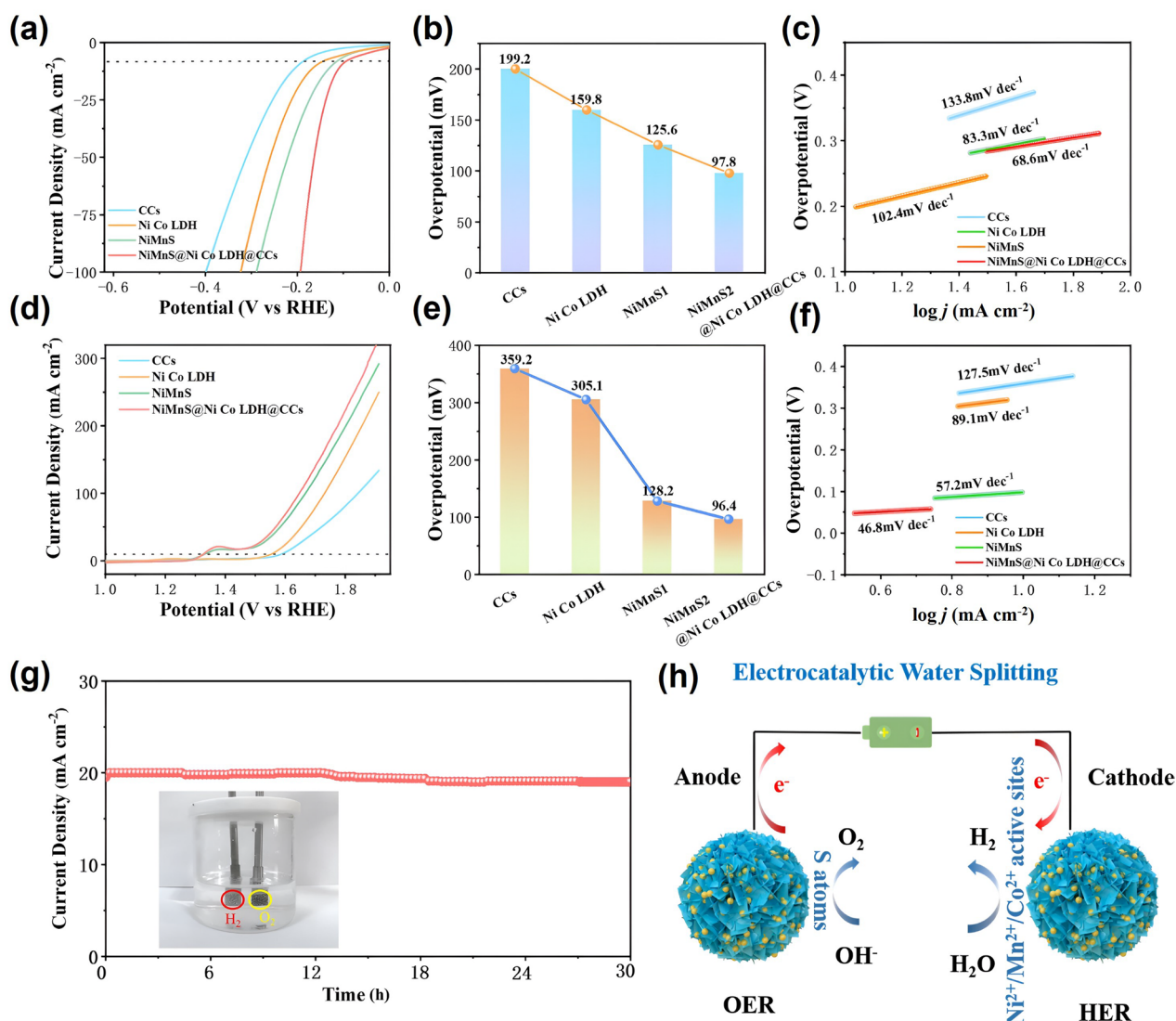
**Fig. 20** Electrochemical performance analysis of Ni-Mn-S@Ni-Co-LDH@CCs electrodes for water splitting: **a** LSV polarization curves for HER, **b** comparison of HER overpotentials, **c** Tafel slopes for HER, **d** LSV polarization curves for OER, (**e**) comparison of OER overpotentials, **f** Tafel slopes for OER, **g** i–t curves for examining catalytic stability, and (**h**) schematics of the electrocatalytic water splitting system (Yan et al. 2023), Copyright © 2023, The Authors, Springer Nature

the lowest Tafel slope (68.6 mV dec$^{-1}$), outperforming CCs (133.8 mV dec$^{-1}$), Ni-Co-LDH (83.3 mV dec$^{-1}$), and Ni-Mn-S (102.4 mV dec$^{-1}$), as shown in Fig. 20c. This underscores the superior reaction kinetics of Ni-Mn-S@Ni-Co-LDH@CCs in the HER. For OER, Ni-Mn-S@Ni-Co-LDH@CCs demonstrated a significantly lower overpotential of 96.4 mV at a current density of 10 mA cm$^{-2}$, compared to CCs (359.2 mV), Ni-Co-LDH (305.1 mV), and Ni-Mn-S (128.2 mV), as depicted in Fig. 20d, e. Moreover, Ni-Mn-S@Ni-Co-LDH@CCs exhibited the smallest Tafel slope, measuring 68.6 mV dec$^{-1}$ (Fig. 20f), indicative of superior reaction kinetics for the OER. The Ni-Mn-S@Ni-Co-LDH@CCs, serving

as the catalytic material for both the anode (OER) and cathode (HER), demonstrated remarkable stability over a 30 h period at 20 mA cm$^{-2}$, as illustrated in Fig. 20g, h.

Yaseen et al. (2022) successfully synthesized the CMO@NC/450 electrocatalyst, derived from waste lotus leaves and comprising Co and MoO$_2$ nanoparticles supported on N-doped carbon nanosheets, to explore its potential application in water splitting. The electrochemical performance of CMO@NC/450 was meticulously examined in a three-electrode setup, utilizing a 1.0 M KOH electrolyte solution, and it demonstrated remarkable results, with notably low

overpotentials of 130 mV and 272 mV at a current density of 10 mA cm$^{-2}$ and Tafel slopes of 91.1 mV dec$^{-1}$ and 45.0 mV dec$^{-1}$ for the HER and the OER, respectively. To evaluate the overall water-splitting performance of the CMO@NC/450 catalyst, a two-electrode setup was employed. In this configuration, CMO@NC/450 served as both the anode for OER and the cathode for HER, using a 1.0 M KOH electrolyte solution. The results of this evaluation highlighted the remarkable overall water-splitting performance of the CMO@NC/450 catalyst, achieving a current density of 10 mA cm$^{-2}$ at a relatively low voltage of 1.629 V.

In another study conducted by Jiang et al. (2022), a novel catalyst known as Co/BCTs-5 was developed, featuring cobalt (Co) supported on biomass carbon tubes (BCTs) derived from natural cotton fibers. This catalyst was specifically designed for use in electrochemical water-splitting applications. The electrocatalytic performance of Co/BCTs-5 was assessed in a three-electrode configuration, utilizing a 1.0 M KOH electrolyte solution for both the HER and the OER. In the context of HER, Co/BCTs-5 exhibited an overpotential of 74 mV at a current density of 10 mA cm$^{-2}$, which was only marginally higher than that of Pt/C (51 mV). Notably, the Tafel slope of Co/BCTs-5, at 48 mV dec$^{-1}$, closely mirrored that of Pt/C (40 mV dec$^{-1}$), indicating superior kinetics for the HER process. In the case of OER, the LSV curve for Co/BCTs-5 displayed an overpotential of merely 330 mV at a current density of 10 mA cm$^{-2}$, a value close to that of RuO$_2$ (280 mV). Co/BCTs-5 also exhibited the lowest Tafel slope, measuring 74 mV dec$^{-1}$, indicating exceptional kinetics for the OER process. The remarkable performance observed in both HER and OER prompted the assembly of an electrolyzer, employing Co/BCTs-5 as both the anode and cathode, for overall water splitting in a 1.0 M KOH electrolyte solution. This configuration necessitated a remarkably low voltage of just 1.40 V at 10 mA cm$^{-2}$, significantly outperforming the Pt/C||RuO$_2$, which required 1.58 V.

In summary, HER plays a pivotal role in H$_2$ production through water splitting, and functionalized biochar catalysts have demonstrated exceptional performance in catalyzing HER under both acidic and alkaline conditions. Detailed data regarding the HER performance of various functionalized biochar catalysts are provided in Table 8.

## 5.2 Fuel cells

Biomass-derived functional carbon materials have recently garnered significant attention in the field of fuel cell research due to their outstanding surface area, porosity, metal loading, diverse functional groups (e.g., −OH, C=O, −COOH, −NH$_2$), electrical conductivity, and thermal stability, which collectively contribute to their excellent performance in fuel cell applications. Fuel cells are vital electrochemical devices that convert the chemical energy inherent in fuels into electrical energy, with the efficiency of this conversion process being paramount for their practical application. They represent a highly promising technology that aligns with the pursuit of a more sustainable and environmentally friendly energy future (Gutru et al. 2023).

Hydrogen fuel cell technology has reached a relatively mature stage of development, with ongoing research focusing on enhancing efficiency and cost-effectiveness. Within the context of a hydrogen fuel cell, the hydrogen oxidation reaction (HOR) and the oxygen reduction reaction (ORR) are pivotal electrochemical processes. Catalysts play a key role in fuel cells, facilitating these electrochemical reactions. The HOR, which occurs at the anode, and the ORR, which takes place at the cathode, together ensure a continuous flow of electrons, empowering the fuel cell to generate clean energy while producing water as its primary byproduct (Park et al. 2022). Advancements in fuel cell technology often revolve around enhancing these catalytic reactions. This entails the development of more efficient and robust catalyst materials, accompanied by efforts to reduce reliance on costly and scarce precious metals like platinum (Pt). The pursuit of superior catalysts is imperative to render fuel cells more cost-effective and accessible for a wide range of applications, spanning from vehicles to stationary power generation and portable devices (Wu et al. 2022). As part of these endeavors, an extensive variety of bio-carbon catalysts have been developed for fuel cells. For instance, Park et al. (2022) explored a range of N-doped carbon materials derived from biomass sources as potential electrocatalysts for the ORR in fuel cells and observed that carbon catalysts doped with metal and nitrogen (Metal-N) showcased a notably superior half-wave potential (E$_{1/2}$) compared to the commercial Pt/C catalyst. Additionally, these catalysts exhibited greater limiting current density (J$_L$) values that surpassed theoretical expectations. This enhanced performance was attributed to their exceptionally porous structures and surface functionality.

Schmies et al. (2023) developed Pt/gaSD-T catalysts derived from sawdust biomass for their application in the ORR within proton exchange membrane (PEM) fuel cells, as depicted in Fig. 21a. The obtained LSV curves revealed that the Pt/gaSD-1100-H$_2$ catalyst exhibited significant catalytic activity, albeit not reaching the J$_L$ value achieved by the commercial Pt/C catalyst, as illustrated in Fig. 21b. This disparity can be primarily attributed to the substantial size of carbon aggregates and the agglomeration of Pt active sites within the prepared catalysts. Additionally, the CV curves in Fig. 21c demonstrated a quasi-rectangular shape for the Pt/gaSD-1100-H$_2$ catalyst, indicating

**Table 8** HER performance of various functionalized biochar catalysts

| Biomass | Biochar preparation | Functionalization | HER catalyst | Electrolyte | Overpotential (mV) | Current density (mA cm$^{-2}$) | Tafel slope (mV dec$^{-1}$) | References |
|---|---|---|---|---|---|---|---|---|
| Natural cotton fibers | One-pot pyrolysis and CoCl$_2$ impregnation: 800 °C, 4 h, Ar/H$_2$ atmosphere | – | Co/BCTs-5 | 1.0 M KOH | 74 | 10 | 48 | Jiang et al. (2022) |
| *Camellia japonica* flower | HTC: 180 °C, 24 h | KOH activation: 800 °C, 2 h, 5 °C min$^{-1}$, N$_2$ atmosphere | SA-Came | 1.0 M KOH | 154 | 10 | 90 | Xia et al. (2022a) |
| Chitosan | Pyrolysis: 700 °C, 2 h, N$_2$ atmosphere | Ni(NO$_3$)$_2$, MnCl$_2$, C$_2$H$_5$NS, Co(NO$_3$)$_2$, and C$_5$H$_8$N$_2$ impregnation followed by hydrothermal treatment: 120 °C, 2 h | Ni-Mn-S@Ni-Co-LDH@CCs | 1.0 M KOH | 97.8 | 10 | 68.6 | Yan et al. (2023) |
| Pomelo peels | Pyrolysis: 400 °C, 1 h, Ar atmosphere | KOH activation: 800 °C, 1 h, Ar atmosphere; (NH$_4$)$_6$Mo$_7$O$_{24}$ impregnation: 800 °C, 3 h, Ar atmosphere | Mo$_2$/NKAB | 0.5 M H$_2$SO$_4$ | 161 | 10 | 57 | Guo et al. (2020) |
| Natural honey | One-pot laser-induced carbonization and RuCl$_3$ impregnation: 6 W | – | 0.04-Ru@CN-6 | 1.0 M KOH<br>0.5 M H$_2$SO$_4$ | 144<br>30 | 10<br>10 | 53<br>60 | Wang et al. (2021c) |
| Peanut root nodules | One-pot pyrolysis and MgCl$_2$ activation: 800 °C, 2 h, Ar atmosphere | – | RN-800 | 1.0 M KOH<br>0.5 M H$_2$SO$_4$ | 11<br>116 | 10<br>10 | 48<br>68 | Zhou et al. (2015) |
| Cellulose | One-pot pyrolysis and (NH$_4$)$_6$Mo$_7$O$_{24}$ impregnation: 800 °C, 1 h, 2 °C min$^{-1}$, N$_2$ atmosphere | – | MoS$_2$@S-CA | 0.5 M H$_2$SO$_4$ | 176 | 10 | 66 | Kong et al. (2018) |
| Pomelo peel | One-pot pyrolysis and Co(NO$_3$)$_2$ impregnation: 800 °C, 6 h, 5 °C min$^{-1}$, N$_2$ atmosphere | – | Co@PPDC | 1.0 M KOH | 154 | 10 | 106 | Min et al. (2020) |
| Pig bone | Pyrolysis: 800 °C, 2 h, N$_2$ atmosphere | – | PBC–800 | 0.5 M H$_2$SO$_4$ | 162 | 10 | 80 | Deng et al. (2021) |
| Green celery | Pyrolysis: 750 °C, 3 h, N$_2$ atmosphere | (NH$_4$)$_6$Mo$_7$O$_{24}$ and CH$_4$N$_2$S impregnation followed by hydrothermal treatment: 220 °C, 18 h | MoS$_2$/BCTM | 0.5 M H$_2$SO$_4$ | 176 | 10 | 51 | Qiao et al. (2019) |

**Table 8** (continued)

| Biomass | Biochar preparation | Functionalization | HER catalyst | Electrolyte | Overpotential (mV) | Current density (mA cm$^{-2}$) | Tafel slope (mV dec$^{-1}$) | References |
|---|---|---|---|---|---|---|---|---|
| Cornstalk | One-pot pyrolysis and $(NH_4)_6Mo_7O_{24}$ impregnation: 900 °C, 4 h, 5 °C min$^{-1}$, Ar atmosphere | – | Mo$_2$C/C | 0.5 M H$_2$SO$_4$ | 114 | 10 | 52 | Mu et al. (2016) |
| | | | | 1.0 M KOH | 117 | 10 | 56 | |
| Waste lotus leaves | One-pot pyrolysis and impregnation with CoCl$_2$ and Na$_2$MoO$_4$: 450 °C, 4 h, 3 °C min$^{-1}$, N$_2$ atmosphere | – | CMO@NC/450 | 1.0 M KOH | 130 | 10 | 91 | Yaseen et al. (2022) |
| Golden shower pod | Pyrolysis: 800 °C, 2 h, 5 °C min$^{-1}$, Ar atmosphere | N-doping using CO(NH$_2$)$_2$: 800 °C, 2 h, Ar atmosphere | N-PC@Ni | 1.0 M KOH | 179 | 10 | 98 | Sathiskumar et al. (2020) |
| Red jujube | One-pot pyrolysis and 24MoO$_3$:P$_2$O$_5$ impregnation: 800 °C, 3 h, 2 °C min$^{-1}$, Ar atmosphere | – | Mo$_2$C@C | 0.5 M H$_2$SO$_4$ | 103 | 10 | 57 | Wang et al. (2020b) |
| Holy leaves | Pyrolysis: 800 °C, 2 h, 10 °C min$^{-1}$, N$_2$ atmosphere | Co(NO$_3$)$_2$ impregnation: 800 °C, 2 h, 10 °C min$^{-1}$, N$_2$ atmosphere | Co-CoO/BC | 1.0 M KOH | 80 | 10 | 46 | Yang et al. (2019b) |
| | | | | 1.0 M KOH | 210 | 10 | 93 | |
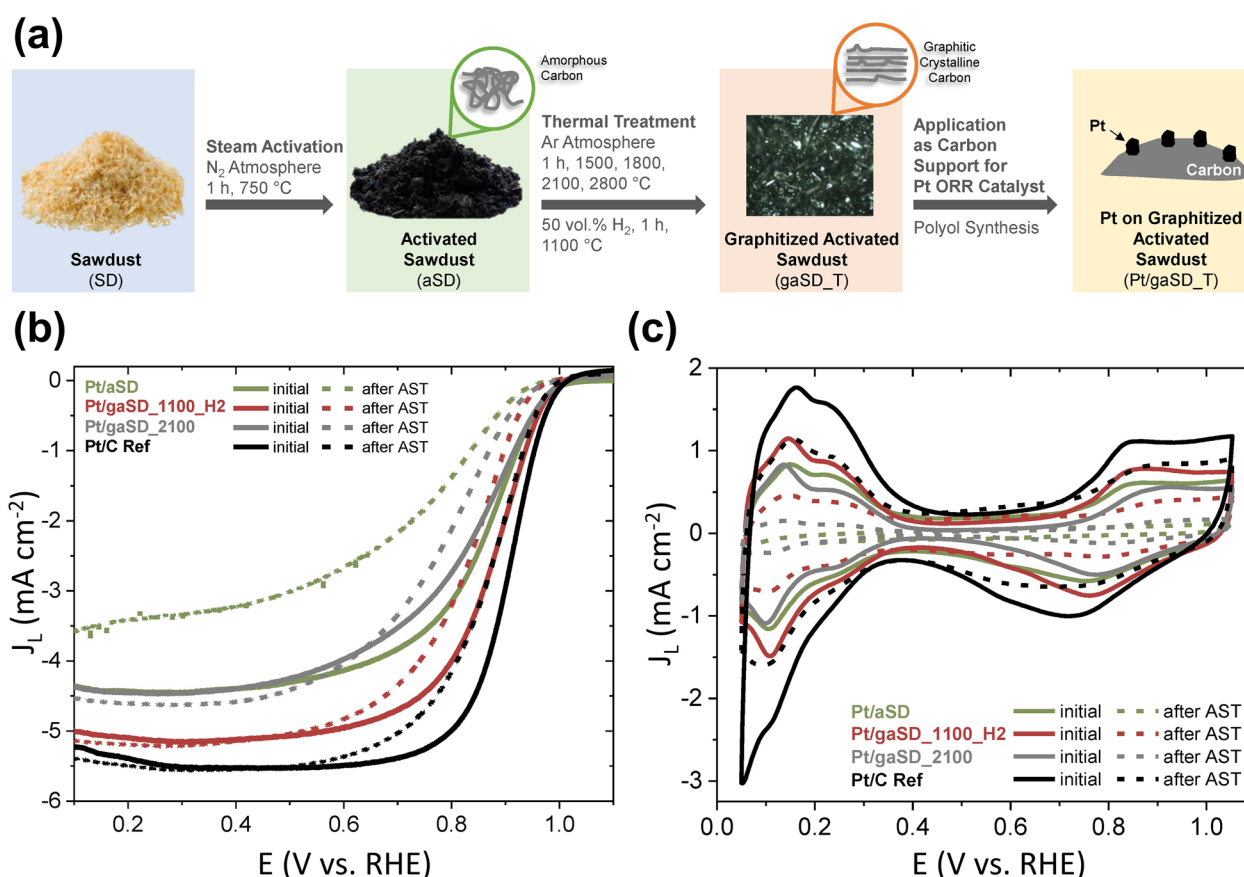
**Fig. 21 a** Schematic synthesis of Pt/gaSD-T electrocatalysts for ORR; **b** LSVs and (**c**) CVs for the prepared catalysts and the commercial Pt/C catalyst (Schmies et al. 2023), Copyright © 2023, The Authors, MDPI

high currents but still falling short of the performance observed with the Pt/C catalyst. The main conclusion of this study underscores the critical importance of achieving a uniform biochar particle size and the even dispersion of Pt on the biochar matrix. These factors, along with high graphitization, are crucial for creating a highly active catalyst for the ORR. In another study, Lu et al. (2021) successfully synthesized an exceptionally active and stable electrocatalyst known as Hemin@NPC-900, derived from acorn shells, for use in ORR within fuel cells. This innovative catalyst possessed an impressive SSA of 819 $m^2 g^{-1}$, characterized by the well-dispersed active sites. The ORR performance of the Hemin@NPC-900 electrocatalyst was evaluated in an $O_2$-saturated 0.1 M KOH electrolyte solution. The LSV curves presented in Fig. 22a revealed that Hemin@NPC-900 outperformed other prepared catalysts, primarily due to its superior $E_o$, $E_{1/2}$, and $J_L$ values. Figure 22b underscores the impressive ORR catalytic activity of Hemin@NPC-900, with values of $E_o = 0.99$ V, $E_{1/2} = 0.84$ V, and $J_L = 3.4$ mA $cm^{-2}$, even slightly surpassing those of the commercial Pt/C catalyst, which recorded $E_o = 0.96$ V, $E_{1/2} = 0.83$ V, and $J_L = 2.9$

mA $cm^{-2}$. Hemin@NPC-900 also exhibited excellent ORR kinetics, as indicated by the Tafel plots presented in Fig. 22c, with a slope of 88 mV $dec^{-1}$, closely resembling the Pt/C kinetics, which had a Tafel slope of 80 mV $dec^{-1}$. Additionally, the LSV curves depicted in Fig. 22d demonstrated that increasing the rotational speed of the rotating disk electrode (RDE) led to a rapid increase in the $J_L$ value of the Hemin@NPC-900 electrocatalyst. The inset image in Fig. 22d shows a K-L plot, revealing a total number of electrons transferred of 3.92. This finding indicates that the ORR process with the Hemin@NPC-900 catalyst followed a 4-electron reduction pathway and adhered to first-order reaction kinetics. Beyond its electrocatalytic activity, the tolerance to methanol ($CH_3OH$) and electrocatalytic stability of the Hemin@NPC-900 catalyst were also investigated. Figure 22e illustrates that there was no discernible change in the LSV and CV curves, even after the addition of 1.0 M $CH_3OH$. Figure 22f further demonstrates the superior electrocatalytic stability of Hemin@NPC-900 ($\Delta E_{1/2} = 35$ mV) in comparison to the commercial Pt/C catalyst ($\Delta E_{1/2} = 48$ mV).
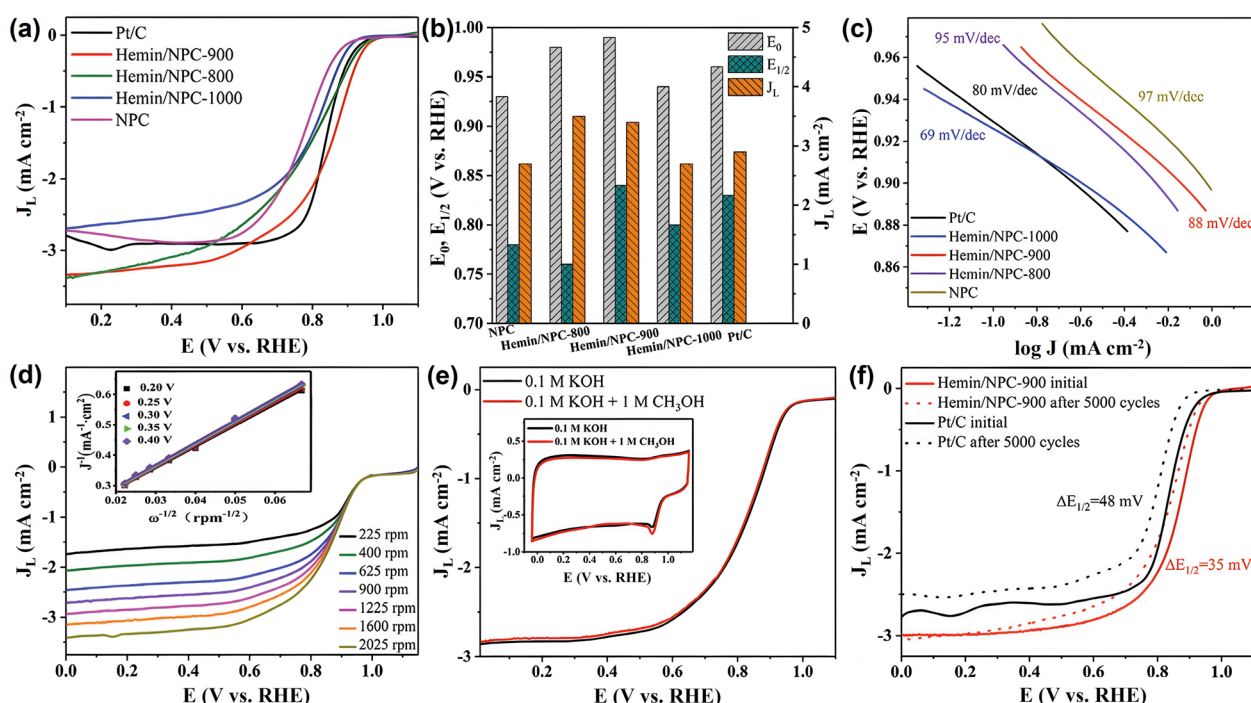
**Fig. 22** **a** LSV curves for the prepared catalysts. **b** Comparative analysis of $E_o$, $E_{1/2}$, and $J_L$. **c** Tafel plots for the prepared catalysts. **d** LSV curves of Hemin/NPC-900 at different rotational speed with (insert) K-L plots. **e** $CH_3OH$ tolerance assessment of Hemin/NPC-900. **f** Electrochemical stability of Hemin/NPC-900 in comparison to commercial Pt/C (Lu et al. 2021), Copyright © 2021 Wiley–VCH GmbH

To summarize, biomass-derived functional carbon materials have shown outstanding performance in catalyzing the ORR in both acidic and alkaline environments. The key factor contributing to the improved ORR performance of these bio-carbons is the presence of numerous active sites that are uniformly distributed. Detailed information regarding the ORR performance of various biochar-based catalysts can be found in Table 9.

### 5.3 Supercapacitors

Functionalized biochar is emerging as a promising electrode material for high-performance supercapacitors, thanks to its favorable combination of structural, physicochemical, and electrochemical attributes. Supercapacitors, also known as ultracapacitors or electrochemical capacitors, are energy storage devices renowned for their exceptional ability to deliver high power and exhibit rapid charge and discharge rates (Wang et al. 2023a). One of the key features of functionalized biochar materials that make them ideal for supercapacitor applications is their highly porous carbon structure, distinguished by a significant specific surface area (SSA). Good electrical conductivity is essential for rapid charge and discharge processes, which is another characteristic of these bio-carbon materials. Functionalized biochars also encompass a

variety of surface functional groups, including hydroxyl (−OH), carbonyl (C=O), and carboxyl (−COOH), which significantly enhance charge transfer and ion adsorption capabilities, ultimately leading to improved specific capacitance (Luo et al. 2022). Researchers are persistently dedicated to enhancing the energy densities in biochar-based supercapacitors to render them more competitive with other energy storage technologies, such as Li-ion batteries. Achieving this goal often involves fine-tuning the surface functionality and hierarchically porous structure of biochar materials to optimize charge storage and ion transport capabilities (Mehdi et al. 2023).

In ongoing efforts to boost energy and power densities, a wide range of biochar materials has been developed for supercapacitor applications. For instance, Xia et al. (2022a) synthesized a highly porous S-doped activated biochar material named SA-Came from Camellia japonica flowers, intending to evaluate its performance as an electrode material in supercapacitor applications. A symmetric supercapacitor (SA-Came//SA-Came) was assembled in a 1.0 M KOH electrolyte, and the schematic diagram of the setup is presented in Fig. 23a. The cyclic voltammetry (CV) curves of the fabricated supercapacitor maintained a quasi-rectangular shape at different scan rates, ranging from 1 to 100 mV s$^{-1}$, and achieved

**Table 9** ORR performance of various biochar-based electrocatalysts

| Biomass | Biochar preparation | Functionalization | ORR catalyst | $S_{BET}$ (m² g⁻¹) | Electrolyte | $E_{onset}$ (V) vs. RHE | $E_{1/2}$ (V) vs. RHE | Tafel slope (mV dec⁻¹) | $J_L$ (mA cm⁻²) | Electrons transferred | References |
|---|---|---|---|---|---|---|---|---|---|---|---|
| Acorn shell | Templated carbonization with $C_3H_6N_6$, $Mg_5(OH)_2(CO_3)_4$, and NaCl: 900 °C, 2 h, 5 °C min⁻¹, $N_2$ atmosphere | Fe impregnation using $C_{34}H_{32}ClFeN_4O_4$: 900 °C, 3 h, 5 °C min⁻¹, $N_2$ atmosphere | Hemin/NPC-900 | 819 | 0.1 M KOH | 0.99 | 0.84 | 88 | 3.40 | 3.92 | Lu et al. (2021) |
| Balsa wood | One-pot pyrolysis and impregnation with $FeCl_3$ and $CO(NH_2)_2$: 1000 °C, 3 h, 5 °C min⁻¹, Ar atmosphere | – | $Fe_2O_3$-CW1000 | 506 | 0.1 M $HClO_4$<br>0.1 M KOH | 0.86<br>0.98 | 0.72<br>0.78 | 115<br>77 | 2.80<br>– | 3.95<br>3.94 | Miao et al. (2022) |
| Coconut shell | Pyrolysis: 550 °C, 1 h, $N_2$ atmosphere | KOH activation: 700 °C, 2 h, Ar atmosphere; N,F-doping using $NH_4F$ and $C_2H_4N_4$: 950 °C, 2 h, 10 °C min⁻¹, Ar atmosphere | NF-PC | 1039 | 0.1 M KOH | 0.99 | 0.84 | 73 | 5.32 | 3.97 | Wang et al. (2021a) |
| Soybean straw | One-pot pyrolysis and impregnation with $C_3H_6N_6$, MgO, and $Fe(NO_3)_3$: 800 °C, 2 h, 3 °C min⁻¹, $N_2$ atmosphere | – | Fe-N-PC | 520 | 0.1 M KOH | 0.99 | 0.85 | 69 | – | 3.97 | Liu et al. (2020b) |
| Plum blossoms | Pyrolysis: 300 °C, 2 h, 5 °C min⁻¹, Ar atmosphere | KOH activation: 900 °C, 1 h, Ar atmosphere; N-doping using $C_3H_6N_6$: 900 °C, 1 h, Ar atmosphere | PBC-A | 2119 | 0.1 M KOH | 0.91 | 0.82 | 84 | 5.96 | 3.83 | Li et al. (2020a) |
| Chitosan | Pyrolysis: 950 °C, 1.5 h, 5 °C min⁻¹, $N_2$ atmosphere | $C_6H_5NH_2$, $C_6H_{18}O_{24}P_6$ and $(NH_4)_2S_2O_8$ modification: 950 °C, 1.5 h, 5 °C min⁻¹, Ar atmosphere | Ca@NP₆C₄ | 135 | 0.1 M KOH | 0.94 | 0.76 | – | 4.43 | 4.03 | Shi and Maimaityiming (2021) |

**Table 9** (continued)

| Biomass | Biochar preparation | Functionalization | ORR catalyst | $S_{BET}$ (m² g⁻¹) | Electrolyte | $E_{onset}$ (V) vs. RHE | $E_{1/2}$ (V) vs. RHE | Tafel slope (mV dec⁻¹) | $J_L$ (mA cm⁻²) | Electrons transferred | References |
|---|---|---|---|---|---|---|---|---|---|---|---|
| Coconut shells | Pyrolysis: 1000 °C, 2 h, 5 °C min⁻¹, N₂ atmosphere | H₃PO₄ activation: 550 °C, 1 h, 10 °C min⁻¹, N₂ atmosphere; N-doping using CO(NH₂)₂: 1000 °C, 2 h, 5 °C min⁻¹, HNO₃/H₂SO₄ functionalization: 120 °C, 2 h | AC-F-U-P | 1071 | 0.1 M KOH | 0.96 | 0.77 | – | – | 3.70 | Borghei et al. (2017) |
| Sunflower seed | One-pot pyrolysis and impregnation with CuCl₂, C₆H₉N₃O₂, and C₂H₄N₄: 850 °C, 3 h, 5 °C min⁻¹, Ar atmosphere | – | Cu/Cu-N-C-850 | 236 | 0.1 M KOH | 0.95 | 0.88 | 74 | – | 3.92 | Li et al. (2022c) |
| Alder wood | Commercial biochar | NaOH activation: 700 °C, 2 h, Ar atmosphere; N-doping using C₂H₄N₄: 800 °C, 1 h, Ar atmosphere | AWC-1 | 2245 | 0.1 M KOH | 0.92 | 0.85 | 56 | 5.90 | 3.98 | Kaare et al. (2020) |
| Sichuan pepper | One-pot pyrolysis and impregnation with C₃₂H₁₆CoN₈, FeCl₃, and ZnCl₂: 900 °C, 2 h, 5 °C min⁻¹, N₂ atmosphere | – | FeCoNC-900 | 1307 | 0.1 M KOH | 0.97 | 0.91 | 91 | – | 3.95 | Gao et al. (2022) |
| Gelatin | One-pot templated carbonization and activation using NaCl: 800 °C, 30 min, 5 °C min⁻¹, N₂ atmosphere | – | NSCA-800 | 839 | 0.1 M KOH | 0.93 | 0.74 | – | 5.79 | 3.93 | Yang et al. (2019a) |

**Table 9** (continued)

| Biomass | Biochar preparation | Functionalization | ORR catalyst | $S_{BET}$ (m² g⁻¹) | Electrolyte | $E_{onset}$ (V) vs. RHE | $E_{1/2}$ (V) vs. RHE | Tafel slope (mV dec⁻¹) | $J_L$ (mA cm⁻²) | Electrons transferred | References |
|---|---|---|---|---|---|---|---|---|---|---|---|
| Walnut peels | HTC: 180 °C, 12 h | N-doping using $C_3H_6N_6$: 800 °C, 4 h, 5 °C min⁻¹, $N_2$ atmosphere | GWS180M800 | – | 0.1 M KOH | 1.01 | 0.82 | 81 | – | 3.95 | Zhou et al. (2022b) |
| Black fungus | HTC: 180 °C, 24 h | $CO(NH_2)_2$ and $ZnCl_2$ activation: 950 °C, 2 h, 5 °C min⁻¹, $N_2$ atmosphere | BF-N-950 | 916 | 0.1 M KOH | 0.98 | 0.91 | 49 | 4.90 | 3.90 | Wang et al. (2020c) |
| Rice husk | One-pot pyrolysis and $ZnCl_2$ activation: 900 °C, 2 h, 5 °C min⁻¹, $N_2$ atmosphere | Fe/S/N doping using $(NH_4)_2Fe(SO_4)_2$: 800 °C, 2 h, 5 °C min⁻¹, $N_2$ atmosphere | Si-Fe/S/N/-RH₃ | 989 | 0.1 M KOH | 0.96 | 0.89 | 75 | 5.23 | 3.90 | Wang et al. (2022a) |
| Tea leaf | Pyrolysis: 1000 °C, 2 h, 10 °C min⁻¹, $N_2$ atmosphere | – | T-NFC | 856 | 0.1 M KOH | 0.81 | 0.66 | – | 5.10 | 3.98 | Wu et al. (2018) |
| Spinach | One-pot pyrolysis and activation with $C_3H_6N_6$, KCl, and NaCl: 900 °C, 2 h, 5 °C min⁻¹, Ar atmosphere | $H_2SO_4$ treatment: 900 °C, 1 h, Ar atmosphere | MSC900-900 | 290 | 0.1 M KOH | 0.94 | 0.88 | 62 | 5.80 | 3.91 | Liu et al. (2020a) |
| Cocoon silk | Pyrolysis: 300 °C, 1 h, 5 °C min⁻¹, $N_2$ atmosphere | $ZnCl_2$ activation: 800 °C, 1 h, 5 °C min⁻¹, $N_2$ atmosphere | PAC-800 | 1274 | 0.1 M KOH | 0.99 | 0.82 | – | 5.00 | 3.96 | Fu et al. (2017) |
| Golden shower pods | Pyrolysis: 800 °C, 2 h, 5 °C min⁻¹, Ar atmosphere | N-doping using $CO(NH_2)_2$: 800 °C, 2 h, Ar atmosphere | N-PC | 839 | 0.1 M KOH | 0.83 | 0.76 | 86 | – | 3.80 | Sathiskumar et al. (2020) |
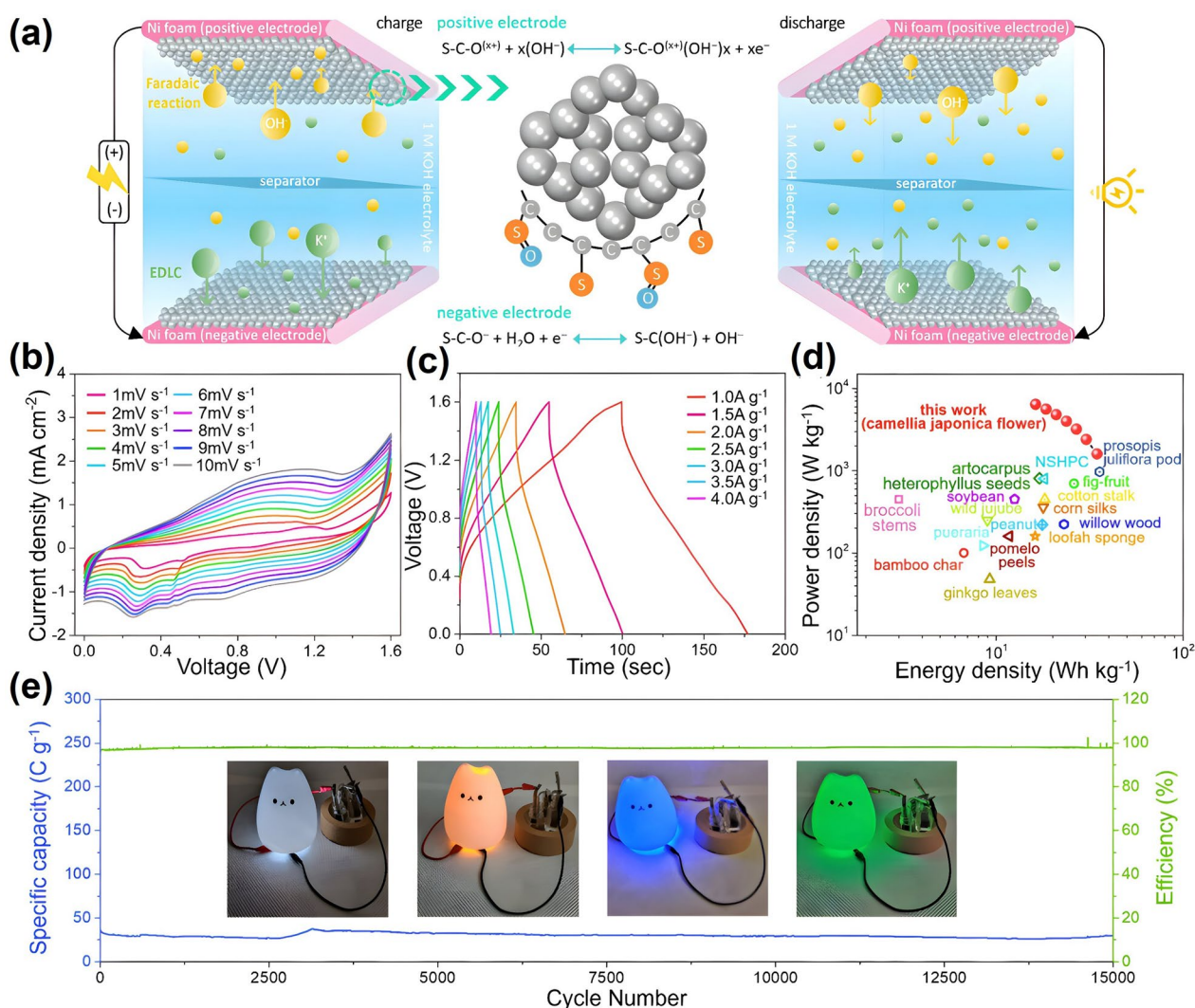
**Fig. 23** **a** Schematic charge mechanism of the SA-Came//SA-Came symmetric supercapacitor; **b** CV curves of the fabricated supercapacitor at various scan rates; **c** GCD curves of the fabricated supercapacitor at various current densities; **d** Ragone plots of the fabricated supercapacitor; **e** Cycling stability and capacitive efficiency of the fabricated supercapacitor (Xia et al. 2022a), Copyright © 2022, The Authors, John Wiley & Sons

a high cell voltage of 1.6 V, as depicted in Fig. 23b. Notably, the specific capacitance obtained from the CV curve at a scan rate of 1 mV s$^{-1}$ reached an impressive value of 117.52 F g$^{-1}$. Galvanostatic charge–discharge (GCD) curves obtained at various current densities, ranging from 1.0 to 4.0 A g$^{-1}$, also achieved a cell voltage of 1.6 V, with a quasi-triangular curve, as shown in Fig. 23c. The specific capacitance determined from the GCD curves was found to be 77.7 F g$^{-1}$ at a current density of 1.0 A g$^{-1}$. Additionally, the GCD curves revealed that the fabricated supercapacitor exhibited the highest energy density of 34.5 Wh kg$^{-1}$ at a power density of 1600 W kg$^{-1}$. A Ragone plot, presented in Fig. 23d, demonstrated that the SA-Came electrode outperformed other biomass-derived electrodes in terms of both energy and power density.

Notably, after undergoing 15,000 cycles at 4.0 A g$^{-1}$, the capacitance of the SA-Came//SA-Came supercapacitor retained an impressive 98%, as shown in Fig. 23e.

In another investigation conducted by Mian et al. (2023), activated biochar was produced from banana peels and referred to as BN-Ac. Cellulose nanofiber (CNF) was employed as a binding material to create a BN-Ac/CNF electrode for evaluating its performance in a coin cell supercapacitor. The schematic diagram illustrating the preparation of the BN-Ac/CNF coin cell supercapacitor is presented in Fig. 24a. The practical electrochemical performance of BN-Ac/CNF in a symmetric two-electrode coin cell supercapacitor was assessed using a 6.0 M KOH electrolyte solution. The CV curves in Fig. 24b exhibited quasi-rectangular shapes and
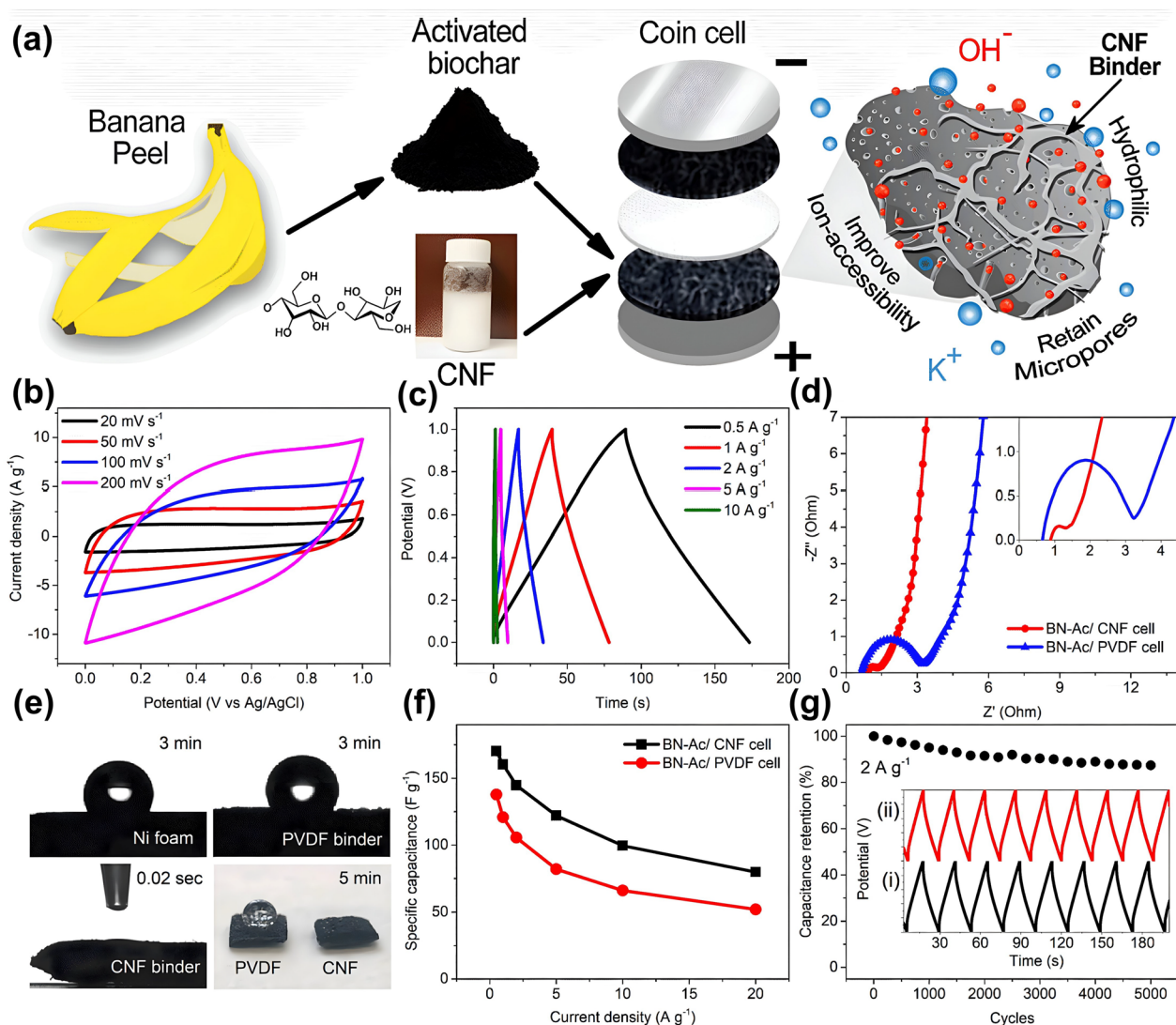
**Fig. 24 a** Schematic of the BN-Ac/CNF coin cell preparation, **b** CV curves at different scan rates, **c** GCD profiles, **d** EIS plots, **e** water contact angle measurements on different electrodes, **f** current density vs. specific capacitance plot, and (**g**) cycling stability evaluation of the supercapacitor (Mian et al. 2023), Copyright © 2023, Elsevier

extended up to a cell voltage of 1.0 V. The GCD curves in Fig. 24c displayed symmetric triangular shapes at various current densities, ranging from 0.5 to 10 A g$^{-1}$, and showed a voltage drop of 0.013 V at 0.5 A g$^{-1}$. The specific capacitance of BN-Ac/CNF was measured at 170.1 F g$^{-1}$ @ 0.5 A g$^{-1}$, which was significantly higher than that of the BN-Ac/polyvinylidene fluoride (PVDF) electrode, which measured 137.8 F g$^{-1}$ @ 0.5 A g$^{-1}$. Furthermore, the replacement of BN-Ac/PVDF with BN-Ac/CNF electrode significantly reduced the internal resistance from 1.5 to 0.76 Ω, as indicated in Fig. 24d. In Fig. 24e, it's evident that a water droplet disperses immediately on BN-Ac/CNF in 0.02 s, illustrating exceptionally high wetting characteristics and fast electrolyte access to the

BN-Ac/CNF electrodes in comparison to Ni foam and BN-Ac/PVDF, which did not change their contact angles even after 3 min. The BN-Ac/CNF electrode maintained a specific capacitance of 123.8 F g$^{-1}$ @ 5 A g$^{-1}$ and 106.2 F g$^{-1}$ @ 10 A g$^{-1}$, as displayed in Fig. 24f. Additionally, it demonstrated an energy density of 5.7 Wh kg$^{-1}$ at a power density of 2500 W kg$^{-1}$ and maintained 2.9 Wh kg$^{-1}$ at a high power density of 21,300 W kg$^{-1}$. Remarkably, BN-Ac/CNF also exhibited 87.3% capacitance retention after 5000 cycles at 2 A g$^{-1}$, as shown in Fig. 24g.

Yan et al. (2022) developed a biochar material derived from basswood, referred to as FA-OC2, for its application as an electrode in high-performance supercapacitors. The process for synthesizing FA-OC2 is visually
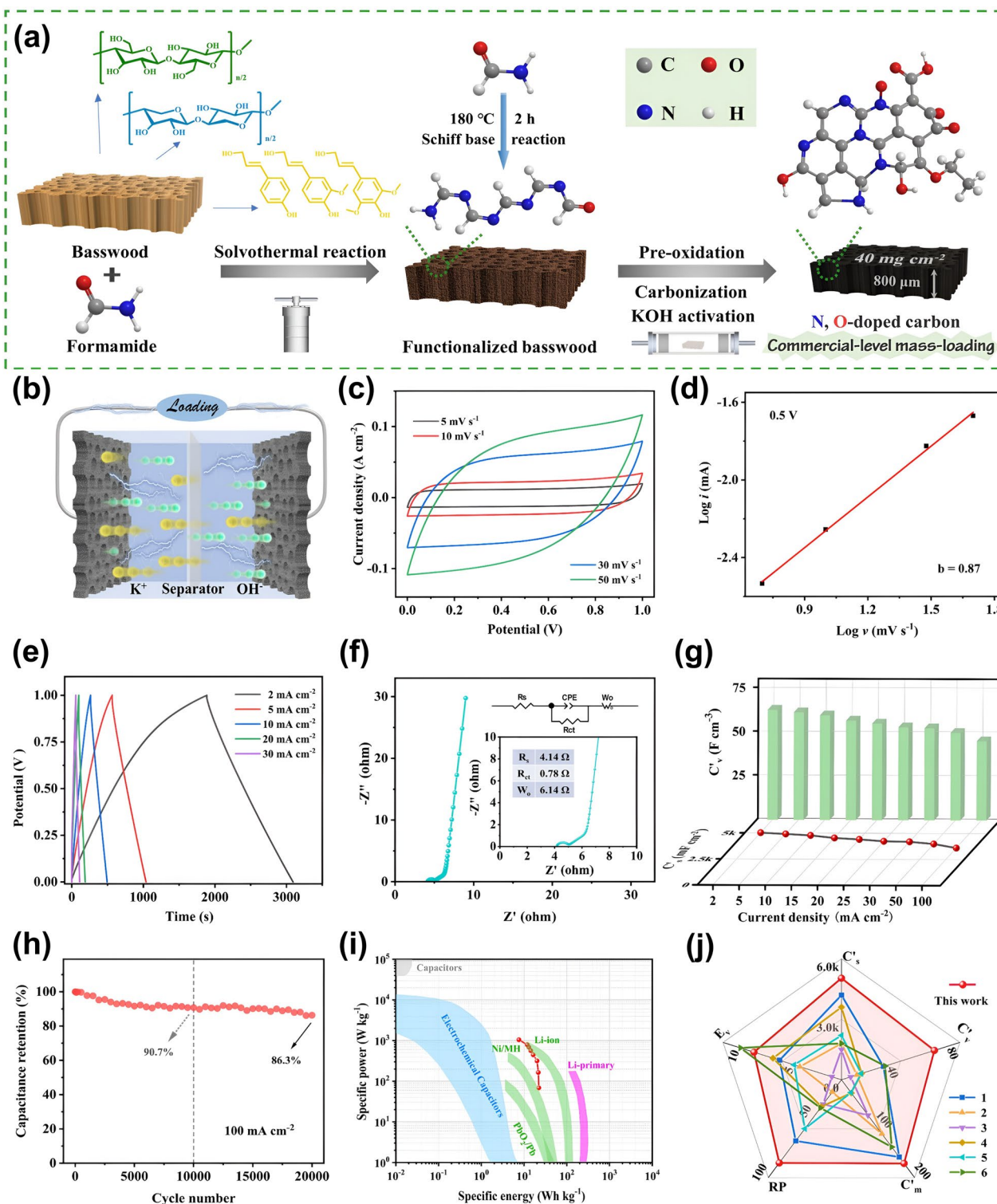
**Fig. 25 a** Schematic diagram for the synthesis of N,O-doped carbon; **b** FA-OC2//FA-OC2 symmetric supercapacitor device; **c** CV curves at different scan rates; **d** Plot of log *i* vs. log *v*; **e** GCD curves; **f** EIS plots and corresponding equivalent circuit diagram; (**g**) Rate performance and corresponding C'$_v$; **h** Cyclic stability at 100 mA cm$^{-2}$; **i** Comparison of Ragone plots of FA-OC2/FA-OC2 with other energy storage devices; **j** Radar plots of the FA-OC2// FA-OC2 device compared with other biocarbon-based devices (Yan et al. 2022), Copyright © 2022, All Authors, Elsevier

depicted in Fig. 25a. To assess its suitability for practical supercapacitors, a symmetrical supercapacitor (FA-OC2//FA-OC2) with a dual-electrode configuration was fabricated, employing a 6.0 M KOH electrolyte, as illustrated in Fig. 25b. The CV curves of the fabricated supercapacitor consistently displayed quasi-rectangular shapes at various scan rates, ranging from 5 to 50 mV s$^{-1}$, as shown in Fig. 25c. The corresponding b value of 0.87 confirmed that the overall capacitance of the supercapacitor results from a combination of double-layer capacitance and pseudocapacitance mechanisms, indicating a synergistic effect, as depicted in Fig. 25d. The GCD curves of the supercapacitor device, obtained at various current densities, ranging from 2 to 30 mA cm$^{-2}$, exhibited symmetric triangular shapes, as shown in Fig. 25e. Notably, the two-electrode FA-OC2//FA-OC2 configuration exhibited a lower specific capacitance (173 F g$^{-1}$ @ 0.05 A g$^{-1}$) compared to the three-electrode configuration (224 F g$^{-1}$ @ 0.05 A g$^{-1}$). This difference is likely attributed to the increased solution resistance ($R_s$) and charge transfer resistance ($R_{ct}$), as demonstrated in Fig. 25f. The FA-OC2//FA-OC2 supercapacitor displayed specific capacitance ($C'_s$) values of 5038, 4421, and 3623 mF cm$^{-2}$ at current densities of 2, 20, and 100 mA cm$^{-2}$ (equivalent to 0.05, 0.50, and 2.50 A g$^{-1}$). These values corresponded to mass-specific capacitance ($C'_m$) values of 173, 152, and 124 F g$^{-1}$ and volumetric capacitance ($C'_v$) values of 63, 55, and 45 F cm$^{-3}$, respectively, as presented in Fig. 25g. Furthermore, the maximum energy density of the FA-OC2//FA-OC2 supercapacitor at a current density of 2 mA cm$^{-2}$ (0.05 A g$^{-1}$) was 0.65 mWh cm$^{-2}$ (22.44 Wh kg$^{-1}$, 8.15 mWh cm$^{-3}$), and the power density at 100 mA cm$^{-2}$ (2.50 A g$^{-1}$) was 58 mW cm$^{-2}$ (1996 W kg$^{-1}$, 725 mW cm$^{-3}$). The cycling stability of FA-OC2//FA-OC2 demonstrated remarkable durability, with the supercapacitor maintaining high stability over 20,000 cycles at a current density of 100 mA cm$^{-2}$ (2.5 A g$^{-1}$) and a significant capacity retention rate of 86.3%, as shown in Fig. 25h. A Ragone plot in Fig. 25i offers a comprehensive comparison of the energy density and power density of the FA-OC2//FA-OC2 supercapacitor with various other energy storage devices, including batteries, electrochemical capacitors, and traditional capacitors. Additionally, the Radar plots, depicted in Fig. 25j, showcase the specific capacitance ($C'_s$), rate performance (RP), and energy density ($E_v$) of the FA-OC2//FA-OC2 supercapacitor in comparison to other supercapacitors derived from bio-carbon materials.

In summary, highly porous carbon materials derived from biomass sources have proven to be outstanding performers in the realm of high-performance supercapacitors. These materials have played a pivotal role in elevating both the energy density and power density of supercapacitors, whether operating in acidic or alkaline electrolytes. For a comprehensive overview of the capacitance performance of various biochar materials, please refer to the detailed data presented in Table 10.

### 5.4 Wastewater treatment and resource recovery

The continuous growth of the global population and economic development have resulted in an ever-increasing demand for resources, including water, energy, and materials. This heightened demand for resources underscores the critical need for resource reclamation from wastewater. Biochar materials offer a sustainable solution for wastewater treatment and resource recovery by facilitating the removal of contaminants, the extraction of valuable components, enhancing water quality, and aligning with the principles of the circular economy through the conversion of waste into valuable resources (Yang et al. 2020b). Thanks to its porous structure, surface charge, and abundant functional groups (e.g., –OH, C=O, –COOH, –NH$_2$), biochar boasts high catalytic activity and adsorption capacity, making it exceptionally effective at eliminating various contaminants from wastewater (Kamali et al. 2021).

Wastewater originates from diverse sources, each with its unique set of contaminants. Industrial wastewater primarily contains heavy metals and organic pollutants, whereas municipal wastewater typically includes nutrients. Agricultural wastewater is known for its presence of pesticides and heavy metals, while stormwater runoff can carry metals, organic matter, and biological contaminants (Khan et al. 2022b). Biochar excels at adsorbing nutrients such as phosphorus (P) and nitrogen (N), heavy metals like lead (Pb), mercury (Hg), cadmium (Cd), chromium (Cr), and arsenic (As), as well as organic contaminants such as humic acid (HA) and tetracycline (TC), thus significantly improving water quality and supporting water resource recovery (Jellali et al. 2021). The adsorption mechanism of biochar for the removal of nutrients, metals, and organic contaminants is illustrated in Fig. 26. Furthermore, biochar can be employed as a biofilter for the treatment of stormwater and domestic wastewater, leading to efficient filtration and contaminant removal. Recovered water can be reused for various non-potable purposes, such as irrigation or industrial processes, contributing to the conservation of freshwater resources (Li et al. 2022b).

Numerous research studies have explored the potential of biochar in effectively removing heavy metals, nutrients, and organic contaminants from wastewater sources. One such study conducted by Ou et al. (2023) involved the development of Fe, Ca-impregnated biochar, referred to as ZFCO-BC, derived from bamboo biomass, for the adsorption of phosphate in industrial wastewater from

**Table 10** Biomass-derived porous carbon electrodes for supercapacitors

| Biomass | Biochar preparation | Functionalization | Electrode material | $S_{BET}$ ($m^2$ $g^{-1}$) | Internal resistance ($\Omega$) | Specific capacitance (F $g^{-1}$) | Current density (A $g^{-1}$) | Electrolyte | Energy density (Wh $kg^{-1}$) | Power density (W $kg^{-1}$) | Cycling stability | References |
|---|---|---|---|---|---|---|---|---|---|---|---|---|
| *Camellia japonica* | HTC: 180 °C, 24 h | KOH activation: 800 °C, 2 h, 5 °C $min^{-1}$, $N_2$ atmosphere | SA-Came | — | 1.90 | 125 | 2.0 | 1.0 M KOH | 34.5 | 1600 | 15,000 (98.0%) | Xia et al. (2022a) |
| Banana peels | Pyrolysis: 600 °C, 1 h, 10 °C $min^{-1}$, $N_2$ atmosphere | KOH activation: 700 °C, 2 h, $N_2$ atmosphere | BN-Ac/CNF | 1486 | 0.76 | 268.4 | 5.0 | 6.0 M KOH | 5.7 | 2500 | 5,000 (87.3%) | Mian et al. (2023) |
| Basswood | Pyrolysis: 1000 °C, 2 h, 5 °C $min^{-1}$, $N_2$ atmosphere | KOH activation: 800 °C, 2 h, 5 °C $min^{-1}$, $N_2$ atmosphere | FA-OC2 | 313 | 0.98 | 223.9 | 0.05 | 6.0 M KOH | 22.4 | 1997 | 20,000 (86.3%) | Yan et al. (2022) |
| Food waste | Pyrolysis: 700 °C, 2 h, 10 °C $min^{-1}$, $N_2$ atmosphere | – | FWHB-700 | 693 | 0.49 | 461 | 1.0 | 6.0 M KOH | 10.0 | 125 | 10,000 (88.2%) | Wang et al. (2023c) |
| *Cannabis sativa* | Pyrolysis: 600 °C, 1 h, 5 °C $min^{-1}$, $N_2$ atmosphere | $Co(NO_3)_2$ and $Ni(CH_3COO)_2$ impregnation: 600 °C, 2 h, 5 °C $min^{-1}$, $N_2$ atmosphere | C@ZIF-67–600 | 175 | 0.19 | 274.4 | 1.0 | 3.0 M KOH | 85.1 | 750 | 20,000 (87.0%) | Yue et al. (2022) |
| *Salvia splendens* | One-pot pyrolysis and NaCl activation: 800 °C, 2 h, 4 °C $min^{-1}$, $N_2$ atmosphere | – | GPCN-SS-800 | 1051 | 0.97 | 294 | 1.0 | 6.0 M KOH | 8.4 | 249 | 20,000 (94.7%) | Liu et al. (2018) |
| | | | | | | | | 1.0 M $Na_2SO_4$ | 12.1 | 34,500 | 20,000 (92.5%) | |
| Pruce bark | HTC: 180 °C, 12 h | KOH activation: 900 °C, 2 h, 5 °C $min^{-1}$, $N_2$ atmosphere | VAGNA-900 | 2385 | 0.28 | 398 | 0.5 | 6.0 M KOH | 10.6 | 50 | 10,000 (96.3%) | Sun et al. (2018b) |
| | | | | | | | | 1.0 M $TEABF_4$/AN | 74.4 | 744 | 10,000 | |

**Table 10** (continued)

| Biomass | Biochar preparation | Functionalization | Electrode material | $S_{BET}$ (m² g⁻¹) | Internal resistance (Ω) | Specific capacitance (F g⁻¹) | Current density (A g⁻¹) | Electrolyte | Energy density (Wh kg⁻¹) | Power density (W kg⁻¹) | Cycling stability | References |
|---|---|---|---|---|---|---|---|---|---|---|---|---|
| *Enteromorpha prolifera* | HTC: 180 °C, 24 h; Pyrolysis: 450 °C, 2 h, 2 °C min⁻¹, N₂ atmosphere | KOH activation: 800 °C, 1 h, 2 °C min⁻¹, N₂ atmosphere | AHC-800 | 2000 | 0.19 | 184 | 0.5 | 6.0 M KOH | 7.0 | 3000 | 10,000 (96.0%) | Ren et al. (2018) |
| Clover | HTC: 160 °C, 6 h; Calcination: 850 °C, 3 h, 10 °C min⁻¹ | KOH activation: 850 °C, 1 h, 10 °C min⁻¹ | NHPCS | 2244 | 0.93 | 451 | 0.5 | 1.0 M H₂SO₄ | 58.4 | 500 | 30,000 (99.3%) | Wang et al. (2018a) |
| *Eleocharis dulcis* | One-pot pyrolysis and KOH activation: 800 °C, 1 h, N₂ atmosphere | – | NPC-3 | 2454 | – | 227 | 1.0 | 6.0 M KOH | 26.3 | 3694 | 10,000 (94.2%) | Zhou et al. (2020) |
| Squid gladius chitin | Pyrolysis: 500 °C, 3 h, 10 °C min⁻¹, N₂ atmosphere | KOH activation: 750 °C, 1.5 h, 10 °C min⁻¹, N₂ atmosphere | SGAC | 1129 | 0.73 | 204 | 0.5 | 1.0 M H₂SO₄ | 4.5 | 9900 | 25,000 (100%) | Raj et al. (2018) |
| *Juncus* | One-pot pyrolysis and ZnCl₂ activation: 800 °C, 2 h, 5 °C min⁻¹ | – | NDPC-3-800 | 1380 | – | 291 | 0.5 | 6.0 M KOH | 28.6 | 30,153 | 10,000 (94.5%) | He et al. (2020) |
| Bristlegrass seeds | One-pot pyrolysis and KOH activation: 800 °C, 2 h, 10 °C min⁻¹, Ar atmosphere | – | N/S/O-HPC | 1484 | 0.80 | 391 | 0.5 | 6.0 M KOH | – | – | 10,000 (97.2%) | Zhou et al. (2018) |
| | | | | | | | | 1.0 M Na₂SO₄ | 20.2 | 500 | 10,000 (94.2%) | |

**Table 10** (continued)

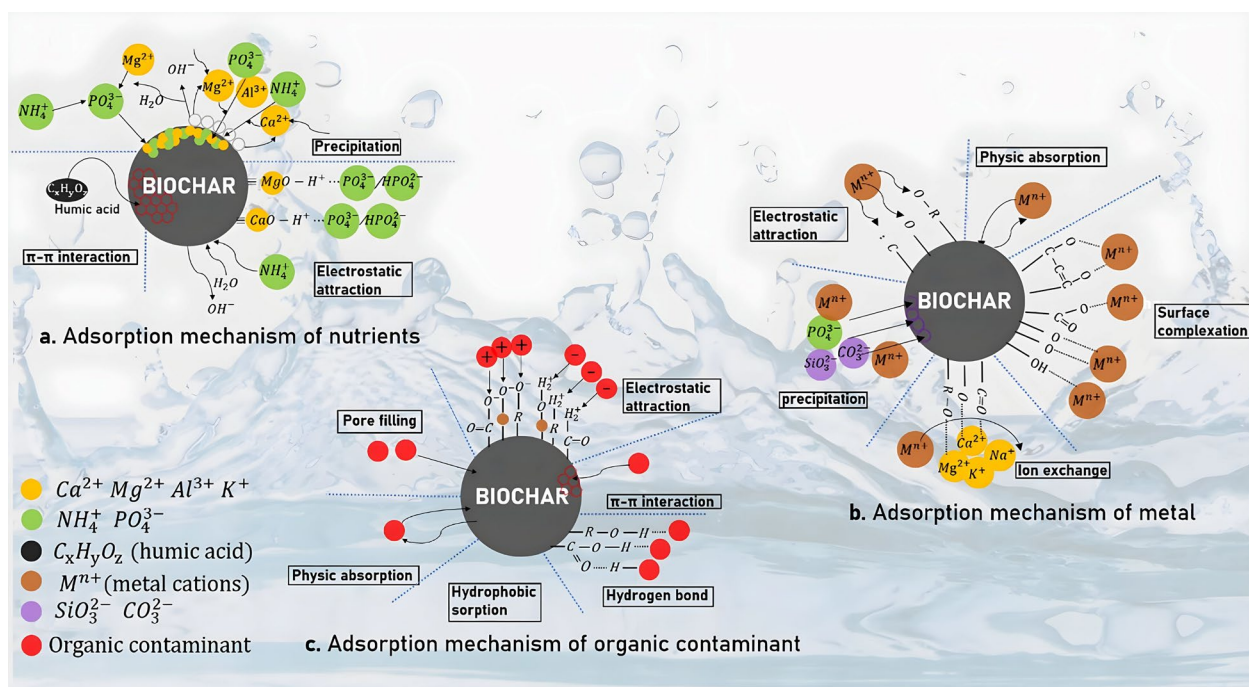| Biomass | Biochar preparation | Functionalization | Electrode material | $S_{BET}$ (m² g⁻¹) | Internal resistance (Ω) | Specific capacitance (F g⁻¹) | Current density (A g⁻¹) | Electrolyte | Energy density (Wh kg⁻¹) | Power density (W kg⁻¹) | Cycling stability | References |
|---|---|---|---|---|---|---|---|---|---|---|---|---|
| Fungus | Pyrolysis: 300 °C, 2 h, 2 °C min⁻¹, N₂ atmosphere | KOH activation: 800 °C, 2 h, 2 °C min⁻¹ | NHPC-800 | 1708 | – | 228 | 0.5 | 2.0 M KOH | 4.3 | 250 | 10,000 (100%) | Zou et al. (2019) |
| Silkworm excrement | Pyrolysis: 900 °C, 3 h, 10 °C min⁻¹, N₂ atmosphere | KOH activation: 600 °C, 2 h, 10 °C min⁻¹, N₂ atmosphere | N-P-S–O-CNs | 2258 | 0.79 | 401 | 0.5 | 6.0 M KOH | – | – | 10,000 (93.8%) | Lei et al. (2018) |
| Cattle bones | Pyrolysis: 400 °C, 3 h, 5 °C min⁻¹, N₂ atmosphere | KOH activation: 850 °C, 1 h, Ar atmosphere | N,O-HPC-850 | 2520 | 0.80 | 435 | 0.1 | 1.0 M Na₂SO₄  /  6.0 M KOH | 23.2  /  – | 500  /  – | 10,000 (92.2%)  /  – | He et al. (2017) |
| Kraft lignin | Pyrolysis: 900 °C, 1 h, 4 °C min⁻¹, N₂ atmosphere | – | O-N-S-HPC | 1307 | 0.45 | 244.5 | 0.2 | 1.0 M Na₂SO₄  /  6.0 M KOH  /  EMIM BF₄ | 30.3  /  8.5  /  66.8 | 341  /  100  /  1750 | 20,000 (97.5%)  /  10,000 (91.6%)  /  10,000 (88.5%) | Liu et al. (2019b) |

**Fig. 26** Biochar's adsorption mechanism for eliminating nutrients, metals, and organic contaminants from wastewater (Yang et al. 2020b), Copyright © 2020, Elsevier

the fertilizer plant. The results of their investigation indicated a substantial reduction in phosphate concentration from 1660.0 to 0.06 mg L$^{-1}$ after 48 h of the treatment process, achieving an impressive 99.9% removal rate of phosphate from the industrial wastewater. Notably, the adsorption capacity of ZFCO-BC was found to be 70 times greater than that of pristine biochar. Additionally, ZFCO-BC displayed a remarkable synergistic effect by simultaneously removing 21 different metals, including but not limited to Cr, As, Cu, Pb, Co, and Cd, from the industrial wastewater. These findings underscore the significant potential of modified biochar in effectively eliminating both nutrients and heavy metals from contaminated water sources. In another study conducted by Khan et al. (2023b), algal-derived biochar was synthesized to target the removal of Cr(VI) from textile wastewater. Impressively, this algal-derived biochar demonstrated an exceptional adsorption capacity of 187 mg g$^{-1}$, along with a remarkable removal efficiency of 97.84% within a 240 min treatment process. Ye et al. (2022) developed two potential biochar adsorbents, CM6 derived from cattle manure and CW6 derived from cherry wood, to effectively remove heavy metals from industrial wastewater. CM6 demonstrated superior adsorption capacities, reaching 40.8 mg g$^{-1}$ for Pb$^{2+}$, 24.2 mg g$^{-1}$ for Cd$^{2+}$, and 25.1 mg g$^{-1}$ for Ni$^{2+}$. In contrast, CW6 exhibited slightly lower adsorption capacities for these heavy metals,

specifically 29.7 mg g$^{-1}$ for Pb$^{2+}$, 21.1 mg g$^{-1}$ for Cd$^{2+}$, and 14.7 mg g$^{-1}$ for Ni$^{2+}$. For a comprehensive overview of the adsorption performance of various biochar materials in removing heavy metals, nutrients, and organic contaminants from wastewater, please refer to Table 11.

In recent years, there has been a notable surge in interest regarding the utilization of biochar as a heterogeneous catalyst in advanced oxidation processes (AOPs) for wastewater treatment. AOPs leverage the generation of highly reactive oxygen species, such as hydroxyl radicals ($\cdot$OH) and sulfate radicals (SO$_4$$\cdot^-$), to efficiently degrade a variety of pollutants in wastewater, including pesticides, organic dyes, pharmaceuticals, and industrial chemicals (Zhu et al. 2023a). The surface of biochar can be modified or functionalized to enhance its catalytic activity within AOPs. Incorporating metal nanoparticles (e.g., Fe, Co, Mn, Cu) onto the biochar surface creates active sites that facilitate the production of free radicals (Zheng et al. 2023). The porous structure of biochar can adsorb pollutants onto its surface, and simultaneously, the active catalytic sites on biochar can promote the degradation of pollutants through advanced oxidation reactions. This dual functionality, integrating catalytic activity and adsorption capacity, renders biochar a versatile material for effective wastewater treatment (Lu et al. 2022). Various AOPs are employed for the degradation of emerging pollutants in wastewater treatment, including persulfate

**Table 11** Removal of heavy metals, nutrients, and organic contaminants from wastewater using biochar adsorbents with a focus on water resource recovery

| Biomass | Pyrolysis conditions | Activator | Wastewater source | Recovered substance | Adsorption capacity (mg $g^{-1}$) | References |
|---|---|---|---|---|---|---|
| Heavy metal removal | | | | | | |
| Marine algae | 500 °C, 1 h | – | Textile industry wastewater | Cr(VI) | 186.9 | Khan et al. (2023b) |
| Cattle manure | 600 °C, 1 h | – | Industrial wastewater | Pb(II) | 40.8 | Ye et al. (2022) |
| | | | | Cd(II) | 24.2 | |
| | | | | Ni(II) | 25.1 | |
| Cherry wood | 600 °C, 1 h | – | Industrial wastewater | Pb(II) | 29.7 | |
| | | | | Cd(II) | 21.1 | |
| | | | | Ni(II) | 14.7 | |
| Camel bones | 500 °C, 2 h | $FeCl_3$ | $Pb(NO_3)_2$ aqueous solution | Pb(II) | 244.8 | Alqadami et al. (2018) |
| | | | $Cd(NO_3)_2$ aqueous solution | Cd(II) | 322.6 | |
| | | | $Co(NO_3)_2$ aqueous solution | Co(II) | 294 | |
| Tea branches | 500 °C, 1.5 h | $MnFe_2O_4$ | $KSbC_4H_4O_7$ aqueous solution | Sb(III) | 237.5 | Wang et al. (2018b) |
| | | | $Cd(NO_3)_2$ aqueous solution | Cd(II) | 181.5 | |
| Bamboo | 480 °C, 2 h | Mg/Al-LDHs | $K_2Cr_2O_7$ aqueous solution | Cr(VI) | 38 | Huang et al. (2019) |
| Poplar leaves | 650 °C | $NH_2CONH_2$ | $K_2Cr_2O_7$ aqueous solution | Cr(VI) | 28.3 | Zhao et al. (2021) |
| Raw corncobs | 550 °C | $TiO_2$ | $Cd(NO_3)_2$ aqueous solution | Cd(II) | 72.6 | Luo et al. (2019) |
| | | | $NaH_2AsO_4$ aqueous solution | Ar(V) | 118.1 | |
| Douglas fir | 1000 °C, 10 s | $FeCl_3$ and $FeSO_4$ | $Pb(NO_3)_2$ aqueous solution | Pb(II) | 40 | Karunanayake et al. (2018) |
| | | | $Cd(NO_3)_2$ aqueous solution | Cd(II) | 16 | |
| Mangosteen shells | 700 °C, 1.5 h | HCl, KOH, and $ZnCl_2$ | $K_2Cr_2O_7$ aqueous solution | Cr(VI) | 212.6 | Shan et al. (2020) |
| Bamboo shoot shell | 550 °C, 3 h | $Zn(CH_3CO_2)_2$ and $HNO_3$ | $KReO_4$ aqueous solution | Re(VII) | 24.5 | Hu et al. (2019) |
| Corn stalk | 500 °C, 2 h | $FeCl_3$ | Wastewater | Cd(II) | 148.5 | Yang et al. (2020a) |
| | | | | As(III) | 33.8 | |
| Nutrient recovery | | | | | | |
| Corn straw | 550 °C, 1 h | $MgCl_2$ | Swine wastewater | N | 33.2 | Yu et al. (2020a) |
| | | | | P | 3.2 | |
| Rice husks | 450 °C, 2 h | $MgCl_2$ | $NH_4Cl$ aqueous solution | N | 58.2 | Jing et al. (2019) |
| | | | $KH_2PO_4$ aqueous solution | P | 125.4 | |
| Corncob | 600 °C, 10 h | – | Anaerobic digestate | P | 6.4 | Kizito et al. (2017) |
| Rice husk | | | | | 5.7 | |
| Sawdust | | | | | 5.4 | |
| *P. edulis* | 400 °C, 1 h | $MgCl_2$ | $KH_2PO_4$ aqueous solution | P | 344 | Jiang et al. (2018) |
| | 500 °C, 1 h | | | | 357 | |

**Table 11** (continued)

| Biomass | Pyrolysis conditions | Activator | Wastewater source | Recovered substance | Adsorption capacity (mg g$^{-1}$) | References |
|---|---|---|---|---|---|---|
| | 600 °C, 1 h | | | | 370 | |
| Corncob | 600 °C, 3 h | $MgCl_2$ | Swine wastewater | P | 239 | Fang et al. (2014) |
| Bamboo | 900 °C, 2 h | $FeCl_3$ and $CaCO_3$ | Industrial wastewater | P | 28.2 | Ou et al. (2023) |
| Corncob | 400 °C, 1 h | $HNO_3$ | $NH_4Cl$ aqueous solution | N | 22.6 | Vu et al. (2017) |
| Sugarcane residue | 550 °C, 1 h | $MgCl_2$ | Swine wastewater | N | 22 | Li et al. (2017) |
| | | | | P | 398 | |
| *E. crassipes* | 450 °C, 2 h | – | $KH_2PO_4$ aqueous solution | P | 31.6 | Mosa et al. (2018) |
| Sugarcane residue | 550 °C, 1 h | $MgCl_2$ | $KH_2PO_4$ aqueous solution | P | 121.3 | Li et al. (2016b) |
| Grapevine canes | 700 °C, 1 h | – | $KH_2PO_4$ aqueous solution | P | 37.7 | Marshall et al. (2017) |
| Sugarcane leaves | 500 °C, 1 h | Mg/Al-LDHs | $KH_2PO_4$ aqueous solution | P | 81.8 | Li et al. (2016a) |
| Cypress sawdust | 600 °C, 1 h | $MgCl_2$ | $KH_2PO_4$ aqueous solution | P | 66.7 | Haddad et al. (2018) |
| Organic contaminant removal | | | | | | |
| Sugarcane residue | 550 °C, 1 h | $MgCl_2$ | Swine wastewater | Humic acid | 247 | Li et al. (2017) |
| Wood waste | 700 °C, 15 h | $H_2SO_4$ | Stormwater | *E. coli* | – | Lau et al. (2017) |
| Pulp and paper sludge | 750 °C, 2 h | $FeCl_3$ | Methyl orange solution | Methyl orange | 46.6 | Chaukura et al. (2017) |
| Rice husks | 450 °C, 2 h | $MgCl_2$ | Humic acid solution | Humic acid | 34.6 | Jing et al. (2019) |
| Wastewater sludge | 500 °C, 2 h | $FeSO_4$ | Tetracycline solution | Tetracycline | 174.1 | Ma et al. (2020) |
| Wood dust | 500 °C, 6 h | – | Stormwater | Bisphenol A | – | Lu and Chen (2018) |

(PS) activation, peroxymonosulfate (PMS) activation, Fenton and Fenton-like processes, ozonation, photocatalysis, electrocatalysis, and sonocatalysis (Zou et al. 2023). Notably, persulfate (PS) and peroxymonosulfate (PMS) stand out as powerful oxidizing agents that can be activated using biochar-based catalysts to produce sulfate radicals ($SO_4\bullet^-$), highly reactive species capable of oxidizing a broad spectrum of pollutants (Huang et al. 2023a). Sulfate radicals ($SO_4\bullet^-$) and hydroxyl radicals ($\bullet OH$) attack pollutants through mechanisms like hydrogen abstraction, electron transfer, and direct addition reactions. As a result, complex contaminants are broken down into simpler, less harmful byproducts. For instance, Zhu et al. (2020) developed a highly efficient biochar-based catalyst, designated as Fe@NCNT-BC-800, from soybean dregs to activate persulfate (PS) in the degradation of Rhodamine B (RhB). Under optimal conditions of [RhB] = 20 mg L$^{-1}$, [Fe@NCNT-BC-800] = 1.0 g L$^{-1}$, [PS] = 5 mM, and pH = 7.0, the degradation of RhB was remarkably swift, achieving 100% removal within 10 min.

The efficacy of the Fe@NCNT-BC-800 catalyst extended to higher pH levels of 9.0 and 11.0, with 98% of RhB removed within 15 min. Notably, the Fe@NCNT-BC-800 catalyst demonstrated outstanding reusability by removing 90.56% of RhB even after undergoing 5 cycles. This research underscores the significant potential of biochar as a sustainable and efficient catalytic material for the degradation of persistent organic pollutants, making it a promising candidate for practical applications in wastewater treatment processes. Detailed insights into the efficacy of biochar-based catalysts in AOPs for the removal of emerging pollutants in wastewater are provided in Table 12.

Biochar, in addition to its role in water resource recovery, serves as an effective means to recover metals, nutrients, and energy from organic solid waste that would otherwise be destined for landfills (Samuel Olugbenga et al. 2024). It embodies the principles of a circular economy by transforming waste into valuable resources. Biochar enriched with heavy metals, like Pb, Hg, As, Cd,

**Table 12** The performances of biochar-based catalysts in advanced oxidation processes (AOPs) for the degradation of emerging pollutants in wastewater

| Bio-sources | Pyrolysis conditions | Modification agents | Catalysts | AOPs | Pollutants | Reaction conditions | Degradation efficiency (%) | References |
|---|---|---|---|---|---|---|---|---|
| Degradation of pharmaceuticals | | | | | | | | |
| Spent coffee ground | 700 °C, 10 °C min$^{-1}$, 120 min | NaOH and CoCl$_2$ | Co-SCG | PMS activation | Tetracycline (TC) | [TC]=0.2 mM, [Catalyst]=0.1 g L$^{-1}$, [PMS]=0.6 mM, t=25 min, pH=7 | 97 | Nguyen et al. (2019) |
| Rice straw | 450 °C | Co(NO$_3$)$_2$ and NH$_3$ | BC-Co$_3$O$_4$ | PMS activation | Ofloxacin (OFX) | [OFX]=50 µM, [Catalyst]=0.2 g L$^{-1}$, [PMS]=0.5 mM, t=10 min, pH=7, T=25 °C | 90 | Chen et al. (2018) |
| Maize cob | 600 °C, 120 min | FeSO$_4$ | Fe/C | PMS activation | Sulfapyridine (SPY) | [SPY]=10 mg L$^{-1}$, [Catalyst]=0.5 g L$^{-1}$, [PMS]=1 mM, t=30 min, pH=8.2, T=22 °C | 100 | Li et al. (2020d) |
| *Myriophyllum aquaticum* | 700 °C, 5 °C min$^{-1}$, 120 min | K$_2$FeO$_4$ | Fe$_3$O$_4$/MC700 | PMS activation | Ciprofloxacin (Cipro) | [Cipro]=20 mg L$^{-1}$, [Catalyst]=0.2 g L$^{-1}$, [PMS]=1 g L$^{-1}$, t=80 min, T=25 °C | 100 | Fu et al. (2019) |
| Organic dyes removal | | | | | | | | |
| *Spartina alterniflora* | 800 °C, 5 °C min$^{-1}$, 120 min | Zn(CH$_3$CO$_2$)$_2$ and K$_2$FeO$_4$ | ZnO-Fe@SC | Photocatalysis | Malachite green (MG) | [MG]=200 mg L$^{-1}$, [Catalyst]=0.05 g L$^{-1}$, t=60 min, UV light irradiation | 99.1 | Jing et al. (2023) |
| Food waste | 300 °C, 5 °C min$^{-1}$, 420 min | FeCl$_2$ and FeCl$_3$ | MC | Sono-Fenton-like | Methyl orange (MO) | [MO]=50 mg L$^{-1}$, [Catalyst]=2 g L$^{-1}$, [H$_2$O$_2$]=200 mM, t=180 min, Ultrasonic power=35.3W | 100 | Chu et al. (2020) |
| *Myriophyllum aquaticum* | 700 °C, 5 °C min$^{-1}$, 120 min | K$_2$FeO$_4$ | Fe$_3$O$_4$/MC700 | PMS activation | Orange II (OII) | [OII]=50 mg L$^{-1}$, [Catalyst]=0.2 g L$^{-1}$, [PMS]=1 g L$^{-1}$, t=40 min, T=25 °C | 100 | Fu et al. (2019) |
| | | | | | Tartrazine | [Tartrazine]=50 mg L$^{-1}$, [Catalyst]=0.2 g L$^{-1}$, [PMS]=1 g L$^{-1}$, t=100 min, T=25 °C | 95 | Fu et al. (2019) |
| Bamboo stakes | 600 °C, 10 °C min$^{-1}$, 120 min | ZnO | ZnO/biochar | Photocatalysis | Methylene blue (MB) | [MB]=160 mg L$^{-1}$, [Catalyst]=1 g L$^{-1}$, t=225 min, LED light power=250W | 95.2 | Yu et al. (2021) |

**Table 12** (continued)

| Bio-sources | Pyrolysis conditions | Modification agents | Catalysts | AOPs | Pollutants | Reaction conditions | Degradation efficiency (%) | References |
|---|---|---|---|---|---|---|---|---|
| Black liquor and Fenton sludge | 900 °C, 10 °C min⁻¹, 60 min | KOH | nZVI@biochar | Fenton-like | Rhodamine B (RhB) | [RhB]=50 mg L⁻¹, [Catalyst]=0.2 g L⁻¹, [H₂O₂]=2 mM, t=10 min, pH=3, T=30 °C | 100 | Xia et al. (2022b) |
| Soybean dregs | 800 °C, 2 °C min⁻¹, 60 min | C₂H₄N₄ and FeCl₃ | Fe@NCNT-BC-800 | PS activation | Rhodamine B (RhB) | [RhB]=20 mg L⁻¹, [Catalyst]=1 g L⁻¹, [PS]=5 mM, t=10 min, pH=7 | 100 | Zhu et al. (2020) |
| Pesticide degradation | | | | | | | | |
| Giant reed | 850 °C, 5 °C min⁻¹, 120 min | C₄H₆CoO₄ | Co-S@NC | PMS activation | Dinotefuran (DIN) | [DIN]=10 mg L⁻¹, [Catalyst]=0.1 g L⁻¹, [PMS]=0.65 mM, t=90 min, pH=4.8 | 100 | Du et al. (2020) |
| Rice straw | 800 °C, 5 °C min⁻¹, 240 min | Co(NO₃)₂ and FeSO₄ | MNBC₈₀₀ | PMS activation | Metolachlor (MET) | [MET]=10 mg L⁻¹, [Catalyst]=0.2 g L⁻¹, [PMS]=0.5 mM, t=40 min | 100 | Liu et al. (2019a) |
| Degradation of endocrine disruptors | | | | | | | | |
| Sawdust | 700 °C, 60 min | FeCl₃ | Fe-BC-700 | PMS activation | Bisphenol A (BPA) | [BPA]=20 mg L⁻¹, [Catalyst]=0.15 g L⁻¹, [PMS]=0.2 g L⁻¹, t=5 min, pH=8.2 | 100 | Jiang et al. (2019a) |
| *Candida utilis* | 700 °C, 5 °C min⁻¹, 120 min | NaCl and KCl | NCS-6 | PMS activation | Bisphenol A (BPA) | [BPA]=20 mg L⁻¹, [Catalyst]=0.4 g L⁻¹, [PMS]=0.4 g L⁻¹, t=6 min, pH=7, T=25 °C | 100 | Xie et al. (2020) |
| Corn straws | 400 °C, 5 °C min⁻¹, 120 min | Co(NO₃)₂ and Fe(NO₃)₃ | CoFe₂O₄/HPC | PMS activation | Bisphenol A (BPA) | [BPA]=10 mg L⁻¹, [Catalyst]=0.05 g L⁻¹, [PMS]=0.5 g L⁻¹, t=8 min, pH=7.4, T=25 °C | 100 | Li et al. (2020c) |
| Spent coffee ground | 1000 °C, 10 °C min⁻¹, 60 min | CO(NH₂)₂ | NBC-1000 | PMS activation | Bisphenol A (BPA) | [BPA]=5 mg L⁻¹, [Catalyst]=0.2 g L⁻¹, [PMS]=0.3 g L⁻¹, t=60 min, pH=4 | 99 | Oh et al. (2018) |

**Table 12** (continued)

| Bio-sources | Pyrolysis conditions | Modification agents | Catalysts | AOPs | Pollutants | Reaction conditions | Degradation efficiency (%) | References |
|---|---|---|---|---|---|---|---|---|
| *Myriophyllum aquaticum* | 700 °C, 5 °C min$^{-1}$, 120 min | $K_2FeO_4$ | $Fe_3O_4$/MC700 | PMS activation | Bisphenol A (BPA) | [BPA] = 10 mg L$^{-1}$, [Catalyst] = 0.2 g L$^{-1}$, [PMS] = 1 g L$^{-1}$, t = 100 min, T = 25 °C | 98 | Fu et al. (2019) |
| Emerging pollutants removal | | | | | | | | |
| Wheat flour | 700 °C, 5 °C min$^{-1}$, 120 min | $Co(NO_3)_2$ | Co–N–S-PC 700 | PMS activation | p-hydroxybenzoic acid (HBA) | [HBA] = 20 mg L$^{-1}$, [Catalyst] = 0.066 g L$^{-1}$, [PMS] = 6.5 mM, t = 120 min, T = 25 °C | 98 | Tian et al. (2018) |
| *Myriophyllum aquaticum* | 700 °C, 5 °C min$^{-1}$, 120 min | $K_2FeO_4$ | $Fe_3O_4$/MC700 | PMS activation | p-hydroxybenzoic acid (HBA) | [HBA] = 10 mg L$^{-1}$, [Catalyst] = 0.2 g L$^{-1}$, [PMS] = 1 g L$^{-1}$, t = 30 min, T = 25 °C | 100 | Fu et al. (2019) |

and Cr adsorbed from wastewater treatment, may potentially be categorized as hazardous waste due to the risk of releasing heavy metals as secondary pollutants, thus posing an environmental concern. Once saturated with metals, this biochar can undergo metal recovery processes, such as acid leaching, to extract valuable metals for reuse in various applications (Yu et al. 2019). Metal-enriched biochar can undergo further processing, such as microwave treatment or pyrolysis, to produce highly promising catalysts or electrode materials for fuel cells, batteries, and supercapacitors (Qin et al. 2019). During the reprocessing procedure, biochar and the reclaimed metals synergistically collaborate, enhancing biochar's catalytic capabilities through the incorporation of these metals into the carbon matrix. The ongoing shortage of nutrients, notably the deficit of P, poses a significant challenge for government bodies (Reijnders 2014). Therefore, there is an urgent imperative to accelerate technological advancements for nutrient retrieval from wastewater. Biochar has the capability to recover nutrients, including N and P, from wastewater. This nutrient-enriched biochar can then be used as a slow-release fertilizer in agriculture, mitigating the reliance on synthetic fertilizers and promoting sustainable nutrient cycling (El-Naggar et al. 2019). Alternatively, it can undergo further processing to extract nutrients for potential applications (Yang et al. 2020b). The most straightforward approach to harnessing energy from wastewater is by converting sludge into biogas through anaerobic digestion (AD). Biochar plays a crucial role in enhancing the efficiency of the digestion process by providing a habitat for bacteria and microorganisms that expedite the decomposition of solid organic waste and the subsequent production of biomethane (Yang et al. 2020b).

### 5.5 $CO_2$ capture and reduction

Addressing the ongoing concerns about GHG emissions and their detrimental impact on climate change is of paramount importance. Capturing $CO_2$ emissions plays a pivotal role in mitigating the greenhouse effect and addressing the broader issue of global warming. Biochar has garnered significant attention for its potential applications in carbon capture and reduction. It can capture $CO_2$ from various sources, including industrial emissions, power plants, or directly from the atmosphere (Khan et al. 2023e). The porous structure of biochar provides a large surface area, which is ideal for adsorbing $CO_2$. The captured $CO_2$ can be subsequently released through desorption, making it suitable for various applications, including conversion into value-added products such as fuels and chemicals through electrochemical reduction technology (Fang et al. 2023).

Several key factors contribute to enhancing the $CO_2$ adsorption capability of biochar materials. These factors include their high surface area, microporous structures, and O-containing functional groups (e.g., –OH, –COOH, and C=O). However, it's worth noting that biochar's $CO_2$ adsorption capacity can diminish in humid environments due to its strong attraction to water. Biochar with hydrophobic and non-polar characteristics may enhance $CO_2$ adsorption capacity by minimizing interference from water molecules (Sarwar et al. 2021). The adsorption of $CO_2$ on biochar materials can occur through either physical or chemical pathways, with the specific mechanism predominantly relying on the textural characteristics and surface functionality of the material. In the case of pristine biochar, the primary mechanism for $CO_2$ adsorption is physisorption, mainly governed by van der Waals forces. This underscores the vital importance of the biochar's structural characteristics in the process of capturing $CO_2$. In functionalized biochar, the adsorption of $CO_2$ might involve a combination of physisorption and chemisorption due to the presence of chemical functional groups on the surface. Surface chemistry is vital in creating additional active sites for $CO_2$ capture, primarily through chemisorption, which involves strong bonding between $CO_2$ and the biochar surface, such as Lewis acid–base interactions (Yuan et al. 2022).

For instance, Zhang et al. (2022) conducted a synthesis of biochar using corn stalk and soybean straw biomass via pyrolysis, and subsequently impregnated it with lignin to fine-tune the pore structure, as shown in Fig. 27a. Following the lignin treatment, the SSA and TPV of the biochar material significantly increased, reaching a maximum of 258 $m^2$ $g^{-1}$ and 0.18 $cm^3$ $g^{-1}$, respectively. The lignin-treated biochar exhibited an enhanced $CO_2$ adsorption capacity ranging from 77.02 to 102.88 mg $g^{-1}$, surpassing the raw biochar (with an adsorption capacity of 74.18 to 89.75 mg $g^{-1}$) due to its super micropore structure and high surface area. Notably, the lignin-treated biochar also demonstrated a notable capacity for adsorbing volatile organic compounds (VOCs) such as benzene (ranging from 31.35 to 61.14 mg $g^{-1}$) and acetone (ranging from 44.67 to 80.99 mg $g^{-1}$).

Figure 27b illustrates the application of biochar to capture $CO_2$ from the environment and sequestrate carbon. Besides physically adsorbing $CO_2$, the introduction of heteroatoms (N and S) and metals (Mg, Al, and Fe) has the potential to enhance the chemical bonding (chemisorption) of $CO_2$, which significantly improves $CO_2$ adsorption capacity and selectivity over other gases (Yuan et al. 2022). Alkali and alkaline earth metals, like Na, K, Ca, Mg, and Li, facilitate the creation of basic sites with a robust attraction to $CO_2$ molecules, functioning
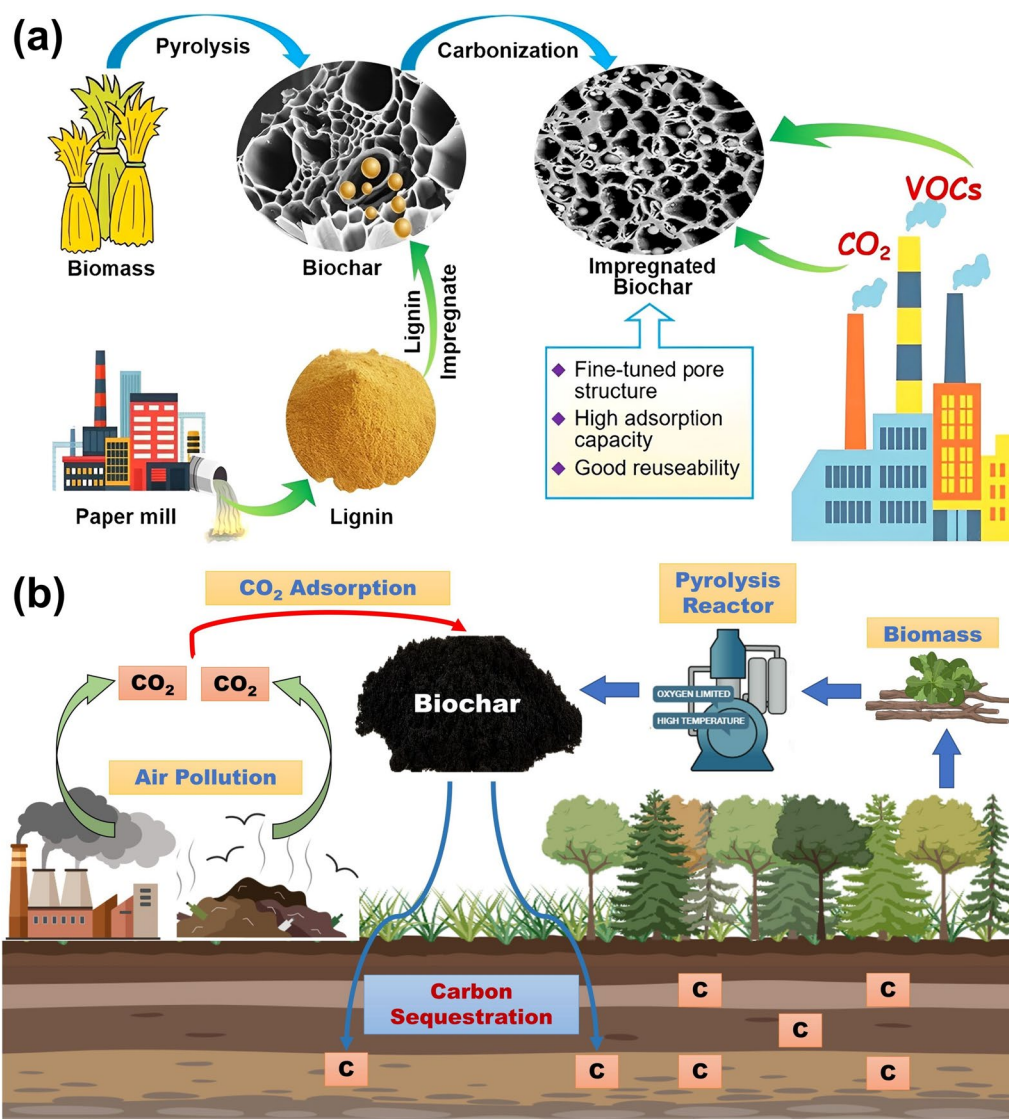
**Fig. 27** **a** Lignin-impregnated biochar for $CO_2$ and VOCs capture (Zhang et al. 2022), Copyright © 2022, Elsevier. **b** Biochar application in $CO_2$ adsorption and carbon sequestration (Khan et al. 2023e), Copyright© 2023, Elsevier

as Lewis acids (Ahmad et al. 2017). For instance, Lahijani et al. (2018) introduced different metals (Mg, Al, Fe, Ni, Ca, and Na) into the biochar framework to enhance its $CO_2$ capture capacity. Among these, Mg-BC exhibited the highest $CO_2$ adsorption capacity, reaching 82 mg g$^{-1}$, which was 16% higher than that of pristine biochar (72.6 mg g$^{-1}$) under ambient conditions at 25 °C and 1 atm. The incorporation of metals into the biochar matrix improved $CO_2$ adsorption capacity in the following order: Mg-BC > Al-BC > Fe-BC > Ni-BC > Ca-BC > Na-BC.

Beyond their role in $CO_2$ capture and storage, biochar materials have garnered significant attention as potential catalysts for the $CO_2$ reduction reaction ($CO_2$RR)

(Feng et al. 2023). The $CO_2$RR is an electrochemical process that converts $CO_2$ into valuable fuels and chemicals, such as CO, $CH_4$, $C_2H_4$, and $CH_3OH$, often making use of renewable energy sources. This process holds immense potential for mitigating climate change by simultaneously reducing $CO_2$ emissions and generating useful commodities. Biochar can serve various roles in $CO_2$RR, primarily as catalyst support, thanks to its large surface area, excellent electrical conductivity, presence of O-containing functional groups (e.g., –OH, –COOH, and C=O), and high electrochemical stability (Nielsen et al. 2018). By incorporating active metals into the biochar matrix, it is possible to enhance its $CO_2$RR activity and selectivity for specific target products. Notably, N-doped biochar
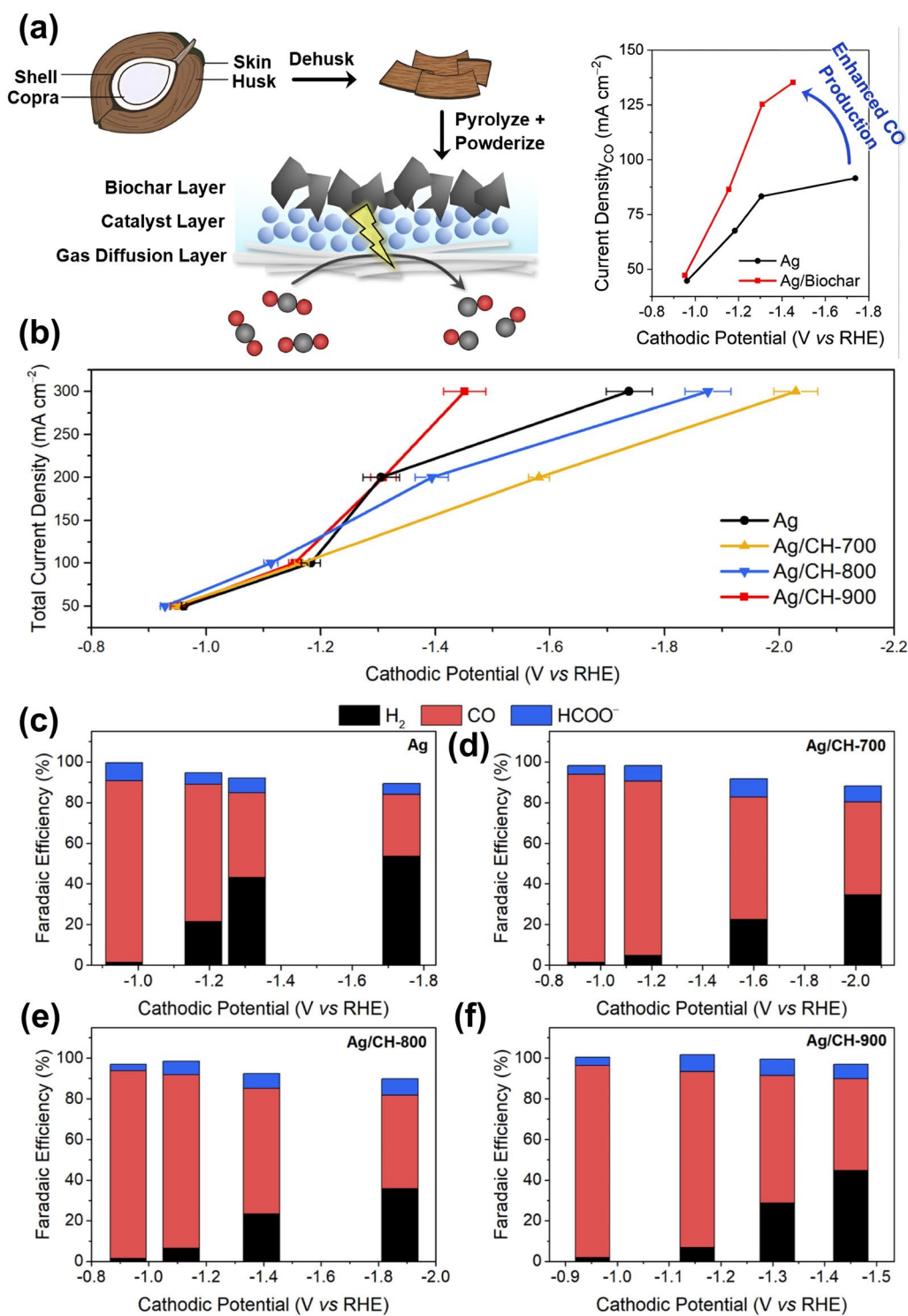
**Fig. 28** **a** Fabrication of biochar-layered gas diffusion electrodes (GDEs) for CO$_2$RR; **b** Comparison of total current density as a function of cathodic potential for different GDEs; Faradaic efficiency profiles for (**c**) Ag, (**d**) Ag/CH-700, **e** Ag/CH-800, and (**f**) Ag/CH-900 GDEs (Tan et al. 2023), Copyright © 2023, Elsevier

materials are emerging as promising $CO_2RR$ catalysts, offering high electronegativity and effectively tuning the electronic structure of the carbon framework (Norouzi et al. 2020).

In a recent study conducted by Tan et al. (2023), biochar-based catalytic materials were developed, denoted as Ag/CH-700, Ag/CH-800, and Ag/CH-900, using coconut husk biomass for the electrochemical conversion of $CO_2$ into value-added products such as CO, $H_2$, and $HCOO^-$. To enhance CO production within a flow electrolyzer, a layer of coconut husk-derived biochar was introduced onto an Ag-coated PTFE substrate, as shown in Fig. 28a. The Ag/CH-900 electrode demonstrated the most favorable cathodic potential, enabling a high current density of 300 mA cm$^{-2}$, as illustrated in Fig. 28b. When analyzing the product distribution, including CO, $H_2$, and $HCOO^-$, it was observed that the Ag electrode exhibited a high Faradaic efficiency (FE) for CO production at a low cathodic potential, achieving 89.3%. However, as the cathodic potential increased, the FE shifted towards the undesired product, $H_2$, as depicted in Fig. 28c. In contrast, all the biochar-based electrodes (Ag/CH-700, Ag/CH-800, and Ag/CH-900) consistently displayed higher FEs for CO production across various cathodic potentials, as shown in Fig. 28d–f. Among these electrodes, Ag/CH-900 achieved the highest FE for CO ($FE_{CO}$), reaching 94.4% at 50 mA cm$^{-2}$ and 86.5%

at 100 mA cm$^{-2}$. In another study, Gong et al. (2021) developed carbon aerogels containing Cu nanoparticles, referred to as SF-Cu/CA and SF-Cu/CA-1, using silk fibroin as a biomass precursor. These aerogels were designed for the electrocatalytic conversion of $CO_2$ into value-added CO. The SF-Cu/CA-1 catalyst exhibited exceptional $CO_2RR$ performance, achieving a current density of 29.4 mA cm$^{-2}$, a high $FE_{CO}$ of 83.1%, and a favorable CO/$H_2$ ratio of 19.6. This superior performance can be mainly attributed to the abundant active sites, rapid electron transfer rate, and the easy desorption of *CO within the SF-Cu/CA-1 catalyst. In contrast, the SF-Cu/CA catalyst showed a reduced current density of 13.0 mA cm$^{-2}$, a lower $FE_{CO}$ of 58.4%, and a decreased CO/$H_2$ ratio of 2.2.

### 5.6 Soil amelioration

Driven by the need for sustainable agriculture, the use of biochar in soil amelioration has grown rapidly due to its potential to improve soil quality and reduce reliance on synthetic fertilizers (Lu et al. 2023). The incorporation of biochar into the soil contributes to increased soil organic matter content, enhanced soil structure, improved microbial activity, and superior nutrient and water retention (Fig. 29), all of which are conductive to optimal plant growth and high crop yields (Yang et al. 2023d). The beneficial impacts of introducing biochar into the soil can
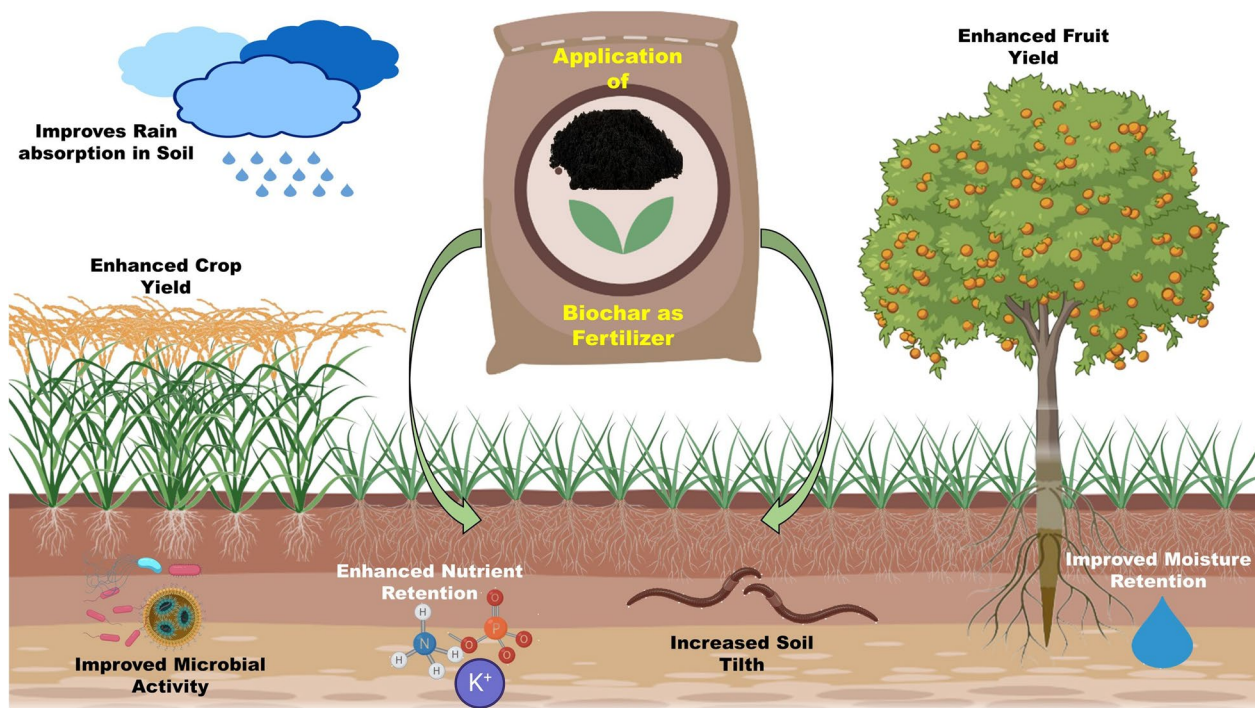
**Fig. 29** Impact of biochar application on soil amelioration (Khan et al. 2023e), Copyright © 2023, Elsevier

be primarily attributed to its substantial surface area, porosity, and cation exchange capacity, facilitating the enhancement of soil properties and fostering a more sustainable environment (Ouyang et al. 2023).

Biochar plays a pivotal role in enhancing soil structure by advancing the formation of stable aggregates. This, in turn, encourages better water infiltration, root penetration, and overall soil aeration (Bo et al. 2023). A well-structured soil is crucial for promoting healthy plant growth as it facilitates the movement of air, water, and nutrients through the soil. The porous nature of biochar allows for efficient water absorption and retention, enhancing the soil's water-holding capacity. This attribute proves particularly beneficial in regions with limited water availability or during drought conditions, facilitating more effective water access for plants (Park et al. 2023a). Biochar can also help neutralize acidic soils, creating a more balanced pH environment for plant growth. With its high cation exchange capacity (CEC), biochar plays a crucial role in augmenting soil fertility by attracting and retaining positively charged ions such as potassium ($K^+$), calcium ($Ca^{2+}$), and magnesium ($Mg^{2+}$). This prevents nutrient leaching and ensures their sustained availability to plants over time (Ivanova et al. 2023).

Additionally, biochar serves as a habitat for beneficial microorganisms, including bacteria and fungi, which play pivotal roles in nutrient cycling, organic matter decomposition, soil respiration, and overall soil health. By fostering a diverse and active microbial community, biochar contributes to creating a more fertile and productive soil environment (Lei et al. 2023). Furthermore, biochar possesses the capability to adsorb and immobilize various contaminants and toxins, including heavy metals, pesticides, and other organic pollutants present in the soil (Fan et al. 2023). A recent study by Yang et al. (2023c) underscores that introducing biochar into polluted soils significantly reduces contaminant levels, enhancing soil quality and mitigating the risk of environmental damage.

In summary, the favorable impacts of biochar on soil tilth, water retention, nutrient availability, and microbial activity collectively contribute to improved plant growth and increased crop yields. However, it is imperative to ensure that the production and application of biochar adhere to stringent quality standards, with appropriate measures implemented to minimize potential risks related to soil and water contamination.

## 6 Technology readiness level (TRL) assessment

The technology readiness level (TRL) is a systematic framework used to assess the progress and maturity of a technology, product, or system for practical applications in real-world environments. TRLs are measured on a scale from 1 to 9, with 1 representing the most basic stage and 9 indicating full commercial viability. They are generally categorized into three key phases: (i) lab-scale (TRL 1–3), (ii) pilot-scale (TRL 4–6), and (iii) commercial scale (TRL 7–9) (Mahmood Ali et al. 2023). It's worth noting that the International Energy Agency (IEA) has proposed expanding the TRL scale to include two additional readiness levels: TRL 10, where the technology is commercial but requires further integration efforts, and TRL 11, where the technology has achieved predictable and sustainable growth (Incer-Valverde et al. 2023). The TRL framework assists policymakers, researchers, and funding agencies in comprehending the current state of technology and making informed decisions regarding further investment, research, or implementation strategies. It is a valuable tool for assessing the maturity and development stage of emerging technologies in various fields (Shyam et al. 2022).

Pyrolysis technology has reached a high level of maturity for the production of biochar, with numerous pilot and commercial plants operating worldwide (Chen et al. 2021). Notable countries with active facilities include the USA, Canada, Finland, China, Australia, France, Netherlands, and Greece, with processing capacities typically ranging from 200–8000 kg/h of biomass feedstock (Rex et al. 2023). According to a report by GECA Environment, there are 66 commercial pyrolysis units in the USA and Canada, with 37 of them having a significant production capacity of over 10,000 metric tons per year. In 2021, the production capacity for biochar reached 1,200,000 metric tons per year in the USA and 200,000 metric tons per year in Canada. By the end of 2023, it is anticipated that the biochar production capacity will increase to 1,500,000 metric tons per year in the USA and 1,400,000 metric tons per year in Canada. A notable exemplar is Oregon Biochar Solutions in the USA, which annually produces 3500–4000 metric tons of biochar, serving as a substitute for existing products like activated carbon for water filtration and various soil conditioners (Kharel et al. 2019). In Canada, several commercial units like Canadian AgriChar, Agri-Therm, and Pyrovac are actively employing pyrolysis technology with biomass processing capacities of up to 8000 kg $h^{-1}$ (Bridgwater 2012). Additionally, several research-oriented pyrolysis units are operational worldwide, including CIRAD in France, RTI in Canada, ECN in the Netherlands, CPERI in Greece, and GIEC in China (Al-Rumaihi et al. 2022). Industrial biochar production receives additional support and benefits from its affiliations with the International Biochar Initiative (IBI), the European Biochar Industry Consortium (EBI), and the Canadian Biochar Initiative (CBI) (Supraja et al. 2023). Collectively, these examples demonstrate that biomass pyrolysis technology has achieved full commercialization for biochar production, reaching a TRL of 9.

Hydrothermal carbonization (HTC) technology for hydrochar production has successfully been implemented at an industrial scale over the past 15 years, with multiple operational HTC plants across Europe, achieving a TRL of 8–9. For instance, Ingelia, a developer of HTC technology, has been running its own commercial HTC plant in Valencia, Spain since 2010, capable of processing 14,000 metric tons of various types of biomass annually (Fernández-Sanromán et al. 2021). In a noteworthy development, CPL Industries, in collaboration with Ingelia, established the first commercial-scale HTC unit in the UK in 2018. This innovative facility transforms a wide range of biomass waste, including food, clothing, and garden waste, into hydrochar, which can be utilized as a fuel source with a gross calorific value of 20–23 MJ kg$^{-1}$ (Cavali et al. 2023). More recently, Ingelia has extended its operations by establishing four additional HTC plants in Belgium, the Spanish Basque country, and Italy (Cavali et al. 2023). The successful deployment of Ingelia's HTC technology at a commercial scale exemplifies its advanced level of maturity, reaching TRL 9.

Hydrogen fuel cell technology based on biochar catalysts is an innovative and emerging concept that has shown promise at the laboratory scale but has yet to undergo extensive testing and demonstration at the pilot and commercial scales. As a result, the TRL for biochar-based fuel cell technology currently stands at 2–3 (Al-Rumaihi et al. 2022). The key obstacles that hinder the advancement of this emerging technology to higher TRL levels revolve around the need for improvements in the electrochemical activity and stability of biochar-based catalysts. Biochar-based electrode materials for supercapacitors are still in the early stages of development, with most of the research focused on the laboratory scale and the optimization of the synthesis and modification techniques. Therefore, the TRL of biochar for supercapacitors is identified as 3–4, indicating that the technology has been validated in the laboratory environment and has shown some potential for further development and scaling up (Shah et al. 2023). Biochar for wastewater treatment is an emerging technology that has been extensively studied in the laboratory and pilot scale, but it still requires further validation and demonstration in commercial-scale water treatment plants before it can be considered a reliable and competitive technology, resulting in a TRL of 5–7 (Supraja et al. 2023). In a significant development, Glanris, a prominent US climate-tech company founded in 2018, specializes in producing a versatile biochar known as Glanris Biocarbon®. Made from rice husks, this biocarbon filtration media excels in effectively removing a variety of metals, including Hg, Pb, Cr, Cu, and Zn, as well as a diverse range of organic contaminants such as pesticides, dyes, and pharmaceuticals from industrial wastewater, municipal water, and portable water sources. Glanris Biocarbon® not only combines the adsorbent properties of activated carbon but also boasts the metals removal capability of ion exchange resin, making it a sustainable and eco-friendly material at a more economical cost. Moreover, it is noteworthy that Glanris Biocarbon® proudly holds certification from IAPMO R&T under the NSF/ANSI/CAN 61 standard for wastewater treatment. Over the past two decades, significant advancements have been made in the development and implementation of biochar carbon removal technology on a commercial scale, achieving a TRL of 7–8. A standout example is PYREG GmbH, a leading German company established in 2009, specializing in the thermochemical conversion of organic wastes into $CO_2$-adsorbing biochar. PYREG has been at the forefront of carbon capture innovation, and their 50 operational plants worldwide collectively sequester an impressive 30,000 tons of $CO_2$ annually. The TRL of biochar as a soil amendment is on a swift ascent, reaching levels 7–8. Notably, several commercial biochar products have entered the market, marking a gradual uptick in their adoption within the agricultural sector. A noteworthy case is SoilFixer, a UK-based company established in 2016, specializing in manufacturing and marketing high-quality biochar granules, compost activators, and super compost (SF60), proven to enhance soil quality and boost plant growth by a significant margin, ranging from 20% to as much as 100%.

## 7 Knowledge gaps and recommendations

Functionalized biochar materials have demonstrated significant potential across various applications, such as water splitting, fuel cells, supercapacitors, wastewater treatment, $CO_2$ capture and reduction, and soil amelioration. However, there are still some knowledge gaps and challenges that require attention to enhance the performance and practical scalability of these materials across diverse fields. Some of them are:

(1) Biochar properties can vary widely depending on the biomass feedstock type, pyrolysis conditions, and post-treatment procedures. This variability hinders the standardization and optimization of biochar quality for specific applications. Therefore, there is a pressing need to establish guidelines and regulations for biochar production and quality standards.

(2) Systematic studies on the economic feasibility of biochar-based energy conversion technologies, including cost–benefit analyses and market assessments, are lacking and necessary.

(3) More research is needed to develop cost-effective and eco-friendly biochar functionalization techniques with the potential for easy scalability.

(4) While biochar materials show great promise for diverse applications, there is limited information on their potential unintended consequences, which need to be thoroughly explored.

(5) There is a lack of understanding regarding the mechanisms and interactions of functionalized biochar materials with reactant molecules, contaminants, and microorganisms. More in-depth and mechanistic research studies are necessary to unravel these complex relationships.

Future research directions should focus on:

(1) Assessing the environmental and economic feasibility of functionalized biochar materials through life cycle assessment (LCA) and techno-economic analysis (TEA).

(2) Facilitating the commercialization and industrialization of functionalized biochar materials by establishing partnerships, industry standards, regulations, and policies.

(3) Expanding the applications of functionalized biochar materials into diverse fields, including drug delivery, biosensors, 3D printing, and photocatalysis.

## 8 Conclusion

Functionalized biochar materials have emerged as promising candidates (e.g., catalysts, electrodes, and adsorbents) for various applications in the energy, water, and environment sectors. This review paper underscores their potential benefits and associated challenges concerning their synthesis, characterization, and performance. These biocarbon materials offer a sustainable and cost-effective way to produce and store renewable energy, treat wastewater, and mitigate carbon emissions. However, they also face some challenges in terms of quality optimization, scalability, and compatibility with different systems. Future research should focus on developing green functionalization techniques while evaluating their environmental and economic feasibility. By tackling these challenges, functionalized biochar materials can pave the way for a cleaner and more sustainable future.

**Abbreviations**

| | |
|---|---|
| GHG | Greenhouse gas |
| TRL | Technology readiness level |
| FC | Fixed carbon |
| VM | Volatile matter |
| HTC | Hydrothermal carbonization |
| MHTC | Microwave-assisted hydrothermal carbonization |
| HHV | Higher heating value |
| AC | Activated carbon |
| SSA | Specific surface area |
| TPV | Total pore volume |
| APD | Average pore diameter |
| AD | Anaerobic digestion |
| BMP | Biochemical methane potential |
| PAN | Polyacrylonitrile |
| CNTs | Carbon nanotubes |
| GNRs | Graphene nanoribbons |
| SEM | Scanning electron microscopy |
| TEM | Transmission electron microscopy |
| EDS | Energy-dispersive X-ray spectroscopy |
| XRD | X-ray diffraction |
| TGA | Thermogravimetric analysis |
| BET | Brunauer-Emmett-Teller |
| NLDFT | Non-local density functional theory |
| XPS | X-ray photoelectron spectroscopy |
| FTIR | Fourier-transform infrared spectroscopy |
| HER | Hydrogen evolution reaction |
| OER | Oxygen evolution reaction |
| EIS | Electrochemical impedance spectroscopy |
| ECSA | Electrochemical surface area |
| RHE | Reversible hydrogen electrode |
| CA | Chronoamperometry |
| HOR | Hydrogen oxidation reaction |
| ORR | Oxygen reduction reaction |
| PEM | Proton exchange membrane |
| LSV | Linear sweep voltammetry |
| CV | Cyclic voltammetry |
| MEA | Membrane electrode assembly |
| RDE | Rotating disk electrode |
| GCD | Galvanostatic charge–discharge |
| AOPs | Advanced oxidation processes |
| VOCs | Volatile organic compounds |
| $CO_2RR$ | Carbon dioxide reduction reaction |
| FE | Faradaic efficiency |
| GDE | Gas diffusion electrode |
| LCA | Life cycle assessment |
| TEA | Techno-economic analysis |

**Author contributions**
MZY: Investigation, Methodology, Formal analysis, Writing—original draft, Writing—review and editing; SRN: Conceptualization, Supervision, Project administration, Funding acquisition, Writing—review and editing; DJ: Data curation, Software, Writing—review and editing; MNAK: Validation, Writing—review and editing. All authors read and approved the final manuscript.

**Availability of data and materials**
The datasets used or analyzed during the current study are available from the corresponding author on reasonable request.

## Declarations

**Ethics approval and consent to participate**
Not applicable.

**Consent for publication**
Not applicable.

## Author details

[1]Laboratory of Alternative Fuels and Sustainability, School of Chemical and Materials Engineering (SCME), National University of Sciences and Technology (NUST), Sector H-12, Islamabad 44000, Pakistan. [2]Department of Electronics, Faculty of Electrical Engineering and Computer Science, VŠB-Technical University of Ostrava, 17. Listopadu 2172/15, 708 00 Ostrava, Poruba, Czech Republic. [3]Department of Engineering and Chemical Sciences, Karlstad University, Karlstad, Sweden.

## References

Abdoli MA, Ghasemzadeh R (2024) Evaluation and optimization of hydrothermal carbonization condition for hydrochar and methane yield from anaerobic digestion of organic fraction of municipal solid waste (OFMSW). Fuel 355:129531. https://doi.org/10.1016/j.fuel.2023.129531

Ahmad M, Lee SS, Lee SE, Al-Wabel MI, Tsang DCW, Ok YS (2017) Biochar-induced changes in soil properties affected immobilization/mobilization of metals/metalloids in contaminated soils. J Soils Sediments 17:717–730. https://doi.org/10.1007/s11368-015-1339-4

Aktar S, Hossain MA, Rathnayake N, Patel S, Gasco G, Mendez A, de Figueiredo C, Surapaneni A, Shah K, Paz-Ferreiro J (2022) Effects of temperature and carrier gas on physico-chemical properties of biochar derived from biosolids. J Anal Appl Pyrol 164:105542. https://doi.org/10.1016/j.jaap.2022.105542

AlMohamadi H, Alamoudi M, Yameen MZ, Naqvi SR (2023) An integrated approach for the extraction of lipids from marine macroalgae consortium using RSM optimization and thermo-kinetic analysis. Chemosphere 338:139623. https://doi.org/10.1016/j.chemosphere.2023.139623

Alqadami AA, Khan MA, Otero M, Siddiqui MR, Jeon B-H, Batoo KM (2018) A magnetic nanocomposite produced from camel bones for an efficient adsorption of toxic metals from water. J Clean Prod 178:293–304. https://doi.org/10.1016/j.jclepro.2018.01.023

Al-Rumaihi A, Shahbaz M, McKay G, Mackey H, Al-Ansari T (2022) A review of pyrolysis technologies and feedstock: a blending approach for plastic and biomass towards optimum biochar yield. Renew Sustain Energy Rev 167:112715. https://doi.org/10.1016/j.rser.2022.112715

Amalina F, Razak ASA, Krishnan S, Sulaiman H, Zularisam AW, Nasrullah M (2022) Biochar production techniques utilizing biomass waste-derived materials and environmental applications—a review. J Hazardous Mater Adv 7:100134. https://doi.org/10.1016/j.hazadv.2022.100134

Aria M, Cuccurullo C (2017) bibliometrix: an R-tool for comprehensive science mapping analysis. J Informet 11:959–975. https://doi.org/10.1016/j.joi.2017.08.007

Bo X, Zhang Z, Wang J, Guo S, Li Z, Lin H, Huang Y, Han Z, Kuzyakov Y, Zou J (2023) Benefits and limitations of biochar for climate-smart agriculture: a review and case study from China. Biochar 5:77. https://doi.org/10.1007/s42773-023-00279-x

Borghei M, Laocharoen N, Kibena-Põldsepp E, Johansson L-S, Campbell J, Kauppinen E, Tammeveski K, Rojas OJ (2017) Porous N, P-doped carbon from coconut shells with high electrocatalytic activity for oxygen reduction: alternative to Pt-C for alkaline fuel cells. Appl Catal B 204:394–402. https://doi.org/10.1016/j.apcatb.2016.11.029

Bridgwater AV (2012) Review of fast pyrolysis of biomass and product upgrading. Biomass Bioenerg 38:68–94. https://doi.org/10.1016/j.biombioe.2011.01.048

Cao B, Yuan J, Jiang D, Wang S, Barati B, Hu Y, Yuan C, Gong X, Wang Q (2021a) Seaweed-derived biochar with multiple active sites as a heterogeneous catalyst for converting macroalgae into acid-free biooil containing abundant ester and sugar substances. Fuel 285:119164. https://doi.org/10.1016/j.fuel.2020.119164

Cao M, Wang Q, Cheng W, Huan S, Hu Y, Niu Z, Han G, Cheng H, Wang G (2021b) A novel strategy combining electrospraying and one-step carbonization for the preparation of ultralight honeycomb-like multi-layered carbon from biomass-derived lignin. Carbon 179:68–79. https://doi.org/10.1016/j.carbon.2021.03.063

Castro-Gutiérrez J, Celzard A, Fierro V (2020) Energy storage in supercapacitors: focus on tannin-derived carbon electrodes. Front Mater 7:217. https://doi.org/10.3389/fmats.2020.00217

Cavali M, Libardi Junior N, de Sena JD, Woiciechowski AL, Soccol CR, Belli Filho P, Bayard R, Benbelkacem H, de Castilhos Junior AB (2023) A review on hydrothermal carbonization of potential biomass wastes, characterization and environmental applications of hydrochar, and biorefinery perspectives of the process. Sci Total Environ 857:159627. https://doi.org/10.1016/j.scitotenv.2022.159627

Chang B, Shi W, Yin H, Zhang S, Yang B (2019a) Poplar catkin-derived self-templated synthesis of N-doped hierarchical porous carbon microtubes for effective $CO_2$ capture. Chem Eng J 358:1507–1518. https://doi.org/10.1016/j.cej.2018.10.142

Chang C, Li M, Wang H, Wang S, Liu X, Liu H, Li L (2019b) A novel fabrication strategy for doped hierarchical porous biomass-derived carbon with high microporosity for ultrahigh-capacitance supercapacitors. J Mater Chem A 7:19939–19949. https://doi.org/10.1039/C9TA06210F

Chaukura N, Murimba EC, Gwenzi W (2017) Synthesis, characterisation and methyl orange adsorption capacity of ferric oxide-biochar nano-composites derived from pulp and paper sludge. Appl Water Sci 7:2175–2186. https://doi.org/10.1007/s13201-016-0392-5

Chen L, Yang S, Zuo X, Huang Y, Cai T, Ding D (2018) Biochar modification significantly promotes the activity of $Co_3O_4$ towards heterogeneous activation of peroxymonosulfate. Chem Eng J 354:856–865. https://doi.org/10.1016/j.cej.2018.08.098

Chen M, Yu D, Zheng X, Dong X (2019) Biomass based N-doped hierarchical porous carbon nanosheets for all-solid-state supercapacitors. J Energy Storage 21:105–112. https://doi.org/10.1016/j.est.2018.11.017

Chen Z, Wang X, Xue B, Li W, Ding Z, Yang X, Qiu J, Wang Z (2020) Rice husk-based hierarchical porous carbon for high performance supercapacitors: the structure-performance relationship. Carbon 161:432–444. https://doi.org/10.1016/j.carbon.2020.01.088

Chen W-H, Farooq W, Shahbaz M, Naqvi SR, Ali I, Al-Ansari T, Saidina Amin NA (2021) Current status of biohydrogen production from lignocellulosic biomass, technical challenges and commercial potential through pyrolysis process. Energy 226:120433. https://doi.org/10.1016/j.energy.2021.120433

Chen Y, Wu Y, Liao Y, Zhang Z, Luo S, Li L, Wu Y, Qing Y (2022) Tuning carbonized wood fiber via sacrificial template-assisted hydrothermal synthesis for high-performance lithium/sodium-ion batteries. J Power Sour 546:231993. https://doi.org/10.1016/j.jpowsour.2022.231993

Chen W-H, Chen W-H, Chein R-Y, Tuan Hoang A, Manatura K, Raza Naqvi S (2023) Optimization of hydrogen purification via vacuum pressure swing adsorption. Energy Convers Manag X 20:100459. https://doi.org/10.1016/j.ecmx.2023.100459

Cheng C, Guo Q, Ding L, Raheem A, He Q, Shiung Lam S, Yu G (2022) Upgradation of coconut waste shell to value-added hydrochar via hydrothermal carbonization: parametric optimization using response surface methodology. Appl Energy 327:120136. https://doi.org/10.1016/j.apenergy.2022.120136

Choi Y-K, Kan E (2019) Effects of pyrolysis temperature on the physicochemical properties of alfalfa-derived biochar for the adsorption of bisphenol A and sulfamethoxazole in water. Chemosphere 218:741–748. https://doi.org/10.1016/j.chemosphere.2018.11.151

Choi S, Kim H, Lee S, Wang Y, Ercan C, Othman R, Choi M (2015) Large-scale synthesis of high-quality zeolite-templated carbons without depositing external carbon layers. Chem Eng J 280:597–605. https://doi.org/10.1016/j.cej.2015.06.055

Chu J-H, Kang J-K, Park S-J, Lee C-G (2020) Application of magnetic biochar derived from food waste in heterogeneous sono-Fenton-like process for removal of organic dyes from aqueous solution. J Water Process Eng 37:101455. https://doi.org/10.1016/j.jwpe.2020.101455

Chu M, Tian W, Zhao J, Zou M, Lu Z, Zhang D, Jiang J (2022) A comprehensive review of capacitive deionization technology with biochar-based electrodes: biochar-based electrode preparation, deionization mechanism and applications. Chemosphere 307:136024. https://doi.org/10.1016/j.chemosphere.2022.136024

Cuong DV, Matsagar BM, Lee M, Hossain MSA, Yamauchi Y, Vithanage M, Sarkar B, Ok YS, Wu KCW, Hou C-H (2021) A critical review on biochar-based engineered hierarchical porous carbon for capacitive charge storage. Renew Sustain Energy Rev 145:111029. https://doi.org/10.1016/j.rser.2021.111029

Demir M, Farghaly AA, Decuir MJ, Collinson MM, Gupta RB (2018) Supercapacitance and oxygen reduction characteristics of sulfur self-doped micro/mesoporous bio-carbon derived from lignin. Mater Chem Phys 216:508–516. https://doi.org/10.1016/j.matchemphys.2018.06.008

Deng X, Zhao B, Zhu L, Shao Z (2015) Molten salt synthesis of nitrogen-doped carbon with hierarchical pore structures for use as high-performance electrodes in supercapacitors. Carbon 93:48–58. https://doi.org/10.1016/j.carbon.2015.05.031

Deng L, Zhang Y, Wang Y, Yuan H, Chen Y, Wu Y (2021) In situ N-, P- and Ca-codoped biochar derived from animal bones to boost the electrocatalytic hydrogen evolution reaction. Resour Conserv Recycl 170:105568. https://doi.org/10.1016/j.resconrec.2021.105568

Ding J, Wang H, Li Z, Cui K, Karpuzov D, Tan X, Kohandehghan A, Mitlin D (2015) Peanut shell hybrid sodium ion capacitor with extreme energy–power rivals lithium ion capacitors. Energy Environ Sci 8:941–955. https://doi.org/10.1039/C4EE02986K

Dong X, Liu X, Chen H, Xu X, Jiang H, Gu C, Li Q, Qiao S, Zhang X, Hu Y (2021) Hard template-assisted N, P-doped multifunctional mesoporous carbon for supercapacitors and hydrogen evolution reaction. J Mater Sci 56:2385–2398. https://doi.org/10.1007/s10853-020-05303-0

Dos Santos AC, Ximenes E, Kim Y, Ladisch MR (2019) Lignin–enzyme interactions in the hydrolysis of lignocellulosic biomass. Trends Biotechnol 37:518–531. https://doi.org/10.1016/j.tibtech.2018.10.010

Du W, Zhang Q, Shang Y, Wang W, Li Q, Yue Q, Gao B, Xu X (2020) Sulfate saturated biosorbent-derived Co-S@NC nanoarchitecture as an efficient catalyst for peroxymonosulfate activation. Appl Catal B 262:118302. https://doi.org/10.1016/j.apcatb.2019.118302

Egyir M, Luyima D, Park S-J, Lee KS, Oh T-K (2022) Volatilisations of ammonia from the soils amended with modified and nitrogen-enriched biochars. Sci Total Environ 835:155453. https://doi.org/10.1016/j.scitotenv.2022.155453

El-Naggar A, Lee SS, Rinklebe J, Farooq M, Song H, Sarmah AK, Zimmerman AR, Ahmad M, Shaheen SM, Ok YS (2019) Biochar application to low fertility soils: a review of current status, and future prospects. Geoderma 337:536–554. https://doi.org/10.1016/j.geoderma.2018.09.034

Fan C, Cui Y, Zhang Q, Yin N, Cai X, Yuan X, Senadheera S, Cho Y, Ok YS (2023) A critical review of the interactions between rhizosphere and biochar during the remediation of metal(loid) contaminated soils. Biochar 5:87. https://doi.org/10.1007/s42773-023-00278-y

Fang C, Zhang T, Li P, Jiang R-f, Wang Y-c (2014) Application of magnesium modified corn biochar for phosphorus removal and recovery from swine wastewater. Int J Environ Res Public Health 11:9217–9237. https://doi.org/10.3390/ijerph110909217

Fang L, Huang T, Lu H, Wu X-L, Chen Z, Yang H, Wang S, Tang Z, Li Z, Hu B, Wang X (2023) Biochar-based materials in environmental pollutant elimination, $H_2$ production and $CO_2$ capture applications. Biochar 5:42. https://doi.org/10.1007/s42773-023-00237-7

Feng C, Chen Y-A, Yu C-P, Hou C-H (2018a) Highly porous activated carbon with multi-channeled structure derived from loofa sponge as a capacitive electrode material for the deionization of brackish water. Chemosphere 208:285–293. https://doi.org/10.1016/j.chemosphere.2018.05.174

Feng J, Yang Z, Hou S, Li M, Lv R, Kang F, Huang Z-H (2018b) GO/auricularia-derived hierarchical porous carbon used for capacitive deionization with high performance. Colloids Surf A 547:134–140. https://doi.org/10.1016/j.colsurfa.2018.03.049

Feng Y, Jiang J, Xu Y, Wang S, An W, Chai Q, Prova UH, Wang C, Huang G (2023) Biomass derived diverse carbon nanostructure for electrocatalysis, energy conversion and storage. Carbon 211:118105. https://doi.org/10.1016/j.carbon.2023.118105

Fernández-Sanromán Á, Lama G, Pazos M, Rosales E, Sanromán MÁ (2021) Bridging the gap to hydrochar production and its application into frameworks of bioenergy, environmental and biocatalysis areas. Biores Technol 320:124399. https://doi.org/10.1016/j.biortech.2020.124399

Fu P, Zhou L, Sun L, Huang B, Yuan Y (2017) Nitrogen-doped porous activated carbon derived from cocoon silk as a highly efficient metal-free electrocatalyst for the oxygen reduction reaction. RSC Adv 7:13383–13389. https://doi.org/10.1039/C7RA00433H

Fu H, Zhao P, Xu S, Cheng G, Li Z, Li Y, Li K, Ma S (2019) Fabrication of $Fe_3O_4$ and graphitized porous biochar composites for activating peroxymonosulfate to degrade p-hydroxybenzoic acid: Insights on the mechanism. Chem Eng J 375:121980. https://doi.org/10.1016/j.cej.2019.121980

Gao Y, Zhang W, Yue Q, Gao B, Sun Y, Kong J, Zhao P (2014) Simple synthesis of hierarchical porous carbon from Enteromorpha prolifera by a self-template method for supercapacitor electrodes. J Power Sour 270:403–410. https://doi.org/10.1016/j.jpowsour.2014.07.115

Gao Z, Zhang P, Jiang R, Wang H, Zhi Q, Yu B, Jin Y, Sun T, Jiang J (2022) Co–Fe alloy nanoparticles and $Fe_3C$ nanocrystals on N-doped biomass-derived porous carbon for superior electrocatalytic oxygen reduction. J Solid State Chem 307:122735. https://doi.org/10.1016/j.jssc.2021.122735

Gasim MF, Choong Z-Y, Koo P-L, Low S-C, Hamidon TS, Hussin MH, Lin K-YA, Oh W-D (2023) Heteroatoms intra-actions and oxidant-pollutant competition over $BC_2O$ sites in N, S, B-tri-doped biochar for the nonradical activation of peroxymonosulfate. J Water Process Eng 55:104189. https://doi.org/10.1016/j.jwpe.2023.104189

Gohar H, Khoja AH, Ansari AA, Naqvi SR, Liaquat R, Hassan M, Hasni K, Qazi UY, Ali I (2022) Investigating the characterisation, kinetic mechanism, and thermodynamic behaviour of coal-biomass blends in co-pyrolysis process. Process Saf Environ Prot 163:645–658. https://doi.org/10.1016/j.psep.2022.05.063

Gong S, Xiao X, Wang W, Sam DK, Lu R, Xu Y, Liu J, Wu C, Lv X (2021) Silk fibroin-derived carbon aerogels embedded with copper nanoparticles for efficient electrocatalytic $CO_2$-to-CO conversion. J Colloid Interface Sci 600:412–420. https://doi.org/10.1016/j.jcis.2021.05.054

Gopalakrishnan A, Badhulika S (2020) Effect of self-doped heteroatoms on the performance of biomass-derived carbon for supercapacitor applications. J Power Sour 480:228830. https://doi.org/10.1016/j.jpowsour.2020.228830

Guo N, Li M, Wang Y, Sun X, Wang F, Yang R (2016) Soybean root-derived hierarchical porous carbon as electrode material for high-performance supercapacitors in ionic liquids. ACS Appl Mater Interfaces 8:33626–33634. https://doi.org/10.1021/acsami.6b11162

Guo T, Zhang X, Liu T, Wu Z, Wang D (2020) N, K Co-activated biochar-derived molybdenum carbide as efficient electrocatalysts for hydrogen evolution. Appl Surf Sci 509:144879. https://doi.org/10.1016/j.apsusc.2019.144879

Guo X, Li W, Zhang Q, Liu Y, Yuan G, Braunstein P, Pang H (2022) Ultrasmall metal (Fe Co, Ni) nanoparticles strengthen silicon oxide embedded nitrogen-doped carbon superstructures for long-cycle-life Li-ion-battery anodes. Chem Eng J 432:134413. https://doi.org/10.1016/j.cej.2021.134413

Guo X, Xu H, Li W, Liu Y, Shi Y, Li Q, Pang H (2023) Embedding atomically dispersed iron sites in nitrogen-doped carbon frameworks-wrapped silicon suboxide for superior lithium storage. Adv Sci 10:2206084. https://doi.org/10.1002/advs.202206084

Gutru R, Turtayeva Z, Xu F, Maranzana G, Thimmappa R, Mamlouk M, Desforges A, Vigolo B (2023) Recent progress in heteroatom doped carbon based electrocatalysts for oxygen reduction reaction in anion exchange membrane fuel cells. Int J Hydrogen Energy 48:3593–3631. https://doi.org/10.1016/j.ijhydene.2022.10.177

Haddad K, Jellali S, Jeguirim M, Ben Hassen Trabelsi A, Limousy L (2018) Investigations on phosphorus recovery from aqueous solutions by biochars derived from magnesium-pretreated cypress sawdust. J Environ Manage 216:305–314. https://doi.org/10.1016/j.jenvman.2017.06.020

Hameed A, Naqvi SR, Sikandar U, Chen W-H (2022) One-step biodiesel production from waste cooking oil using CaO promoted activated carbon catalyst from *Prunus persica* seeds. Catalysts. 12:592. https://doi.org/10.3390/catal12060592

Hamid Y, Liu L, Usman M, Naidu R, Haris M, Lin Q, Ulhassan Z, Hussain MI, Yang X (2022) Functionalized biochars: synthesis, characterization, and applications for removing trace elements from water. J Hazard Mater 437:129337. https://doi.org/10.1016/j.jhazmat.2022.129337

He C, Wang K, Giannis A, Yang Y, Wang J-Y (2015) Products evolution during hydrothermal conversion of dewatered sewage sludge in sub- and near-critical water: effects of reaction conditions and calcium oxide

additive. Int J Hydrogen Energy 40:5776–5787. https://doi.org/10.1016/j.ijhydene.2015.03.006

He D, Niu J, Dou M, Ji J, Huang Y, Wang F (2017) Nitrogen and oxygen co-doped carbon networks with a mesopore-dominant hierarchical porosity for high energy and power density supercapacitors. Electrochim Acta 238:310–318. https://doi.org/10.1016/j.electacta.2017.03.218

He G, Yan G, Song Y, Wang L (2020) Biomass juncus derived nitrogen-doped porous carbon materials for supercapacitor and oxygen reduction reaction. Front Chem 8:226. https://doi.org/10.3389/fchem.2020.00226

He H, Zhang R, Zhang P, Wang P, Chen N, Qian B, Zhang L, Yu J, Dai B (2023) Functional carbon from nature: biomass-derived carbon materials and the recent progress of their applications. Adv Sci 10:2205557. https://doi.org/10.1002/advs.202205557

Hou C-H, Liu N-L, Hsi H-C (2015a) Highly porous activated carbons from resource-recovered Leucaena leucocephala wood as capacitive deionization electrodes. Chemosphere 141:71–79. https://doi.org/10.1016/j.chemosphere.2015.06.055

Hou J, Cao C, Idrees F, Ma X (2015b) Hierarchical porous nitrogen-doped carbon nanosheets derived from silk for ultrahigh-capacity battery anodes and supercapacitors. ACS Nano 9:2556–2564. https://doi.org/10.1021/nn506394r

Hsu C-H, Chung C-H, Hsieh T-H, Lin H-P (2022) Green and highly-efficient microwave synthesis route for sulfur/carbon composite for Li-S battery. Int J Mol Sci. 23:39. https://doi.org/10.3390/ijms23010039

Hu L, Zhu Q, Wu Q, Li D, An Z, Xu B (2018) Natural biomass-derived hierarchical porous carbon synthesized by an in situ hard template coupled with NaOH activation for ultrahigh rate supercapacitors. ACS Sustain Chem Eng 6:13949–13959. https://doi.org/10.1021/acssuschemeng.8b02299

Hu H, Sun L, Wang T, Lv C, Gao Y, Zhang Y-F, Wu H, Chen X (2019) Nano-ZnO functionalized biochar as a superhydrophobic biosorbent for selective recovery of low-concentration Re(VII) from strong acidic solutions. Miner Eng 142:105885. https://doi.org/10.1016/j.mineng.2019.105885

Hu R, Xiao J, Wang T, Gong Y, Chen G, Chen L, Tian X (2020) Highly concentrated amino-modified biochars using a plasma: evolution of surface composition and porosity for heavy metal capture. Carbon 168:515–527. https://doi.org/10.1016/j.carbon.2020.07.012

Huang D, Liu C, Zhang C, Deng R, Wang R, Xue W, Luo H, Zeng G, Zhang Q, Guo X (2019) Cr(VI) removal from aqueous solution using biochar modified with Mg/Al-layered double hydroxide intercalated with ethylenediaminetetraacetic acid. Biores Technol 276:127–132. https://doi.org/10.1016/j.biortech.2018.12.114

Huang J, Feng Y, Xie H, Wu P, Wang M, Wang B, Zhang Q, Zhang S, Liu Z (2023a) A bibliographic study reviewing the last decade of hydrochar in environmental application: history, status quo, and trending research paths. Biochar 5:12. https://doi.org/10.1007/s42773-023-00210-4

Huang P, Zhang P, Wang C, Du X, Jia H, Sun H (2023b) P-doped biochar regulates nZVI nanocracks formation for superefficient persulfate activation. J Hazard Mater 450:130999. https://doi.org/10.1016/j.jhazmat.2023.130999

Incer-Valverde J, Mörsdorf J, Morosuk T, Tsatsaronis G (2023) Power-to-liquid hydrogen: exergy-based evaluation of a large-scale system. Int J Hydrogen Energy 48:11612–11627. https://doi.org/10.1016/j.ijhydene.2021.09.026

Issaka E, Fapohunda FO, Amu-Darko JNO, Yeboah L, Yakubu S, Varjani S, Ali N, Bilal M (2022) Biochar-based composites for remediation of polluted wastewater and soil environments: challenges and prospects. Chemosphere 297:134163. https://doi.org/10.1016/j.chemosphere.2022.134163

Ivanova N, Obaeed GLO, Sulkarnaev F, Buchkina N, Gubin A, Yurtaev A (2023) Effect of biochar aging in agricultural soil on its wetting properties and surface structure. Biochar 5:75. https://doi.org/10.1007/s42773-023-00272-4

Jang E-S, Ryu D-Y, Kim D (2022) Hydrothermal carbonization improves the quality of biochar derived from livestock manure by removing inorganic matter. Chemosphere 305:135391. https://doi.org/10.1016/j.chemosphere.2022.135391

Jellali S, Khiari B, Usman M, Hamdi H, Charabi Y, Jeguirim M (2021) Sludge-derived biochars: A review on the influence of synthesis conditions on pollutants removal efficiency from wastewaters. Renew Sustain Energy Rev 144:111068. https://doi.org/10.1016/j.rser.2021.111068

Jia S, Wei J, Meng X, Shao Z (2020) Facile and friendly preparation of N/S Co-doped graphene-like carbon nanosheets with hierarchical pore by molten salt for all-solid-state supercapacitor. Electrochim Acta 331:135338. https://doi.org/10.1016/j.electacta.2019.135338

Jiang D, Chu B, Amano Y, Machida M (2018) Removal and recovery of phosphate from water by Mg-laden biochar: batch and column studies. Colloids Surf A 558:429–437. https://doi.org/10.1016/j.colsurfa.2018.09.016

Jiang S-F, Ling L-L, Chen W-J, Liu W-J, Li D-C, Jiang H (2019a) High efficient removal of bisphenol A in a peroxymonosulfate/iron functionalized biochar system: mechanistic elucidation and quantification of the contributors. Chem Eng J 359:572–583. https://doi.org/10.1016/j.cej.2018.11.124

Jiang X, Xiang X, Peng S, Hou L (2019b) Facile preparation of nitrogen-doped activated mesoporous carbon aerogel from chitosan for methyl orange adsorption from aqueous solution. Cellulose 26:4515–4527. https://doi.org/10.1007/s10570-019-02368-2

Jiang E, Song N, Hong S, Xiao M, Zhu D, Yan Z, Sun J, Chen G, Li C, Dong H (2022) Cobalt supported on biomass carbon tubes derived from cotton fibers towards high-efficient electrocatalytic overall water-splitting. Electrochim Acta 407:139895. https://doi.org/10.1016/j.electacta.2022.139895

Jing H-P, Li Y, Wang X, Zhao J, Xia S (2019) Simultaneous recovery of phosphate, ammonium and humic acid from wastewater using a biochar supported Mg(OH)$_2$/bentonite composite. Environ Sci Water Res Technol 5:931–943. https://doi.org/10.1039/C8EW00952J

Jing H, Ji L, Li Z, Wang Z, Li R, Ju K (2023) Zn/Fe bimetallic modified Spartina alterniflora-derived biochar heterostructure with superior catalytic performance for the degradation of malachite green. Biochar 5:29. https://doi.org/10.1007/s42773-023-00227-9

Kaare K, Yu E, Volperts A, Dobele G, Zhurinsh A, Dyck A, Niaura G, Tamasauskaite-Tamasiunaite L, Norkus E, Andrulevičius M, Danilson M, Kruusenberg I (2020) Highly active wood-derived nitrogen-doped carbon catalyst for the oxygen reduction reaction. ACS Omega 5:23578–23587. https://doi.org/10.1021/acsomega.0c01974

Kalderis D, Görmez Ö, Saçlı B, Çalhan SD, Gözmen B (2023) Valorization of loquat seeds by hydrothermal carbonization for the production of hydrochars and aqueous phases as added-value products. J Environ Manage 344:118612. https://doi.org/10.1016/j.jenvman.2023.118612

Kamali M, Appels L, Kwon EE, Aminabhavi TM, Dewil R (2021) Biochar in water and wastewater treatment—a sustainability assessment. Chem Eng J 420:129946. https://doi.org/10.1016/j.cej.2021.129946

Kandel DR, Kim H-J, Lim J-M, Poudel MB, Cho M, Kim H-W, Oh B-T, Nah C, Lee SH, Dahal B, Lee J (2022) Cold plasma-assisted regeneration of biochar for dye adsorption. Chemosphere 309:136638. https://doi.org/10.1016/j.chemosphere.2022.136638

Karunanayake AG, Todd OA, Crowley M, Ricchetti L, Pittman CU, Anderson R, Mohan D, Mlsna T (2018) Lead and cadmium remediation using magnetized and nonmagnetized biochar from Douglas fir. Chem Eng J 331:480–491. https://doi.org/10.1016/j.cej.2017.08.124

Kasera N, Kolar P, Hall SG (2022) Nitrogen-doped biochars as adsorbents for mitigation of heavy metals and organics from water: a review. Biochar 4:17. https://doi.org/10.1007/s42773-022-00145-2

Kaur P, Verma G, Sekhon SS (2019) Biomass derived hierarchical porous carbon materials as oxygen reduction reaction electrocatalysts in fuel cells. Prog Mater Sci 102:1–71. https://doi.org/10.1016/j.pmatsci.2018.12.002

Kaur A, Bajaj B, Kaushik A, Saini A, Sud D (2022) A review on template assisted synthesis of multi-functional metal oxide nanostructures: status and prospects. Mater Sci Eng, B 286:116005. https://doi.org/10.1016/j.mseb.2022.116005

Kazemi Shariat Panahi H, Dehhaghi M, Ok YS, Nizami A-S, Khoshnevisan B, Mussatto SI, Aghbashlo M, Tabatabaei M, Lam SS (2020) A comprehensive review of engineered biochar: production, characteristics, and environmental applications. J Clean Prod 270:122462. https://doi.org/10.1016/j.jclepro.2020.122462

Khan HA, Naqvi SR, Mehran MT, Khoja AH, Khan Niazi MB, Juchelková D, Atabani A (2021) A performance evaluation study of nano-biochar as a potential slow-release nano-fertilizer from wheat straw residue for sustainable agriculture. Chemosphere 285:131382. https://doi.org/10.1016/j.chemosphere.2021.131382

Khan A, Ali I, Farooq W, Naqvi SR, Mehran MT, Shahid A, Liaquat R, Waqas Anjum M, Naqvi M (2022a) Investigation of combustion performance of tannery sewage sludge using thermokinetic analysis and prediction by

artificial neural network. Case Stud Therm Eng 40:102586. https://doi.org/10.1016/j.csite.2022.102586

Khan AA, Gul J, Naqvi SR, Ali I, Farooq W, Liaqat R, AlMohamadi H, Štěpanec L, Juchelková D (2022b) Recent progress in microalgae-derived biochar for the treatment of textile industry wastewater. Chemosphere 306:135565. https://doi.org/10.1016/j.chemosphere.2022.135565

Khan M, Ullah Z, Mašek O, Raza Naqvi S, Nouman Aslam Khan M (2022c) Artificial neural networks for the prediction of biochar yield: a comparative study of metaheuristic algorithms. Biores Technol 355:127215. https://doi.org/10.1016/j.biortech.2022.127215

Khan A, Ali I, Naqvi SR, AlMohamadi H, Shahbaz M, Ali AM, Shahzad K (2023a) Assessment of thermokinetic behaviour of tannery sludge in slow pyrolysis process through artificial neural network. Chemosphere 337:139226. https://doi.org/10.1016/j.chemosphere.2023.139226

Khan AA, Naqvi SR, Ali I, Arshad M, AlMohamadi H, Sikandar U (2023b) Algal-derived biochar as an efficient adsorbent for removal of Cr (VI) in textile industry wastewater: non-linear isotherm, kinetics and ANN studies. Chemosphere 316:137826. https://doi.org/10.1016/j.chemosphere.2023.137826

Khan AA, Naqvi SR, Ali I, Farooq W, Anjum MW, AlMohamadi H, Lam SS, Verma M, Ng HS, Liew RK (2023c) Algal biochar: A natural solution for the removal of Congo red dye from textile wastewater. J Taiwan Inst Chem Eng. 105312. https://doi.org/10.1016/j.jtice.2023.105312

Khan M, Raza Naqvi S, Ullah Z, Ali Ammar Taqvi S, Nouman Aslam Khan M, Farooq W, Taqi Mehran M, Juchelková D, Štěpanec L (2023d) Applications of machine learning in thermochemical conversion of biomass—a review. Fuel 332:126055. https://doi.org/10.1016/j.fuel.2022.126055

Khan R, Shukla S, Kumar M, Zuorro A, Pandey A (2023e) Sewage sludge derived biochar and its potential for sustainable environment in circular economy: advantages and challenges. Chem Eng J 471:144495. https://doi.org/10.1016/j.cej.2023.144495

Kharel G, Sacko O, Feng X, Morris JR, Phillips CL, Trippe K, Kumar S, Lee JW (2019) Biochar surface oxygenation by ozonization for super high cation exchange capacity. ACS Sustain Chem Eng 7:16410–16418. https://doi.org/10.1021/acssuschemeng.9b03536

Kim M-J, Choi SW, Kim H, Mun S, Lee KB (2020) Simple synthesis of spent coffee ground-based microporous carbons using $K_2CO_3$ as an activation agent and their application to $CO_2$ capture. Chem Eng J 397:125404. https://doi.org/10.1016/j.cej.2020.125404

Kizito S, Luo H, Wu S, Ajmal Z, Lv T, Dong R (2017) Phosphate recovery from liquid fraction of anaerobic digestate using four slow pyrolyzed biochars: dynamics of adsorption, desorption and regeneration. J Environ Manag 201:260–267. https://doi.org/10.1016/j.jenvman.2017.06.057

Kong X, Chen S, Zou Y, Lyu S, She X, Lu Y, Sun J, Zhang H, Yang D (2018) Cellulose nanocrystals (CNC) derived $Mo_2C$@sulfur-doped carbon aerogels for hydrogen evolution. Int J Hydrogen Energy 43:13720–13726. https://doi.org/10.1016/j.ijhydene.2018.01.072

Kulkarni R, Lingamdinne LP, Karri RR, Momin ZH, Koduru JR, Chang Y-Y (2023) Catalytic efficiency of LDH@carbonaceous hybrid nanocomposites towards water splitting mechanism: impact of plasma and its significance on HER and OER activity. Coord Chem Rev 497:215460. https://doi.org/10.1016/j.ccr.2023.215460

Kumar M, Xiong X, Wan Z, Sun Y, Tsang DCW, Gupta J, Gao B, Cao X, Tang J, Ok YS (2020) Ball milling as a mechanochemical technology for fabrication of novel biochar nanomaterials. Biores Technol 312:123613. https://doi.org/10.1016/j.biortech.2020.123613

Lahijani P, Mohammadi M, Mohamed AR (2018) Metal incorporated biochar as a potential adsorbent for high capacity $CO_2$ capture at ambient condition. J CO2 Util 26:281–293. https://doi.org/10.1016/j.jcou.2018.05.018

Lau AYT, Tsang DCW, Graham NJD, Ok YS, Yang X, Li X-d (2017) Surface-modified biochar in a bioretention system for *Escherichia coli* removal from stormwater. Chemosphere 169:89–98. https://doi.org/10.1016/j.chemosphere.2016.11.048

Lei S, Chen L, Zhou W, Deng P, Liu Y, Fei L, Lu W, Xiao Y, Cheng B (2018) Tetra-heteroatom self-doped carbon nanosheets derived from silkworm excrement for high-performance supercapacitors. J Power Sour 379:74–83. https://doi.org/10.1016/j.jpowsour.2018.01.032

Lei W, Yang B, Sun Y, Xiao L, Tang D, Chen K, Sun J, Ke J, Zhuang Y (2021) Self-sacrificial template synthesis of heteroatom doped porous biochar for enhanced electrochemical energy storage. J Power Sour 488:229455. https://doi.org/10.1016/j.jpowsour.2021.229455

Lei C, Lu T, Qian H, Liu Y (2023) Machine learning models reveal how biochar amendment affects soil microbial communities. Biochar 5:89. https://doi.org/10.1007/s42773-023-00291-1

Li R, Wang JJ, Zhou B, Awasthi MK, Ali A, Zhang Z, Gaston LA, Lahori AH, Mahar A (2016a) Enhancing phosphate adsorption by Mg/Al layered double hydroxide functionalized biochar with different Mg/Al ratios. Sci Total Environ 559:121–129. https://doi.org/10.1016/j.scitotenv.2016.03.151

Li R, Wang JJ, Zhou B, Awasthi MK, Ali A, Zhang Z, Lahori AH, Mahar A (2016b) Recovery of phosphate from aqueous solution by magnesium oxide decorated magnetic biochar and its potential as phosphate-based fertilizer substitute. Biores Technol 215:209–214. https://doi.org/10.1016/j.biortech.2016.02.125

Li R, Wang JJ, Zhou B, Zhang Z, Liu S, Lei S, Xiao R (2017) Simultaneous capture removal of phosphate, ammonium and organic substances by MgO impregnated biochar and its potential use in swine wastewater treatment. J Clean Prod 147:96–107. https://doi.org/10.1016/j.jclepro.2017.01.069

Li J, Gao S, Li B, Li Y, Cheng C, Maouche C, Wu Y, Rahman N, Zhou Y, Yang J (2020a) Biomass-derived nitrogen-doped porous carbons with ultra-high surface area for electrocatalytic oxygen reduction reaction. J Electroanal Chem 878:114542. https://doi.org/10.1016/j.jelechem.2020.114542

Li J, Jiang Q, Wei L, Zhong L, Wang X (2020b) Simple and scalable synthesis of hierarchical porous carbon derived from cornstalk without pith for high capacitance and energy density. J Mater Chem A 8:1469–1479. https://doi.org/10.1039/C9TA07864A

Li Y, Ma S, Xu S, Fu H, Li Z, Li K, Sheng K, Du J, Lu X, Li X, Liu S (2020c) Novel magnetic biochar as an activator for peroxymonosulfate to degrade bisphenol A: emphasizing the synergistic effect between graphitized structure and $CoFe_2O_4$. Chem Eng J 387:124094. https://doi.org/10.1016/j.cej.2020.124094

Li Z, Sun Y, Yang Y, Han Y, Wang T, Chen J, Tsang DCW (2020d) Comparing biochar- and bentonite-supported Fe-based catalysts for selective degradation of antibiotics: mechanisms and pathway. Environ Res 183:109156. https://doi.org/10.1016/j.envres.2020.109156

Li C, Feng Y, Zhong F, Deng J, Yu T, Cao H, Niu W (2022a) Optimization of microwave-assisted hydrothermal carbonization and potassium bicarbonate activation on the structure and electrochemical characteristics of crop straw-derived biochar. J Energy Storage 55:105838. https://doi.org/10.1016/j.est.2022.105838

Li N, He M, Lu X, Yan B, Duan X, Chen G, Wang S, La H (2022b) Municipal solid waste derived biochars for wastewater treatment: production, properties and applications. Resour Conserv Recycl 177:106003. https://doi.org/10.1016/j.resconrec.2021.106003

Li Z, Gao C, Zhao H, Meng A, Ding S, Wang X, Li S (2022c) Porous biomass-derived carbon modified by Cu, N co-doping and Cu nanoparticles as high-efficient electrocatalyst for oxygen reduction reaction and zinc-air battery. J Alloy Compd 897:163175. https://doi.org/10.1016/j.jallcom.2021.163175

Liang W, Wang G, Xu R, Ning X, Zhang J, Guo A, Ye L, Li J, Jiang C, Wang P, Wang C (2022) Hydrothermal carbonization of forest waste into solid fuel: Mechanism and combustion behavior. Energy 246:123343. https://doi.org/10.1016/j.energy.2022.123343

Lin L, Li Z, Liu X, Qiu W, Song Z (2019) Effects of Fe-Mn modified biochar composite treatment on the properties of As-polluted paddy soil. Environ Pollut 244:600–607. https://doi.org/10.1016/j.envpol.2018.10.011

Lin H, Liu Y, Chang Z, Yan S, Liu S, Han S (2020) A new method of synthesizing hemicellulose-derived porous activated carbon for high-performance supercapacitors. Microporous Mesoporous Mater 292:109707. https://doi.org/10.1016/j.micromeso.2019.109707

Liu D, Zhang W, Lin H, Li Y, Lu H, Wang Y (2015) Hierarchical porous carbon based on the self-templating structure of rice husk for high-performance supercapacitors. RSC Adv 5:19294–19300. https://doi.org/10.1039/C4RA15111A

Liu J, Deng Y, Li X, Wang L (2016) Promising nitrogen-rich porous carbons derived from one-step calcium chloride activation of biomass-based waste for high performance supercapacitors. ACS Sustain Chem Eng 4:177–187. https://doi.org/10.1021/acssuschemeng.5b00926

Liu B, Yang M, Chen H, Liu Y, Yang D, Li H (2018) Graphene-like porous carbon nanosheets derived from salvia splendens for high-rate performance

supercapacitors. J Power Sour 397:1–10. https://doi.org/10.1016/j.jpowsour.2018.06.100

Liu C, Chen L, Ding D, Cai T (2019a) From rice straw to magnetically recoverable nitrogen doped biochar: efficient activation of peroxymonosulfate for the degradation of metolachlor. Appl Catal B 254:312–320. https://doi.org/10.1016/j.apcatb.2019.05.014

Liu F, Wang Z, Zhang H, Jin L, Chu X, Gu B, Huang H, Yang W (2019b) Nitrogen, oxygen and sulfur co-doped hierarchical porous carbons toward high-performance supercapacitors by direct pyrolysis of kraft lignin. Carbon 149:105–116. https://doi.org/10.1016/j.carbon.2019.04.023

Liu X, Culhane C, Li W, Zou S (2020a) Spinach-derived porous carbon nanosheets as high-performance catalysts for oxygen reduction reaction. ACS Omega 5:24367–24378. https://doi.org/10.1021/acsomega.0c02673

Liu Y, Su M, Li D, Li S, Li X, Zhao J, Liu F (2020b) Soybean straw biomass-derived Fe–N co-doped porous carbon as an efficient electrocatalyst for oxygen reduction in both alkaline and acidic media. RSC Adv 10:6763–6771. https://doi.org/10.1039/C9RA07539A

Lu L, Chen B (2018) Enhanced bisphenol A removal from stormwater in biochar-amended biofilters: combined with batch sorption and fixed-bed column studies. Environ Pollut 243:1539–1549. https://doi.org/10.1016/j.envpol.2018.09.097

Lu Z, Chen J, Wang W, Li W, Sun M, Wang Y, Wang X, Ye J, Rao H (2021) Electrocatalytic, kinetic, and mechanism insights into the oxygen-reduction catalyzed based on the biomass-derived $FeO_x$@N-Doped porous carbon composites. Small 17:2007326. https://doi.org/10.1002/smll.202007326

Lu Y, Cai Y, Zhang S, Zhuang L, Hu B, Wang S, Chen J, Wang X (2022) Application of biochar-based photocatalysts for adsorption-(photo) degradation/reduction of environmental contaminants: mechanism, challenges and perspective. Biochar 4:45. https://doi.org/10.1007/s42773-022-00173-y

Lu J, Li Y, Cai Y, Jiang P, Yu B (2023) Co-incorporation of hydrotalcite and starch into biochar-based fertilizers for the synthesis of slow-release fertilizers with improved water retention. Biochar 5:44. https://doi.org/10.1007/s42773-023-00242-w

Luo M, Lin H, He Y, Li B, Dong Y, Wang L (2019) Efficient simultaneous removal of cadmium and arsenic in aqueous solution by titanium-modified ultrasonic biochar. Biores Technol 284:333–339. https://doi.org/10.1016/j.biortech.2019.03.108

Luo Z, Lin N, Sun M, Wang Y, Zhu X (2021) Synthesis of 3D-interconnected hierarchical porous carbon from heavy fraction of bio-oil using crayfish shell as the biological template for high-performance supercapacitors. Carbon 173:910–917. https://doi.org/10.1016/j.carbon.2020.11.083

Luo L, Lan Y, Zhang Q, Deng J, Luo L, Zeng Q, Gao H, Zhao W (2022) A review on biomass-derived activated carbon as electrode materials for energy storage supercapacitors. J Energy Storage 55:105839. https://doi.org/10.1016/j.est.2022.105839

Ma J, Zhou B, Zhang H, Zhang W (2020) Fe/S modified sludge-based biochar for tetracycline removal from water. Powder Technol 364:889–900. https://doi.org/10.1016/j.powtec.2019.10.107

Mahmood Ali A, Khan A, Shahbaz M, Imtiaz Rashid M, Imran M, Shahzad K, Binti Mahpudz A (2023) A renewable and sustainable framework for clean fuel towards circular economy for solid waste generation in leather tanneries. Fuel 351:128962. https://doi.org/10.1016/j.fuel.2023.128962

Mahmoud DK, Salleh MAM, Karim WAWA, Idris A, Abidin ZZ (2012) Batch adsorption of basic dye using acid treated kenaf fibre char: equilibrium, kinetic and thermodynamic studies. Chem Eng J 181–182:449–457. https://doi.org/10.1016/j.cej.2011.11.116

Mamaní A, Ramírez N, Deiana C, Giménez M, Sardella F (2019) Highly microporous sorbents from lignocellulosic biomass: different activation routes and their application to dyes adsorption. J Environ Chem Eng 7:103148. https://doi.org/10.1016/j.jece.2019.103148

Mannarino G, Sarrion A, Diaz E, Gori R, De la Rubia MA, Mohedano AF (2022) Improved energy recovery from food waste through hydrothermal carbonization and anaerobic digestion. Waste Manage 142:9–18. https://doi.org/10.1016/j.wasman.2022.02.003

Marshall JA, Morton BJ, Muhlack R, Chittleborough D, Kwong CW (2017) Recovery of phosphate from calcium-containing aqueous solution resulting from biochar-induced calcium phosphate precipitation. J Clean Prod 165:27–35. https://doi.org/10.1016/j.jclepro.2017.07.042

Mehdi R, Naqvi SR, Khoja AH, Hussain R (2023) Biomass derived activated carbon by chemical surface modification as a source of clean energy for supercapacitor application. Fuel 348:128529. https://doi.org/10.1016/j.fuel.2023.128529

Mian MM, Kamana IML, An X, Abbas SC, Ahommed MS, He Z, Ni Y (2023) Cellulose nanofibers as effective binders for activated biochar-derived high-performance supercapacitors. Carbohyd Polym 301:120353. https://doi.org/10.1016/j.carbpol.2022.120353

Miao W, Li S, Cao X, Lv E, Yu H, Zhang X, Dong X (2022) Wood-derived porous carbon supported $\gamma$-$Fe_2O_3$ nanoparticles as efficient catalyst for oxygen reduction reaction. Appl Surf Sci 604:154471. https://doi.org/10.1016/j.apsusc.2022.154471

Min S, Duan Y, Li Y, Wang F (2020) Biomass-derived self-supported porous carbon membrane embedded with Co nanoparticles as an advanced electrocatalyst for efficient and robust hydrogen evolution reaction. Renewable Energy 155:447–455. https://doi.org/10.1016/j.renene.2020.03.164

Mohanty P, Nanda S, Pant KK, Naik S, Kozinski JA, Dalai AK (2013) Evaluation of the physiochemical development of biochars obtained from pyrolysis of wheat straw, timothy grass and pinewood: effects of heating rate. J Anal Appl Pyrol 104:485–493. https://doi.org/10.1016/j.jaap.2013.05.022

Mosa A, El-Ghamry A, Tolba M (2018) Functionalized biochar derived from heavy metal rich feedstock: phosphate recovery and reusing the exhausted biochar as an enriched soil amendment. Chemosphere 198:351–363. https://doi.org/10.1016/j.chemosphere.2018.01.113

Mu Y, Zhang Y, Fang L, Liu L, Zhang H, Wang Y (2016) Controllable synthesis of molybdenum carbide nanoparticles embedded in porous graphitized carbon matrixes as efficient electrocatalyst for hydrogen evolution reaction. Electrochim Acta 215:357–365. https://doi.org/10.1016/j.electacta.2016.08.104

Naqvi SR, Jamshaid S, Naqvi M, Farooq W, Niazi MBK, Aman Z, Zubair M, Ali M, Shahbaz M, Inayat A, Afzal W (2018a) Potential of biomass for bioenergy in Pakistan based on present case and future perspectives. Renew Sustain Energy Rev 81:1247–1258. https://doi.org/10.1016/j.rser.2017.08.012

Naqvi SR, Tariq R, Hameed Z, Ali I, Taqvi SA, Naqvi M, Niazi MBK, Noor T, Farooq W (2018b) Pyrolysis of high-ash sewage sludge: thermo-kinetic study using TGA and artificial neural networks. Fuel 233:529–538. https://doi.org/10.1016/j.fuel.2018.06.089

Naqvi SR, Tariq R, Hameed Z, Ali I, Naqvi M, Chen W-H, Ceylan S, Rashid H, Ahmad J, Taqvi SA, Shahbaz M (2019) Pyrolysis of high ash sewage sludge: kinetics and thermodynamic analysis using Coats-Redfern method. Renewable Energy 131:854–860. https://doi.org/10.1016/j.renene.2018.07.094

Naqvi SR, Khoja AH, Ali I, Naqvi M, Noor T, Ahmad A, Luque R, Amin NAS (2023) Recent progress in catalytic deoxygenation of biomass pyrolysis oil using microporous zeolites for green fuels production. Fuel 333:126268. https://doi.org/10.1016/j.fuel.2022.126268

Naveed MH, Khan MNA, Mukarram M, Naqvi SR, Abdullah A, Haq ZU, Ullah H, Mohamadi HA (2024) Cellulosic biomass fermentation for biofuel production: review of artificial intelligence approaches. Renew Sustain Energy Rev 189:113906. https://doi.org/10.1016/j.rser.2023.113906

Nguyen V-T, Nguyen T-B, Chen C-W, Hung C-M, Huang CP, Dong C-D (2019) Cobalt-impregnated biochar (Co-SCG) for heterogeneous activation of peroxymonosulfate for removal of tetracycline in water. Biores Technol 292:121954. https://doi.org/10.1016/j.biortech.2019.121954

Nielsen DU, Hu X-M, Daasbjerg K, Skrydstrup T (2018) Chemically and electro-chemically catalysed conversion of $CO_2$ to CO with follow-up utilization to value-added chemicals. Nat Catal 1:244–254. https://doi.org/10.1038/s41929-018-0051-3

Norouzi O, Maria FD, Dutta A (2020) Biochar-based composites as electrode active materials in hybrid supercapacitors with particular focus on surface topography and morphology. J Energy Storage 29:101291. https://doi.org/10.1016/j.est.2020.101291

Nowrouzi M, Younesi H, Bahramifar N (2018) Superior $CO_2$ capture performance on biomass-derived carbon/metal oxides nanocomposites from Persian ironwood by $H_3PO_4$ activation. Fuel 223:99–114. https://doi.org/10.1016/j.fuel.2018.03.035

Oh W-D, Lisak G, Webster RD, Liang Y-N, Veksha A, Giannis A, Moo JGS, Lim J-W, Lim T-T (2018) Insights into the thermolytic transformation of lignocellulosic biomass waste to redox-active carbocatalyst: durability of surface active sites. Appl Catal B 233:120–129. https://doi.org/10.1016/j.apcatb.2018.03.106

Ohms D, Herzog S, Franke R, Neumann V, Wiesener K, Gamburcev S, Kaisheva A, Iliev I (1992) Influence of metal ions on the electrocatalytic oxygen reduction of carbon materials prepared from pyrolyzed polyacrylonitrile. J Power Sour 38:327–334. https://doi.org/10.1016/0378-7753(92)80122-R

Ortiz-Ortega E, Hosseini S, Martinez-Chapa SO, Madou MJ (2021) Aging of plasma-activated carbon surfaces: challenges and opportunities. Appl Surf Sci 565:150362. https://doi.org/10.1016/j.apsusc.2021.150362

Ou W, Lan X, Guo J, Cai A, Liu P, Liu N, Liu Y, Lei Y (2023) Preparation of iron/calcium-modified biochar for phosphate removal from industrial wastewater. J Clean Prod 383:135468. https://doi.org/10.1016/j.jclepro.2022.135468

Ouyang P, Narayanan M, Shi X, Chen X, Li Z, Luo Y, Ma Y (2023) Integrating biochar and bacteria for sustainable remediation of metal-contaminated soils. Biochar 5:63. https://doi.org/10.1007/s42773-023-00265-3

Park S, Kim J, Kwon K (2022) A review on biomass-derived N-doped carbons as electrocatalysts in electrochemical energy applications. Chem Eng J 446:137116. https://doi.org/10.1016/j.cej.2022.137116

Park J-H, Yun J-J, Kim S-H, Park J-H, Acharya BS, Cho J-S, Kang S-W (2023a) Biochar improves soil properties and corn productivity under drought conditions in South Korea. Biochar 5:66. https://doi.org/10.1007/s42773-023-00267-1

Park S, Song J, Lee WC, Jang S, Lee J, Kim J, Kim H-K, Min K (2023b) Advances in biomass-derived electrode materials for energy storage and circular carbon economy. Chem Eng J 470:144234. https://doi.org/10.1016/j.cej.2023.144234

Peng L, Liang Y, Huang J, Xing L, Hu H, Xiao Y, Dong H, Liu Y, Zheng M (2019) Mixed-biomass wastes derived hierarchically porous carbons for high-performance electrochemical energy storage. ACS Sustain Chem Eng 7:10393–10402. https://doi.org/10.1021/acssuschemeng.9b00477

Poomsawat S, Poomsawat W (2021) Analysis of hydrochar fuel characterization and combustion behavior derived from aquatic biomass via hydrothermal carbonization process. Case Stud Therm Eng 27:101255. https://doi.org/10.1016/j.csite.2021.101255

Potnuri R, Surya DV, Rao CS, Yadav A, Sridevi V, Remya N (2023) A review on analysis of biochar produced from microwave-assisted pyrolysis of agricultural waste biomass. J Anal Appl Pyrol 173:106094. https://doi.org/10.1016/j.jaap.2023.106094

Prasongthum N, Suemanotham A, Sisuthog W, Thanmongkhon Y, Chaiya C, Attanatho L (2023) Hydrothermal carbonization of oil palm trunk: hydrochar properties and combustion behaviors. Energy Rep 9:380–386. https://doi.org/10.1016/j.egyr.2023.09.033

Qi X, Zhang H, Li C, Chen D, Sun C, Yang Z (2020) A simple and recyclable molten-salt route to prepare superthin biocarbon sheets based on the high water-absorbent agaric for efficient lithium storage. Carbon 157:286–294. https://doi.org/10.1016/j.carbon.2019.10.050

Qiao S, Zhao J, Zhang B, Liu C, Li Z, Hu S, Li Q (2019) Micrometer-Scale biomass carbon tube matrix auxiliary $MoS_2$ heterojunction for electrocatalytic hydrogen evolution. Int J Hydrogen Energy 44:32019–32029. https://doi.org/10.1016/j.ijhydene.2019.10.117

Qin L, Zhou Z, Dai J, Ma P, Zhao H, He J, Xie A, Li C, Yan Y (2016) Novel N-doped hierarchically porous carbons derived from sustainable shrimp shell for high-performance removal of sulfamethazine and chloramphenicol. J Taiwan Inst Chem Eng 62:228–238. https://doi.org/10.1016/j.jtice.2016.02.009

Qin L, Zeng Z, Zeng G, Lai C, Duan A, Xiao R, Huang D, Fu Y, Yi H, Li B, Liu X, Liu S, Zhang M, Jiang D (2019) Cooperative catalytic performance of bimetallic Ni-Au nanocatalyst for highly efficient hydrogenation of nitroaromatics and corresponding mechanism insight. Appl Catal B 259:118035. https://doi.org/10.1016/j.apcatb.2019.118035

Qin C, Wang H, Yuan X, Xiong T, Zhang J, Zhang J (2020) Understanding structure-performance correlation of biochar materials in environmental remediation and electrochemical devices. Chem Eng J 382:122977. https://doi.org/10.1016/j.cej.2019.122977

Qu Y, Guo M, Wang X, Yuan C (2019) Novel nitrogen-doped ordered mesoporous carbon as high-performance anode material for sodium-ion batteries. J Alloy Compd 791:874–882. https://doi.org/10.1016/j.jallcom.2019.03.370

Raj CJ, Rajesh M, Manikandan R, Yu KH, Anusha JR, Ahn JH, Kim D-W, Park SY, Kim BC (2018) High electrochemical capacitor performance of oxygen and nitrogen enriched activated carbon derived from the pyrolysis and activation of squid gladius chitin. J Power Sour 386:66–76. https://doi.org/10.1016/j.jpowsour.2018.03.038

Ramos R, Abdelkader-Fernández VK, Matos R, Peixoto AF, Fernandes DM (2022) Metal-supported biochar catalysts for sustainable biorefinery, electrocatalysis, and energy storage applications: a review. Catalysts 12:207. https://doi.org/10.3390/catal12020207

Reijnders L (2014) Phosphorus resources, their depletion and conservation, a review. Resour Conserv Recycl 93:32–49. https://doi.org/10.1016/j.resconrec.2014.09.006

Ren M, Jia Z, Tian Z, Lopez D, Cai J, Titirici M-M, Jorge AB (2018) High performance N-doped carbon electrodes obtained via hydrothermal carbonization of macroalgae for supercapacitor applications. ChemElectroChem 5:2686–2693. https://doi.org/10.1002/celc.201800603

Rex P, Mohammed Ismail KR, Meenakshisundaram N, Barmavatu P, Sai Bharadwaj AV (2023) Agricultural biomass waste to biochar: a review on biochar applications using machine learning approach and circular economy. ChemEngineering 7:50. https://doi.org/10.3390/chemengineering7030050

Robinson J, Binner E, Vallejo DB, Perez ND, Al Mughairi K, Ryan J, Shepherd B, Adam M, Budarin V, Fan J, Gronnow M, Peneranda-Foix F (2022) Unravelling the mechanisms of microwave pyrolysis of biomass. Chem Eng J 430:132975. https://doi.org/10.1016/j.cej.2021.132975

Rong X, Xie M, Kong L, Natarajan V, Ma L, Zhan J (2019) The magnetic biochar derived from banana peels as a persulfate activator for organic contaminants degradation. Chem Eng J 372:294–303. https://doi.org/10.1016/j.cej.2019.04.135

Saleem F, Khoja AH, Khan A, Rehman A, Naqvi SR, Qazi UY, Zhang K, Harvey A (2023) Effect of non-thermal plasma dielectric barrier discharge reactor on the quality of biomass gasification product gas from the gasifier. J Energy Inst 108:101228. https://doi.org/10.1016/j.joei.2023.101228

Samuel Olugbenga O, Goodness Adeleye P, Blessing Oladipupo S, Timothy Adeleye A, Igenepo John K (2024) Biomass-derived biochar in wastewater treatment—a circular economy approach. Waste Manag Bull 1:1–14. https://doi.org/10.1016/j.wmb.2023.07.007

Sarwar A, Ali M, Khoja AH, Nawar A, Waqas A, Liaquat R, Naqvi SR, Asjid M (2021) Synthesis and characterization of biomass-derived surface-modified activated carbon for enhanced $CO_2$ adsorption. J CO2 Util 46:101476. https://doi.org/10.1016/j.jcou.2021.101476

Sathiskumar C, Ramakrishnan S, Vinothkannan M, Rhan Kim A, Karthikeyan S, Yoo DJ (2020) Nitrogen-doped porous carbon derived from biomass used as trifunctional electrocatalyst toward oxygen reduction, oxygen evolution and hydrogen evolution reactions. Nanomaterials 10:76. https://doi.org/10.3390/nano10010076

Schmies H, Bengen N, Müller-Hülstede J, Ibitowa OA, Wagner P, Wark M (2023) How effective is graphitization of biomasses for the carbon stability of Pt/C ORR catalysts? Catalysts 13:343. https://doi.org/10.3390/catal13020343

Scrinzi D, Bona D, Denaro A, Silvestri S, Andreottola G, Fiori L (2022) Hydrochar and hydrochar co-compost from OFMSW digestate for soil application: 1. Production and chemical characterization. J Environ Manag 309:114688. https://doi.org/10.1016/j.jenvman.2022.114688

Shah SS, Aziz MA, Usman M, Hakeem AS, Ali S, Alzahrani AS (2023) Biomass-based supercapacitors: lab to industry. Biomass-based supercapacitors. Wiley, USA, pp 435–459. https://doi.org/10.1002/9781119866435.ch25

Shan R, Shi Y, Gu J, Bi J, Yuan H, Luo B, Chen Y (2020) Aqueous Cr(VI) removal by biochar derived from waste mangosteen shells: Role of pyrolysis and modification on its absorption process. J Environ Chem Eng 8:103885. https://doi.org/10.1016/j.jece.2020.103885

Shen F, Xiong X, Fu J, Yang J, Qiu M, Qi X, Tsang DCW (2020) Recent advances in mechanochemical production of chemicals and carbon materials from sustainable biomass resources. Renew Sustain Energy Rev 130:109944. https://doi.org/10.1016/j.rser.2020.109944

Shi C, Maimaitiyiming X (2021) Biomass-derived precious metal-free porous carbon: Ca-N, P-doped carbon materials and its electrocatalytic properties. J Alloy Compd 883:160726. https://doi.org/10.1016/j.jallcom.2021.160726

Shyam S, Arun J, Gopinath KP, Ribhu G, Ashish M, Ajay S (2022) Biomass as source for hydrochar and biochar production to recover phosphates from wastewater: a review on challenges, commercialization, and future perspectives. Chemosphere 286:131490. https://doi.org/10.1016/j.chemosphere.2021.131490

Singh G, Maria Ruban A, Geng X, Vinu A (2023) Recognizing the potential of K-salts, apart from KOH, for generating porous carbons using chemical activation. Chem Eng J 451:139045. https://doi.org/10.1016/j.cej.2022.139045

Sizmur T, Fresno T, Akgül G, Frost H, Moreno-Jiménez E (2017) Biochar modification to enhance sorption of inorganics from water. Biores Technol 246:34–47. https://doi.org/10.1016/j.biortech.2017.07.082

Soltani N, Bahrami A, Giebeler L, Gemming T, Mikhailova D (2021) Progress and challenges in using sustainable carbon anodes in rechargeable metal-ion batteries. Prog Energy Combust Sci 87:100929. https://doi.org/10.1016/j.pecs.2021.100929

Song S, Ma F, Wu G, Ma D, Geng W, Wan J (2015) Facile self-templating large scale preparation of biomass-derived 3D hierarchical porous carbon for advanced supercapacitors. J Mater Chem A 3:18154–18162. https://doi.org/10.1039/C5TA04721H

Song HJ, Gurav R, Bhatia SK, Lee EB, Kim HJ, Yang Y-H, Kan E, Kim HH, Lee SH, Choi Y-K (2021) Treatment of microcystin-LR cyanotoxin contaminated water using Kentucky bluegrass-derived biochar. J Water Process Eng 41:102054. https://doi.org/10.1016/j.jwpe.2021.102054

Sun J, He F, Pan Y, Zhang Z (2017) Effects of pyrolysis temperature and residence time on physicochemical properties of different biochar types. Acta Agric Scand Sect B Soil Plant Sci 67:12–22. https://doi.org/10.1080/09064710.2016.1214745

Sun J, Niu J, Liu M, Ji J, Dou M, Wang F (2018a) Biomass-derived nitrogen-doped porous carbons with tailored hierarchical porosity and high specific surface area for high energy and power density supercapacitors. Appl Surf Sci 427:807–813. https://doi.org/10.1016/j.apsusc.2017.07.220

Sun Z, Zheng M, Hu H, Dong H, Liang Y, Xiao Y, Lei B, Liu Y (2018b) From biomass wastes to vertically aligned graphene nanosheet arrays: a catalyst-free synthetic strategy towards high-quality graphene for electrochemical energy storage. Chem Eng J 336:550–561. https://doi.org/10.1016/j.cej.2017.12.019

Sun H, Yang B, Li A (2019a) Biomass derived porous carbon for efficient capture of carbon dioxide, organic contaminants and volatile iodine with exceptionally high uptake. Chem Eng J 372:65–73. https://doi.org/10.1016/j.cej.2019.04.061

Sun N, Li Z, Zhang X, Qin W, Zhao C, Zhang H, Ng DHL, Kang S, Zhao H, Wang G (2019b) Hierarchical porous carbon materials derived from kelp for superior capacitive applications. ACS Sustain Chem Eng 7:8735–8743. https://doi.org/10.1021/acssuschemeng.9b00635

Sun Y, Yu IKM, Tsang DCW, Fan J, Clark JH, Luo G, Zhang S, Khan E, Graham NJD (2020) Tailored design of graphitic biochar for high-efficiency and chemical-free microwave-assisted removal of refractory organic contaminants. Chem Eng J 398:125505. https://doi.org/10.1016/j.cej.2020.125505

Supraja KV, Kachroo H, Viswanathan G, Verma VK, Behera B, Doddapaneni TRKC, Kaushal P, Ahammad SZ, Singh V, Awasthi MK, Jain R (2023) Biochar production and its environmental applications: recent developments and machine learning insights. Biores Technol 387:129634. https://doi.org/10.1016/j.biortech.2023.129634

Świątek K, Gaag S, Klier A, Kruse A, Sauer J, Steinbach D (2020) Acid hydrolysis of lignocellulosic biomass: sugars and furfurals formation. Catalysts 10:437. https://doi.org/10.3390/catal10040437

Tan X-f, Liu Y-g, Gu Y-l, Xu Y, Zeng G-m, Hu X-j, Liu S-b, Wang X, Liu S-m, Li J (2016) Biochar-based nano-composites for the decontamination of wastewater: a review. Biores Technol 212:318–333. https://doi.org/10.1016/j.biortech.2016.04.093

Tan YC, Jia S, Tan J, Leow Y, Zheng R, Tan XY, Dolmanan SB, Zhang M, Yew PYM, Ni XP, Zhu Q, Xu J, Loh XJ, Ramakrishna S, Kai D (2023) Coconut husk-derived biochar for enhancing electrochemical conversion of $CO_2$. Mater Today Chemistry 30:101595. https://doi.org/10.1016/j.mtchem.2023.101595

Tian W, Zhang H, Qian Z, Ouyang T, Sun H, Qin J, Tadé MO, Wang S (2018) Bread-making synthesis of hierarchically Co@C nanoarchitecture in heteroatom doped porous carbons for oxidative degradation of emerging contaminants. Appl Catal B 225:76–83. https://doi.org/10.1016/j.apcatb.2017.11.056

Tian W, Gao Q, VahidMohammadi A, Dang J, Li Z, Liang X, Hamedi MM, Zhang L (2021) Liquid-phase exfoliation of layered biochars into multifunctional heteroatom (Fe, N, S) co-doped graphene-like carbon nanosheets. Chem Eng J 420:127601. https://doi.org/10.1016/j.cej.2020.127601

Tiwari SK, Bystrzejewski M, De Adhikari A, Huczko A, Wang N (2022) Methods for the conversion of biomass waste into value-added carbon nanomaterials: recent progress and applications. Prog Energy Combust Sci 92:101023. https://doi.org/10.1016/j.pecs.2022.101023

Tomczyk A, Sokołowska Z, Boguta P (2020) Biochar physicochemical properties: pyrolysis temperature and feedstock kind effects. Rev Environ Sci Bio/Technol 19:191–215. https://doi.org/10.1007/s11157-020-09523-3

Vu TM, Trinh VT, Doan DP, Van HT, Nguyen TV, Vigneswaran S, Ngo HH (2017) Removing ammonium from water using modified corncob-biochar. Sci Total Environ 579:612–619. https://doi.org/10.1016/j.scitotenv.2016.11.050

Vuppaladadiyam AK, Vuppaladadiyam SSV, Awasthi A, Sahoo A, Rehman S, Pant KK, Murugavelh S, Huang Q, Anthony E, Fennel P, Bhattacharya S, Leu S-Y (2022) Biomass pyrolysis: a review on recent advancements and green hydrogen production. Biores Technol 364:128087. https://doi.org/10.1016/j.biortech.2022.128087

Wahab MA, Darain F, Islam N, Young DJ (2018) Nano/Mesoporous Carbon from Rice Starch for Voltammetric Detection of Ascorbic Acid. Molecules. 23:234. https://doi.org/10.3390/molecules23020234

Wan L, Xiao R, Liu J, Zhang Y, Chen J, Du C, Xie M (2020a) A novel strategy to prepare N, S-codoped porous carbons derived from barley with high surface area for supercapacitors. Appl Surf Sci 518:146265. https://doi.org/10.1016/j.apsusc.2020.146265

Wan Z, Sun Y, Tsang DCW, Khan E, Yip ACK, Ng YH, Rinklebe J, Ok YS (2020b) Customised fabrication of nitrogen-doped biochar for environmental and energy applications. Chem Eng J 401:126136. https://doi.org/10.1016/j.cej.2020.126136

Wang C, Wu D, Wang H, Gao Z, Xu F, Jiang K (2018a) Biomass derived nitrogen-doped hierarchical porous carbon sheets for supercapacitors with high performance. J Colloid Interface Sci 523:133–143. https://doi.org/10.1016/j.jcis.2018.03.009

Wang Y-Y, Ji H-Y, Lu H-H, Liu Y-X, Yang R-Q, He L-L, Yang S-M (2018b) Simultaneous removal of Sb(III) and Cd(II) in water by adsorption onto a $MnFe_2O_4$-biochar nanocomposite. RSC Adv 8:3264–3273. https://doi.org/10.1039/C7RA13151H

Wang G, Zhang J, Lee J-Y, Mao X, Ye L, Xu W, Ning X, Zhang N, Teng H, Wang C (2020a) Hydrothermal carbonization of maize straw for hydrochar production and its injection for blast furnace. Appl Energy 266:114818. https://doi.org/10.1016/j.apenergy.2020.114818

Wang J, Wei H, Chen X, Chen C, Xa C (2020b) Facile preparation of N, P co-doped molybdenum carbide/porous carbon rough microspheres for efficient electrocatalytic hydrogen evolution. Int J Hydrogen Energy 45:595–604. https://doi.org/10.1016/j.ijhydene.2019.10.241

Wang X, Fang J, Liu X, Zhang X, Lv Q, Xu Z, Zhang X, Zhu W, Zhuang Z (2020c) Converting biomass into efficient oxygen reduction reaction catalysts for proton exchange membrane fuel cells. Sci China Mater 63:524–532. https://doi.org/10.1007/s40843-019-1224-5

Wang H, Sun J, Wang J, Jiang L, Liu H (2021a) Green synthesis of nitrogen and fluorine co-doped porous carbons from sustainable coconut shells as an advanced synergistic electrocatalyst for oxygen reduction. J Market Res 13:962–970. https://doi.org/10.1016/j.jmrt.2021.05.048

Wang J, Kong H, Zhang J, Hao Y, Shao Z, Ciucci F (2021b) Carbon-based electrocatalysts for sustainable energy applications. Prog Mater Sci 116:100717. https://doi.org/10.1016/j.pmatsci.2020.100717

Wang N, Bo X, Zhou M (2021c) Laser conversion of biomass into porous carbon composite under ambient condition for pH-Universal electrochemical hydrogen evolution reaction. J Colloid Interface Sci 604:885–893. https://doi.org/10.1016/j.jcis.2021.07.057

Wang F, Li Q, Xiao Z, Jiang B, Ren J, Jin Z, Tang X, Chen Y, Li X (2022a) Conversion of rice husk biomass into electrocatalyst for oxygen reduction reaction in Zn-air battery: effect of self-doped Si on performance. J Colloid Interface Sci 606:1014–1023. https://doi.org/10.1016/j.jcis.2021.08.117

Wang Y-j, Yu Y, Huang H-j, Yu C-l, Fang H-s, Zhou C-h, Yin X, Chen W-h, Guo X-c (2022b) Efficient conversion of sewage sludge into hydrochar by microwave-assisted hydrothermal carbonization. Sci Total Environ 803:149874. https://doi.org/10.1016/j.scitotenv.2021.149874

Wang D, Wen C, Zhang B, Zhu G, Wen W, Liu Q, Liu T (2023a) Sustainable eutectic mixture strategy of molten salts for preparing biochar with interconnected pore structure from algal residue and its performance in aqueous supercapacitor. J Energy Storage 69:107935. https://doi.org/10.1016/j.est.2023.107935

Wang G, Li D, Xiong L, Dan J, Xu K, Yuan X, Kan G, Ning X, Wang C (2023b) Application of catalysts in biomass hydrothermal carbonization for the preparation of high-quality blast furnace injection fuel. Energy 283:129147. https://doi.org/10.1016/j.energy.2023.129147

Wang S, Shi Y, Chen S, Zhu C, Wang X, Zhou T, Su L, Tan C, Zhang L, Xiang H (2023c) Porous biochars with nitrogen defects prepared from hydrogel template-modified food waste for high-performance supercapacitors. J Energy Storage 72:108720. https://doi.org/10.1016/j.est.2023.108720

Wei H, Chen J, Fu N, Chen H, Lin H, Han S (2018) Biomass-derived nitrogen-doped porous carbon with superior capacitive performance and high $CO_2$ capture capacity. Electrochim Acta 266:161–169. https://doi.org/10.1016/j.electacta.2017.12.192

Wei X, Zhang Z, Qin L, Dai J (2019) Template-free preparation of yeast-derived three-dimensional hierarchical porous carbon for highly efficient sulfamethazine adsorption from water. J Taiwan Inst Chem Eng 95:532–540. https://doi.org/10.1016/j.jtice.2018.09.009

Wu D, Shi Y, Jing H, Wang X, Song X, Si D, Liang S, Hao C (2018) Tea-leaf-residual derived electrocatalyst: Hierarchical pore structure and self nitrogen and fluorine co-doping for efficient oxygen reduction reaction. Int J Hydrogen Energy 43:19492–19499. https://doi.org/10.1016/j.ijhydene.2018.08.201

Wu L, Cai Y, Wang S, Li Z (2021) Doping of nitrogen into biomass-derived porous carbon with large surface area using $N_2$ non-thermal plasma technique for high-performance supercapacitor. Int J Hydrogen Energy 46:2432–2444. https://doi.org/10.1016/j.ijhydene.2020.10.037

Wu Y, Ghalkhani M, Ashrafzadeh Afshar E, Karimi F, Xia C, Le QV, Vasseghian Y (2022) Recent progress in Biomass-derived nanoelectrocatalysts for the sustainable energy development. Fuel 323:124349. https://doi.org/10.1016/j.fuel.2022.124349

Xia C, Surendran S, Ji S, Kim D, Chae Y, Kim J, Je M, Han M-K, Choe W-S, Choi CH, Choi K, Kim JK, Sim U (2022a) A sulfur self-doped multifunctional biochar catalyst for overall water splitting and a supercapacitor from Camellia japonica flowers. Carbon Energy 4:491–505. https://doi.org/10.1002/cey2.207

Xia J, Shen Y, Zhang H, Hu X, Mian MM, Zhang W-H (2022b) Synthesis of magnetic nZVl@biochar catalyst from acid precipitated black liquor and Fenton sludge and its application for Fenton-like removal of rhodamine B dye. Ind Crops Prod 187:115449. https://doi.org/10.1016/j.indcrop.2022.115449

Xie Y, Hu W, Wang X, Tong W, Li P, Zhou H, Wang Y, Zhang Y (2020) Molten salt induced nitrogen-doped biochar nanosheets as highly efficient peroxymonosulfate catalyst for organic pollutant degradation. Environ Pollut 260:114053. https://doi.org/10.1016/j.envpol.2020.114053

Xing T, Sunarso J, Yang W, Yin Y, Glushenkov AM, Li LH, Howlett PC, Chen Y (2013) Ball milling: a green mechanochemical approach for synthesis of nitrogen doped carbon nanoparticles. Nanoscale 5:7970–7976. https://doi.org/10.1039/C3NR02328A

Xu Z, Wu Z, Chi J, Lei E, Liu Y, Yin Y, Yang Z, Ma C, Li W, Luo S, Liu S (2023) Soft-template hydrothermal synthesis of N and B co-doped walnut-shaped porous carbon spheres with hydrophilic surfaces for supercapacitors. Appl Surface Sci 638:158016. https://doi.org/10.1016/j.apsusc.2023.158016

Xue B, Wang Z, Zhu Y, Wang X, Xiao R (2021) Sustainable and recyclable synthesis of porous carbon sheets from rice husks for energy storage: a strategy of comprehensive utilization. Ind Crops Prod 170:113724. https://doi.org/10.1016/j.indcrop.2021.113724

Yameen MZ, AlMohamadi H, Naqvi SR, Noor T, Chen W-H, Amin NAS (2023a) Advances in production & activation of marine macroalgae-derived biochar catalyst for sustainable biodiesel production. Fuel 337:127215. https://doi.org/10.1016/j.fuel.2022.127215

Yameen MZ, Naqvi SR, AlMohamadi H, Wang S (2023b) Process optimization, kinetic, and thermodynamic studies of biodiesel production using KOH-modified bio-carbon catalyst derived from marine macroalgae. Carbon Lett 33:1571–1590. https://doi.org/10.1007/s42823-023-00541-z

Yan B, Zheng J, Feng L, Du C, Jian S, Yang W, Wu YA, Jiang S, He S, Chen W (2022) Wood-derived biochar as thick electrodes for high-rate performance supercapacitors. Biochar 4:50. https://doi.org/10.1007/s42773-022-00176-9

Yan C, Yang Y, Wei J, Hou J, Shao Z (2023) N self-doped multifunctional chitosan biochar-based microsphere with heterogeneous interfaces for self-powered supercapacitors to drive overall water splitting. Biochar 5:90. https://doi.org/10.1007/s42773-023-00266-2

Yang H, Kou S, Li Z, Chang Z, Wang M, Liu Z, Lu G (2019a) 3D interconnected nitrogen-self-doped carbon aerogels as efficient oxygen reduction electrocatalysts derived from biomass gelatin. RSC Adv 9:40301–40308. https://doi.org/10.1039/C9RA07926B

Yang M, Wu D, Cheng D (2019b) Biomass-derived porous carbon supported Co–CoO yolk-shell nanoparticles as enhanced multifunctional electrocatalysts. Int J Hydrogen Energy 44:6525–6534. https://doi.org/10.1016/j.ijhydene.2019.01.155

Yang D, Wang L, Li Z, Tang X, He M, Yang S, Liu X, Xu J (2020a) Simultaneous adsorption of Cd(II) and As(III) by a novel biochar-supported nanoscale zero-valent iron in aqueous systems. Sci Total Environ 708:134823. https://doi.org/10.1016/j.scitotenv.2019.134823

Yang H, Ye S, Zeng Z, Zeng G, Tan X, Xiao R, Wang J, Song B, Du L, Qin M, Yang Y, Xu F (2020b) Utilization of biochar for resource recovery from water: a review. Chem Eng J 397:125502. https://doi.org/10.1016/j.cej.2020.125502

Yang B, Dai J, Zhao Y, Wu J, Ji C, Zhang Y (2022a) Advances in preparation, application in contaminant removal, and environmental risks of biochar-based catalysts: a review. Biochar 4:51. https://doi.org/10.1007/s42773-022-00169-8

Yang J, Xu H, Chen H, Meng F, Zu H, Zhu P, Yang Z, Li M, Li H (2022b) Removal of flue gas mercury by porous carbons derived from one-pot carbonization and activation of wood sawdust in a molten salt medium. J Hazard Mater 424:127336. https://doi.org/10.1016/j.jhazmat.2021.127336

Yang X, Cao B, Jiang D, He S, Yuan C, Li H, Naqvi SR, Wang S (2023a) Catalytic pyrolysis of guaiacol on Enteromorpha-based biochar: a combination of experiments and density functional theory. Fuel Process Technol 239:107527. https://doi.org/10.1016/j.fuproc.2022.107527

Yang X, He H, Lv T, Qiu J (2023b) Fabrication of biomass-based functional carbon materials for energy conversion and storage. Mater Sci Eng R Rep 154:100736. https://doi.org/10.1016/j.mser.2023.100736

Yang X, You M, Liu S, Sarkar B, Liu Z, Yan X (2023c) Microbial responses towards biochar application in potentially toxic element (PTE) contaminated soil: a critical review on effects and potential mechanisms. Biochar 5:57. https://doi.org/10.1007/s42773-023-00255-5

Yang Y, Zhong M, Bian X, You Y, Li F (2023d) Preparation of carbon-based material with high water absorption capacity and its effect on the water retention characteristics of sandy soil. Biochar 5:61. https://doi.org/10.1007/s42773-023-00260-8

Yaseen W, Xie M, Yusuf BA, Xu Y, Rafiq M, Ullah N, Zhou P, Li X, Xie J (2022) Hierarchical Co/$MoO_2$@N-doped carbon nanosheets derived from waste lotus leaves for electrocatalytic water splitting. Int J Hydrogen Energy 47:15673–15686. https://doi.org/10.1016/j.ijhydene.2022.03.037

Ye Q, Li Q, Li X (2022) Removal of heavy metals from wastewater using biochars: adsorption and mechanisms. Environ Pollut Bioavail 34:385–394. https://doi.org/10.1080/26395940.2022.2120542

Yihunu EW, Minale M, Abebe S, Limin M (2019) Preparation, characterization and cost analysis of activated biochar and hydrochar derived from agricultural waste: a comparative study. SN Appl Sci 1:873. https://doi.org/10.1007/s42452-019-0936-z

Yin M, Bai X, Wu D, Li F, Jiang K, Ma N, Chen Z, Zhang X, Fang L (2022) Sulfur-functional group tunning on biochar through sodium thiosulfate modified molten salt process for efficient heavy metal adsorption. Chem Eng J 433:134441. https://doi.org/10.1016/j.cej.2021.134441

Yu H, Zou W, Chen J, Chen H, Yu Z, Huang J, Tang H, Wei X, Gao B (2019) Biochar amendment improves crop production in problem soils: a review. J Environ Manag 232:8–21. https://doi.org/10.1016/j.jenvman.2018.10.117

Yu J, Hu H, Wu X, Zhou T, Liu Y, Ruan R, Zheng H (2020a) Coupling of biochar-mediated absorption and algal-bacterial system to enhance nutrients

recovery from swine wastewater. Sci Total Environ 701:134935. https://doi.org/10.1016/j.scitotenv.2019.134935

Yu Y-q, Li J-x, Liao Y-l, Yang J-y (2020b) Effectiveness, stabilization, and potential feasible analysis of a biochar material on simultaneous remediation and quality improvement of vanadium contaminated soil. J Clean Prod 277:123506. https://doi.org/10.1016/j.jclepro.2020.123506

Yu F, Tian F, Zou H, Ye Z, Peng C, Huang J, Zheng Y, Zhang Y, Yang Y, Wei X, Gao B (2021) ZnO/biochar nanocomposites via solvent free ball milling for enhanced adsorption and photocatalytic degradation of methylene blue. J Hazard Mater 415:125511. https://doi.org/10.1016/j.jhazmat.2021.125511

Yuan X, Wang J, Deng S, Suvarna M, Wang X, Zhang W, Hamilton ST, Alahmed A, Jamal A, Park A-HA, Bi X, Ok YS (2022) Recent advancements in sustainable upcycling of solid waste into porous carbons for carbon dioxide capture. Renew Sustain Energy Rev 162:112413. https://doi.org/10.1016/j.rser.2022.112413

Yuan X, Cao Y, Li J, Patel AK, Dong C-D, Jin X, Gu C, Yip ACK, Tsang DCW, Ok YS (2023a) Recent advancements and challenges in emerging applications of biochar-based catalysts. Biotechnol Adv 67:108181. https://doi.org/10.1016/j.biotechadv.2023.108181

Yuan X, Shen Y, Withana PA, Mašek O, Lin CSK, You S, Tack FMG, Ok YS (2023b) Thermochemical upcycling of food waste into engineered biochar for energy and environmental applications: a critical review. Chem Eng J 469:143783. https://doi.org/10.1016/j.cej.2023.143783

Yue L, Chen L, Liu X, Lu D, Zhou W, Li Y (2022) Honeycomb-like biomass carbon with planted $CoNi_3$ alloys to form hierarchical composites for high-performance supercapacitors. J Colloid Interface Sci 608:2602–2612. https://doi.org/10.1016/j.jcis.2021.10.184

Zeng F, Li Z, Li X, Wang J, Kong Z, Sun Y, Liu Z, Feng H (2019) Almond-derived origami-like hierarchically porous and N/O co-functionalized carbon sheet for high-performance supercapacitor. Appl Surf Sci 467–468:229–235. https://doi.org/10.1016/j.apsusc.2018.10.089

Zhang M, Gao B, Yao Y, Xue Y, Inyang M (2012) Synthesis of porous MgO-biochar nanocomposites for removal of phosphate and nitrate from aqueous solutions. Chem Eng J 210:26–32. https://doi.org/10.1016/j.cej.2012.08.052

Zhang J, Zhang D, Li K, Tian Y, Wang Y, Sun T (2021) N, O and S co-doped hierarchical porous carbon derived from a series of samara for lithium and sodium storage: insights into surface capacitance and inner diffusion. J Colloid Interface Sci 598:250–259. https://doi.org/10.1016/j.jcis.2021.04.047

Zhang X, Cao L, Xiang W, Xu Y, Gao B (2022) Preparation and evaluation of fine-tuned micropore biochar by lignin impregnation for $CO_2$ and VOCs adsorption. Sep Purif Technol 295:121295. https://doi.org/10.1016/j.seppur.2022.121295

Zhao L, Cao X, Mašek O, Zimmerman A (2013) Heterogeneity of biochar properties as a function of feedstock sources and production temperatures. J Hazard Mater 256–257:1–9. https://doi.org/10.1016/j.jhazmat.2013.04.015

Zhao L, Zheng W, Cao X (2014) Distribution and evolution of organic matter phases during biochar formation and their importance in carbon loss and pore structure. Chem Eng J 250:240–247. https://doi.org/10.1016/j.cej.2014.04.053

Zhao Y, Ran W, He J, Song Y, Zhang C, Xiong D-B, Gao F, Wu J, Xia Y (2015) Oxygen-rich hierarchical porous carbon derived from artemia cyst shells with superior electrochemical performance. ACS Appl Mater Interfaces 7:1132–1139. https://doi.org/10.1021/am506815f

Zhao S, Yan T, Wang Z, Zhang J, Shi L, Zhang D (2017) Removal of NaCl from saltwater solutions using micro/mesoporous carbon sheets derived from watermelon peel via deionization capacitors. RSC Adv 7:4297–4305. https://doi.org/10.1039/C6RA27127H

Zhao B, O'Connor D, Zhang J, Peng T, Shen Z, Tsang DCW, Hou D (2018) Effect of pyrolysis temperature, heating rate, and residence time on rapeseed stem derived biochar. J Clean Prod 174:977–987. https://doi.org/10.1016/j.jclepro.2017.11.013

Zhao N, Zhao C, Tsang DCW, Liu K, Zhu L, Zhang W, Zhang J, Tang Y, Qiu R (2021) Microscopic mechanism about the selective adsorption of Cr(VI) from salt solution on O-rich and N-rich biochars. J Hazard Mater 404:124162. https://doi.org/10.1016/j.jhazmat.2020.124162

Zheng T, Ouyang S, Zhou Q (2023) Synthesis, characterization, safety design, and application of NPs@BC for contaminated soil remediation

and sustainable agriculture. Biochar 5:5. https://doi.org/10.1007/s42773-022-00198-3

Zhou Y, Leng Y, Zhou W, Huang J, Zhao M, Zhan J, Feng C, Tang Z, Chen S, Liu H (2015) Sulfur and nitrogen self-doped carbon nanosheets derived from peanut root nodules as high-efficiency non-metal electrocatalyst for hydrogen evolution reaction. Nano Energy 16:357–366. https://doi.org/10.1016/j.nanoen.2015.07.008

Zhou W, Lei S, Sun S, Ou X, Fu Q, Xu Y, Xiao Y, Cheng B (2018) From weed to multi-heteroatom-doped honeycomb-like porous carbon for advanced supercapacitors: a gelatinization-controlled one-step carbonization. J Power Sour 402:203–212. https://doi.org/10.1016/j.jpowsour.2018.09.044

Zhou J, Ye S, Zeng Q, Yang H, Chen J, Guo Z, Jiang H, Rajan K (2020) Nitrogen and phosphorus co-doped porous carbon for high-performance supercapacitors. Front Chem 8:105. https://doi.org/10.3389/fchem.2020.00105

Zhou R, Wang X, Zhou R, Weerasinghe J, Zhang T, Xin Y, Wang H, Cullen P, Wang H, Ostrikov KK (2022) Non-thermal plasma enhances performances of biochar in wastewater treatment and energy storage applications. Front Chem Sci Eng 16:475–483. https://doi.org/10.1007/s11705-021-2070-x

Zhou Y, Yan L, Hou J (2022) Nanosheets with high-performance electrochemical oxygen reduction reaction revived from green walnut peel. Molecules. 27:328. https://doi.org/10.3390/molecules27010328

Zhou C, Zhang J, Pei Y, Tian K, Zhang X, Yan X, Yang J (2023) Molten salt strategy to activate biochar for enhancing biohydrogen production. Biores Technol 385:129466. https://doi.org/10.1016/j.biortech.2023.129466

Zhu Y, Xu G, Zhang X, Wang S, Li C, Wang G (2017) Hierarchical porous carbon derived from soybean hulls as a cathode matrix for lithium-sulfur batteries. J Alloy Compd 695:2246–2252. https://doi.org/10.1016/j.jallcom.2016.11.075

Zhu S, Zhao N, Li J, Deng X, Sha J, He C (2019) Hard-template synthesis of three-dimensional interconnected carbon networks: Rational design, hybridization and energy-related applications. Nano Today 29:100796. https://doi.org/10.1016/j.nantod.2019.100796

Zhu K, Bin Q, Shen Y, Huang J, He D, Chen W (2020) In-situ formed N-doped bamboo-like carbon nanotubes encapsulated with Fe nanoparticles supported by biochar as highly efficient catalyst for activation of persulfate (PS) toward degradation of organic pollutants. Chem Eng J 402:126090. https://doi.org/10.1016/j.cej.2020.126090

Zhu K, Qin W, Gan Y, Huang Y, Jiang Z, Chen Y, Li X, Yan K (2023a) Acceleration of $Fe^{3+}/Fe^{2+}$ cycle in garland-like MIL-101(Fe)/$MoS_2$ nanosheets to promote peroxymonosulfate activation for sulfamethoxazole degradation. Chem Eng J 470:144190. https://doi.org/10.1016/j.cej.2023.144190

Zhu X, Sun M, Zhu X, Guo W, Luo Z, Cai W, Zhu X (2023b) Molten salt shielded pyrolysis of biomass waste: development of hierarchical biochar, salt recovery, $CO_2$ adsorption. Fuel 334:126565. https://doi.org/10.1016/j.fuel.2022.126565

Zou Z, Lei Y, Li Y, Zhang Y, Xiao W (2019) Nitrogen-doped hierarchical meso/microporous carbon from bamboo fungus for symmetric supercapacitor applications. Molecules 24:3677. https://doi.org/10.3390/molecules24203677

Zou Q, Wang B, Gao B, Jiang T, Feng Q, Chen M, Zhang J, Zhang X (2023) Roles and mechanisms of carbonaceous materials in advanced oxidation coupling processes for degradation organic pollutants in wastewater: a review. Biochar 5:86. https://doi.org/10.1007/s42773-023-00285-z